Onshore and offshore seismotectonics of Iberia: An updated review

Antonio Olaiz[1], José A. Álvarez Gómez[2], Gerardo de Vicente[2,3], Alfonso Muñoz-Martín[2,3], Juan V. Cantavella[4], Susana Custódio[5], Dina Vales[6] and Oliver Heidbach[7,8].

[1]Repsol E&P, C/Méndez Álvaro 44, 28045, Madrid, Spain
[2]GEODESPAL, Faculta de C.C. Geológicas, Universidad Complutense de Madrid, Spain
[3]Instituto de Geociencias IGEO, CSIC-UCM, Madrid, Spain
[4]Instituto Geográfico Nacional, C/General Ibáñez Íbero, 3, 28003, Madrid, Spain
[5]Instituto Dom Luiz, Faculdade de Ciências, Universidade de Lisboa, 1749-016 Lisboa, Portugal.
[6]Instituto Português do Mar e da Atmosfera, Lisboa, Portugal
[7]Helmholtz Centre Potsdam, GFZ German Research Centre for Geosciences. Germany, 14473 Potsdam, Germany
[8]Institute for Applied Geosciences, TU Berlin, 10587 Berlin, Germany

Correspondence to: Antonio Olaiz (antoniojose.olaiz@repsol.com)

Abstract. An analysis of 542 moment tensor focal mechanisms across the Iberian Peninsula was conducted to infer active tectonic deformation and stress regimes. This study employed a suite of complementary methodologies, including FMC classification of the rupture type; composed focal mechanism based on the average seismic moment tensor; rotation angle between tensors estimates; Right Dihedra composed focal mechanisms; Slip Model analysis to determine the strain conditions and classical stress inversion methodology. Based on the Slip Model results and considering the tectonic constraints of Cenozoic deformation in Iberia, the study region was subdivided into several tectonically coherent zones, where the different methods were applied independently to ensure robust regional interpretations. The results indicate that thrust faulting stress regimes are active in the Gorringe-Horseshoe area and the easternmost Tell Atlas. In the south, most of the zones are transpressive, as is the southwestern corner of Iberia, south of Lisbon. The exception is the Granada Basin, which exhibits a nearly t radial normal faulting stress regime. Normal faulting stresses are dominant in the Pyrenees and the Mediterranean rim, north of the Betic Mountains. In the central part of the Pyrenees, the maximum horizontal extension is oriented perpendicular to the mountain range, indicating that local stresses related to post-orogenic collapse or isostatic rebound dominate over regional ones. The maximum horizontal compression along the Eurasia-Africa plate limit is consistently oriented around N154°E, except in some parts of the Betics that are probably influenced by a remnant effect of the Alboran Slab. In the Central Ranges and offshore Atlantic, the maximum horizontal compression is slightly rotated anticlockwise to N140°E.

1 Introduction and objectives

The Iberian Peninsula, and the former Iberian microplate, shows evidence of an intense and distributed Alpine deformation that occurred over geologic time scales (de Vicente and Vegas, 2009) (Fig. 1). After the Variscan orogeny, and during the Mesozoic, numerous extensional structures developed, in which thick sedimentary deposits accumulated, with one exception, on the Iberian Massif to the west. At the northern edge of the Iberian microplate, this extension even reached the stage of oceanic crust generation (Montadert et al., 1971; Nirrengarten et al., 2018; Sibuet et al., 2004), albeit during a very short time (Aptian-Albian) (Srivastava et al., 1990). Tectonic reconstructions indicate that the Iberian microplate moved independently relative to Africa and Eurasia until its collision with Eurasia to form the Cantabrian-Pyrenean Orogen (Roca and Muñoz, 1996).

A pronounced change in the tectonic framework has been suggested to have occurred around 84 Ma, when an incipient collision between the Iberian microplate and Africa may have begun (Reicherter and Pletsch, 2000). In any case, from the beginning of the Eocene, the Iberian microplate underwent compression, not only at its northern border, where an incipient subduction zone was located (Gallastegui and Pulgar, 2002; Fernandez-Viejo et al., 2012), but also in its interior, as documented in the sedimentary infill of Madrid and Duero Basin (de Vicente et al., 2007)

Alpine compression in the interior of the Iberian microplate resulted in the inversion of the Mesozoic aulacogen of the Iberian Basin (Iberian Chain, IC), and the development of a series of ranges with crustal thickening along the Iberian microplate (i.e., the Spanish Portuguese Central System, SPCS). This set of intra-plate ranges can also be considered as an incipient and aborted orogen (de Vicente et al., 2022). It has also been suggested that the Iberian block accommodated shortening by forming lithospheric folds (Cloetingh et al., 2002). Accompanying these significant thrusts, major strike-slip faults deformation belts were activated at the crustal scale, such as the South ("Castilian") and North ("Aragonese") Branches of the IC, and the Messejana-Plasencia fault (more than 500 km long), which nucleated on an end-Triassic basic dyke related to the Central Atlantic Magmatic Province (Cebriá et al., 2003; Villamor, 2002; de Vicente et al., 2021). The age of the main deformation event for these fault systems is Oligocene - Early Miocene. However, in the westernmost sector, the SPCS and the left-lateral strike-slip faults of Règua and Vilariça display deformation during the Middle-Late Miocene. They are still considered active structures (Cabral, 2012).

Today, extensional structures dominate the easternmost part of the Iberian Peninsula (since the Late Miocene), due to back-arc extension related to a subduction zone below Corsica and Sardinia (e.g. Faccenna et al., 2002), initially a part of the Iberian microplate (van Hinsbergen et al., 2014). A normal faulting stress regime, unrelated to plate tectonics, also affects the Pyrenees, where a post-orogenic collapse process has been suggested (Asensio et al., 2012. The active plate boundary is considered to have progressively migrated southward, from its initial position to the north, when Iberia acted as an independent, to its current configuration along the southern margin of the Iberian Peninsula (Terceira Ridge – Gloria Fault – Alboran Basin – Tell Atlas). This tectonic reorganization coincided with the integration of Iberia into the Eurasian Plate. The resulting geodynamic setting is characterized by a diffuse plate boundary encompassing the Betic Cordillera, where coeval compressional and extensional tectonic regimes are accommodated. These processes are primarily governed by the westward migration and emplacement of

65   the Alboran Domain and the ongoing subduction of the southern Iberian margin. In this complex Cenozoic and neotectonic deformation setting, it is unsurprising that the present tectonic stresses in Iberia exhibit significant variations in both the stress regime and orientation of the principal stress axes (de Vicente et al., 2008) over relatively small areas.

Recent determinations of earthquake focal mechanisms by the Geophysical Institutes of Spain and Portugal have significantly expanded the regional seismicity catalogs maintained by Instituto Geográfico Nacional, Instituto Andaluz de Geofisica, and

70   Instituto Português do Mar e da Atmosfera. These datasets, enriched by peer-reviewed publications stemming from major research initiatives such as TopoIberia (e.g., Martín et al., 2015; Matos et al., 2018), as well as from the analysis of notable seismic crises (e.g., Villaseñor et al., 2020; Cesca et al., 2021), provide a robust foundation for advancing our understanding of the seismotectonic framework of the region).

In this study, we exclusively utilize well-fitted moment tensor focal mechanisms to study the contemporary deformation pattern

75   in the Iberian Peninsula. We analyse the rupture characteristics of focal mechanism populations for defined tectonic subareas employ the Slip Model described by Reches (1983) and de Vicente (1988) to ascertain the rupture plane among the two nodal planes). This information, along with the focal mechanisms populations, is then used to perform a stress inversion to determine the orientation of the maximum horizontal stress axis (or minimum extension) (S_{Hmax}) and the tectonic stress regime. Additionally, we derive the S_{Hmax} orientation from the individual focal mechanism and integrate these results with those from

80   the stress inversion into a revised dataset for the World Stress Map project, based on borehole logs, overcoring measurements, and geological stress indicators.
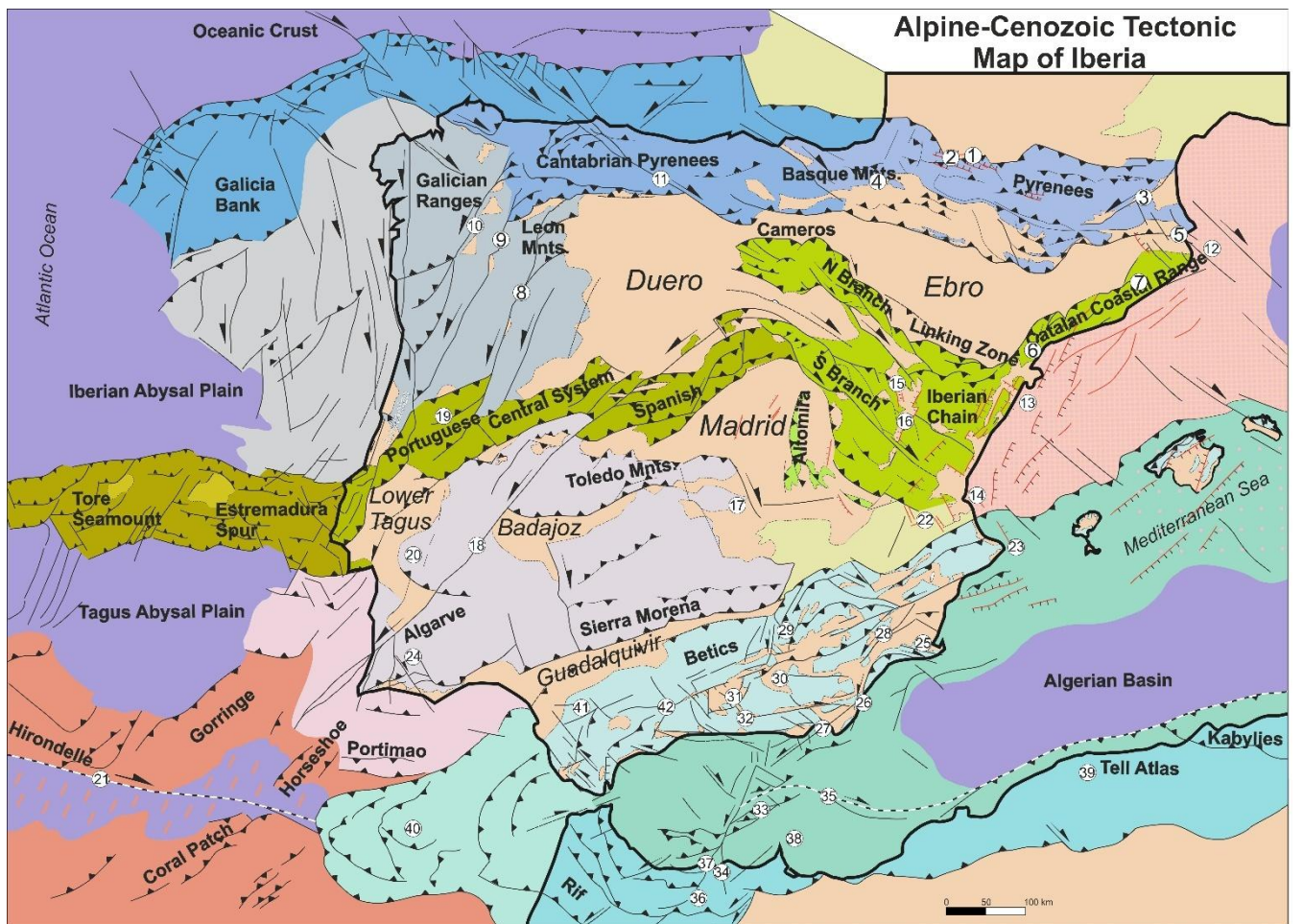
Figure 1: Alpine-Cenozoic tectonic map of Iberia, including continental and offshore domains, and showing areas that have experienced intense and distributed deformation. More recent normal faulting is shown by red lines. Q: Quaternary. Lourdes Fault (1), Bedous, Laruns, Pierrefitte and Pic de Midi du Bigorre faults (2), Têt Fault (3), Pamplona Fault (4), Amer and

Empordà faults (5), El Camp Fault (6), Montseny and Pla de Barcelona faults (7), Vilariça-Bragança fault system (8), Régua-Verín fault system (9), Monforte-Orense fault system (10), Ventaniella-Ubierna faults (11), Gulf of Rosas Fault (12), Amposta Basin Fault (13), Cape Cullera Fault (14), Jiloca Graben (15), Teruel Graben (16), Campos de Calatrava volcanism (17), Messejana-Plasencia Fault (18), Serra da Estrela Fault (19), Arraiolos and Évora seismic zones (20), Gloria Fault (21), Navarrés and Tous grabens (22), Cabo de la Nao Fault (23), São Marcos - Quarteira Fault (24), Mazarrón Fault (25), Palomares Fault (26), Serrata-Carboneras Fault (27), Alhama Fault (28), Tiscar and Guadiana Menor faults (29), Guadix Basin (30), Granada and Sierra Elvira-Dílar faults (31), Padul-Dúrcal Fault (32), Alborán Ridge (33), Idrissi Fault (34), Yusuf Fault (35), Nekor Fault (36), Al Hoceima area (37), Kert and Nador faults (38), Fault propagation associated to El Asnam earthquake (39), W verging thrusts Gulf of Cádiz (40), NE-SW thrusts (41), Torcal Shear Zone (42)

2 Data from earthquake focal mechanism

In this study, we establish a new and comprehensive compilation of robust focal mechanism solutions of onshore and offshore Iberia, inferred from waveform moment tensor inversions, using the following catalogues:

- Global Centroid Moment Tensor (former Harvard Centroid Moment Tensor https://www.globalcmt.org/, Dziewonski et al., 1981; Ekström et al., 2012)

- Instituto Geográfico Nacional de España (https://www.ign.es/web/ign/portal/tensor-momento-sismico/-/tensor-momento-sismico/getExplotacion, Rueda and Mezcua, 2005)

- Instituto Andaluz de Geofísica (https://iagpds.ugr.es/investigacion/informacion-general, Stich et al., 2003, 2006, 2010).

- Istituto Nazionale di Geofisica e Vulcanologia (http://terremoti.ingv.it/en/tdmt; Scognamiglio et al., 2006; Pondrelli et al., 2002, 2004)

- Geofon (GFZ-Postdam) (https://geofon.gfz-potsdam.de/old/eqinfo/list.php?mode=mt)

- ETH- Swiss Seismological Service (https://geophysics.ethz.ch/research/groups/sed.html) (Braunmiller et al., 2002).

- IPMA Portuguese Institute for Sea and Atmosphere (https://www.ipma.pt/en/geofisica/tensor)

This dataset was expanded through the integration of various regional studies (e.g., Carreño et al., 2008; Chevrot et al., 2011; Domingues et al., 2013; Custodio et al., 2016), datasets associated with projects such as TopoIberia (Martín et al., 2015), datasets related to earthquake clusters (Morales et al., 2015; Matos et al., 2018). Additionally, it incorporates results from specific seismic crisis events, most likely associated to induced seismicity (e.g., Villaseñor et al., 2020; Cesca et al., 2021;).

To further enhance the dataset, nine previously unpublished moment tensor focal mechanisms were determined for events that occurred between 2003 and 2019 (Table 1), and focal mechanisms for two historical events were also included in our dataset (Stich et al., 2005). The events are located at depths shallower than the Moho proposed by Diaz et al. (2016), except for some events located in oceanic crust, where the proposed crustal thickness is estimated at approximately 18 km and hypocentral depths are less than 30 km, within a domain in which the rheology of the upper mantle might be assumed to be similar to the crust. In cases where multiple solutions existed for the same even across different catalogues and appears, the double couple percentages (%DC) was used as a selection criterion, and the solution with the highest %DC was retained.

Long (º)	Lat (º)	Depth (km)	StrikeA (º)	DipA (º)	RakeA (º)	StrikeB (º)	DipB (º)	RakeB (º)	Mw	Date (YYYY/MM/DD)
-5.98	41.5	9	7	71	25	268	66	160	3.8	20030112
-2.34	40.21	11	228	71	-157	130	69	-20	3.3	20091014
-7.62	38.96	15	288	75	180	18	90	15	3.5	20100327
-8.546	37.35	8.5	84	85	168	175	78	6	3.3	20150722
-2.29	41.61	12	179	46	-87	355	44	-93	3.6	20150805
-8.524	37.237	20	216	50	88	39	40	92	3.2	20151021
-4.62	42.86	14	134	75	-86	297	16	-106	3.6	20180519
-9.552	37.73	28	35	62	52	275	62	52	3.6	20181001
-8.013	36.37	30	175	42	-165	74	80	-49	3.8	20190716

Table 1: Focal mechanisms calculated in this study

Thus, the final database consists of 542 events. In terms of temporal coverage, the first earthquake in our database is that of Benavente (Portugal) in 1909, and the most recent one occurred on 30 September 2023 (Fig. 2).
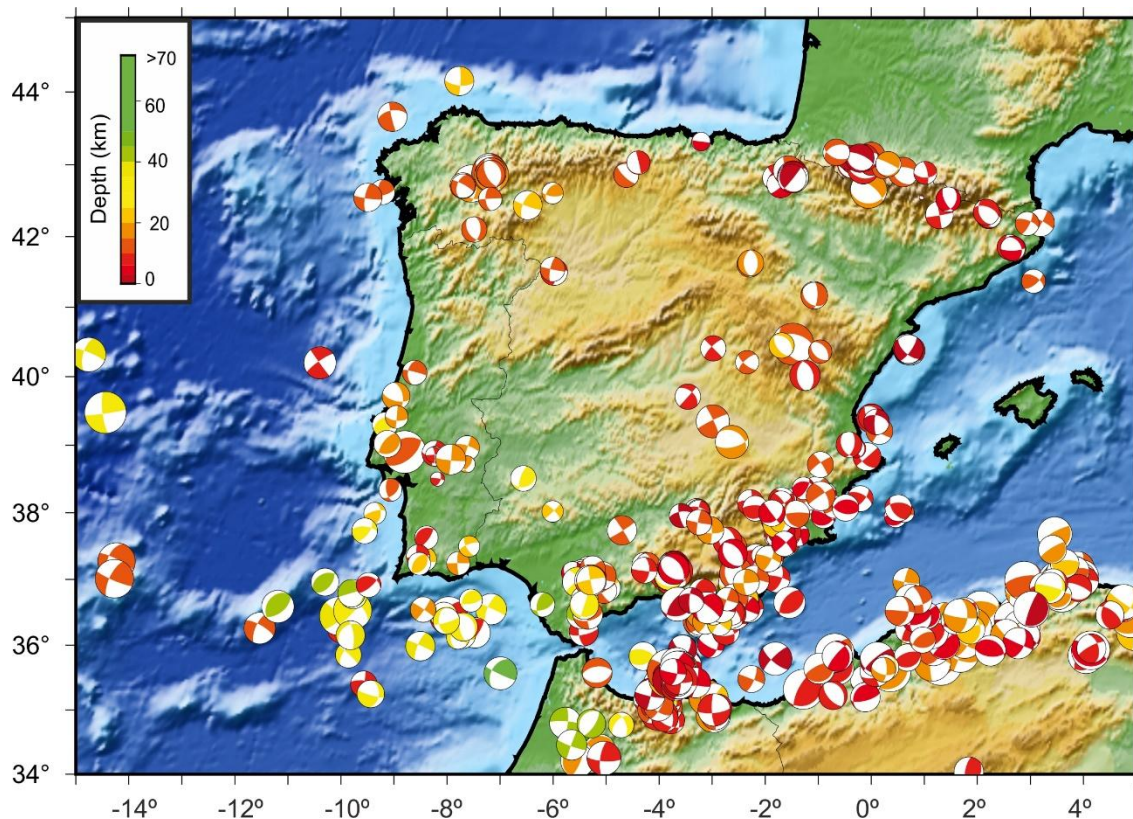
Figure 2: Distribution of the 542 focal mechanisms used in this study. The color of focal mechanisms indicates hypocentral depth.

3. Methodology

To characterize the tensorial properties of seismicity, two complementary analytical frameworks can be employed: a stress-based approach and a deformation-based approach. In this study, both methodologies are applied to provide a comprehensive understanding of the seismotectonic regime. For the deformation based type analysis, we use two approaches. First, a kinematic classification of rupture types is performed, including the derivation of a combined focal mechanism following the methodologies of Álvarez-Gómez (2019) and Kiratzi and Papazachos (1995). This is complemented by the application of the Right Dihedral method (Angelier and Mechler, 1977) and the Slip Model (Reches, 1983), which facilitates the identification of the most probable rupture plane to determine the stress tensor using classical inversion procedures, we will use the methodology proposed by Reches et al. (1992). This approach enables iterative testing of various friction coefficients, validated by angular criteria established by SLIP and PAM angles, as detailed in the subsequent section. The methodology has been recently revised and implemented in MATLAB (Busetti et al., 2014; Wetzler et al., 2021).

Terminological precision is maintained throughout the analysis. For individual focal mechanisms, we differentiate between reverse, strike-slip, and normal earthquakes. When referring to deformation, we use the terms shortening, shear, and extension.

Conversely, when discussing stresses, we use thrusting stress regime, strike-slip stress regime, and normal faulting stress regime.

3.1 Kinematic analysis. Composite focal mechanism

To gain insight into the kinematics related to the brittle behaviour of the lithosphere, we binned the focal mechanisms according to their rupture characteristics and stress-strain orientations in tectonic sub-areas. We refer to these from here onwards as tectonic zones. These zones were delimited considering the tectonic regimes, using a methodology explained in more detail in Section 4, which is a fundamental step in the stress inversion analysis.

For each tectonic zone, we classified the focal mechanisms by rupture type (reverse, strike-slip, normal) using the Focal Mechanisms Classification (FMC) diagram (Álvarez-Gómez, 2019). Then, for each rupture type population, we obtained a combined focal mechanism by averaging the moment tensor components following the approximation of Kiratzi and Papazachos (1995):

$$\bar{F}_{ik} = \frac{\sum_{x=1}^{n} M_O^x F_{ik}^x}{\sum_{x=1}^{n} M_O^x}, \tag{1}$$

Where F_{ik} is the normalized moment tensor, M_0 is the seismic moment, and the sums are performed over the number of events in each rupture population. If most of the released seismic moment is controlled by one of the earthquakes, the composite focal mechanism is very close to that of the larger event (Kiratzi and Papazachos, 1995). To avoid this effect in areas with moderate seismicity, an adequate approximation is to use only the sum of the seismic moment tensor components, disregarding the respective seismic moments. In this case, all earthquakes will have the same weight in the sum.

$$\bar{F}_{ik}^{RT} = \sum_{x=1}^{n} \bar{F}_{ik}^x, \tag{2}$$

where RT is each of the rupture types, encompassing n events, and i and k are the indices of the moment tensor components. As a result, we obtain a combined focal mechanism for each rupture type reflecting the geometry of the corresponding moment tensors and related deformation.

Following this reasoning, we can also obtain a composed focal mechanism considering all the events in a tectonic zone:

$$\bar{F}_{ik}^{zone} = \sum_{y=1}^{n} \bar{F}_{ik}^{(y)} = \bar{F}_{ik}^{Reverse} + \bar{F}_{ik}^{Strike-slip} + \bar{F}_{ik}^{Normal}, \tag{3}$$

As can be seen in equation 3, the summation of the combined rupture types is equivalent to the sum of all tensors. This enables quantification of of strain partitioning through the computation of the minimum rotation angle between rupture types, following the method proposed by Kagan (1991).

A way to assess the character of a moment tensor is to use its compensated linear vector dipole (*clvd*) component, which quantifies the extent to which the deviatoric part of the seismic moment tensor differs from a pure double-couple. We used the *clvd* ratio (*fclvd*) from Frohlich and Apperson (1992):

$$fclvd = \frac{|m_B|}{max[|m_T|,|m_P|]} ,\qquad(4)$$

Where m_T, m_B, and m_P are the largest, intermediate, and smallest principal components of the summed moment tensor. When the double couple component is dominant, the *fclvd* tends to be zero. Conversely, when the value approaches 0.5, the tensor is far from a double couple. The *clvd* proportion of the summed moment tensor can also be used to analyse the seismotectonics of a zone (e.g., Frohlich and Apperson, 1992; Jost et al., 1998; Buforn et al., 2004; Borges et al., 2007; Bailey et al., 2012).

Let's consider the composed moment tensor to be a representation of the seismic strain in a zone. We can use its orientation and characteristics to get insight into the deformation pattern of the studied tectonic zones. A first approximation is to consider the orientation of the principal strain axes. The T axis is equivalent to the extension axis, the P axis is comparable to the shortening axis, and the B axis is the intermediate axis, which can be neutral for a plane strain deformation (a pure double couple moment tensor) or it can be an extension or a shortening axis depending on the tectonics of the zone.

It is of interest to quantify the amount of seismic deformation occurring in each zone using the various rupture types. These different rupture processes within a zone cannot be considered to reflect temporal changes in the regional deformation field, as the time interval of the catalogue is very short; instead, they are likely due to local strain axis permutations. To quantify these changes in the orientation of the axes between rupture types, we resort to the minimum rotation angle between tensors (or Kagan angle; Kagan, 1991). The angle for a pure axis permutation maintaining the orientation of all the axes would be 90°. In practice, if we consider the angle between the focal mechanisms of different types of rupture and given that they nucleate in faults with different orientations, this angle may depart slightly from 90º.

Finally, to analyse the shape of the seismic deformation tensor, we can adapt the Flinn diagram for 3D strain tensor shapes used in classic structural geology analysis. The Flinn diagram represents the relation between the principal strain axes, or principal extension (Flinn, 1958), where the abscissa is the relation $\hat{s}_2/\hat{s}_3$ and the ordinate the relation $\hat{s}_1/\hat{s}_2$. An alternative to these values was proposed by Ramsay (1967), who suggested the use of the natural logarithm of these relations so that:

$$ln[\hat{s}_1/\hat{s}_2] = \varepsilon_1 - \varepsilon_2 ,\qquad(5)$$

$$ln[\hat{s}_2/\hat{s}_3] = \varepsilon_2 - \varepsilon_3,\qquad(6)$$

where ε_1, ε_2 and ε_3 are the natural strains of the largest, intermediate, and smallest principal strain axes of the deformation ellipsoid, i.e. the magnitude of the changes in the length of the axes. Similarly, the principal strain axes of the combined seismic moment tensors can be considered the amount of seismic strain change induced by the earthquakes in a volume. Consequently, the logarithmic Flinn diagram can be adapted to this purpose. Additionally, the shape of the ellipsoid can also be defined by the *k*-value, which is defined as

$$k = \frac{\varepsilon_1 - \varepsilon_2}{\varepsilon_2 - \varepsilon_3} ,\qquad(7)$$

This parameter has values of 0 for oblate strain shape, 1 for plane strain and ∞ for prolate strain shapes. In the case of seismic moment tensors, a pure double couple has the form

$$\begin{bmatrix} M_0 & 0 & 0 \\ 0 & 0 & 0 \\ 0 & 0 & -M_0 \end{bmatrix}, \tag{8}$$

having the values of the principal axes the same magnitude although of opposite sign to conserve the volume. Strictly speaking, a double couple corresponds to a plane strain ellipsoid with no strain on the orthogonal plane to the maximum and minimum moment axes $m_T=-m_P$, $m_B=0$. If the intermediate moment axis is different from 0, then the compensated linear vector dipole component appears as shown in equation 3.

To represent the combine seismic moment tensors in the Flinn diagram we defined the ordinate and abscissa as $M_1 - M_2$ (or $m_T - m_B$) and $M_2 - M_3$ (or $m_B - m_P$) respectively, where $M_1 \geq M_2 \geq M_3$ (we used the logarithm of these values to improve the data presentation). The shape of the tensor can then be defined in an equivalent way as in equations (5 and 6):

$$k = \frac{M_1 - M_2}{M_2 - M_3}, \tag{9}$$

3.2 Kinematic analysis. Slip Model

Focal mechanisms provide valuable insights into earthquake rupture kinematics, including the strike, dip, and rake of the two nodal planes. However, most of the time, the selection of the true fault plane among the two possible ones is not straightforward. The strain orientation derived from thrust or normal faulting focal mechanisms may remain the same irrespective of the true fault plane, but the dip direction of the fault would not be constrained. On the other hand, for strike-slip faulting focal mechanisms, the strike of the fault plane is crucial to define the strain field properly.

The Slip Model (Reches, 1983; de Vicente et al., 1988) identifies which of the nodal planes is more prone to slip from a mechanical point of view, as it requires less energy to mobilize (the neoformed plane, not a reactivated one). The Slip Model proposed by Capote et al. (1991), based on de Vicente (1988) and Reches (1983), defines the maximum shortening trend (D_{ey}, E_{Hmax}) and the shape factor (k') of the deformation ellipsoid for each focal mechanism.   Thus, areas under similar strain conditions can be readily defined, improving the results of stress inversion, based on plane populations. In this study, we apply the workflow suggested by de Vicente et al. (2008), Olaiz et al. (2009), and Arcila and Muñoz-Martín (2020). This method, based on the Navier–Coulomb fracture criterion, assumes that the brittle strain and stress axes are parallel and that one of the axes is close to vertical. According to the Slip Model, under the triaxial strain conditions of brittle strain, fractures are arranged in orthorhombic symmetry concerning the fundamental axes of the strain ellipsoid.

$$k' = e_y/e_z, \tag{10}$$

where e_z is the axis of the vertical strain and e_y is the axis of the maximum horizontal shortening

Accordingly, replacing e_y and e_z in equation (10):

$$k' = (sin^2 D cos^2 B)/(1 - sin^2 D cos^2 B), \tag{11}$$

$$B = sin^2 D cos^2 P \, ,\tag{12}$$

where D is the dip and P the pitch of the slip vector on the fault plane.

Two sequences of strain are established as a function of k', from reverse to normal through strike-slip faulting, and k' is rescaled to plot values continuously (Table 2).

$k' = \infty$	Plane strain	Pure strike-slip (Pitch =0)
$\infty > k' > 1$	Shear with extension	Strike-slip normal
$k' = 1$		
$1 > k' > 0$	Extension with shear	Normal strike-slip
$k' = 0$	Plane strain	
$0 > k' > -0.5$	Radial extension	Pure normal (Pitch = 90)
$k' = -0.5$	Pure radial extension	
$k' = -0.5$	Pure radial shortening	
$-1 > k' > -0.5$	Radial shortening	Pure reverse (Pitch = 90)
$k' = -1$	Plane strain	
$-2 < k' < -1$	Shortening with shear	Reverse strike-slip
$k' = -2$		
$-\infty < k' < -2$	Shear with shortening	Strike-slip reverse
$k' = -\infty$	Plane strain	Pure strike-slip (Pitch = 0)

Table 2: k´ values obtained from the Slip Model

Additionally, based on the relationship between D and P proposed by de Vicente (1988), when the nodal plane coincides with the character of the focal mechanism, frictional energy is dissipated more efficiently. Therefore, the selected plane can be effectively utilised in stress inversion methods that rely on fault planes orientations and their associated slip directions (Angelier and Mechler, 1977). Hence, the quality of the stress inversion results is improved compared to those obtained using both planes (neoformed and reactivated) (Michael, 1987; de Vicente, 1988; Giner-Robles et al., 2006).

3.3 Dynamic analysis, stress inversion

For the stress inversion, we apply the method proposed by Reches et al. (1992). The process incorporates two constraints: first, the stresses in the slip direction satisfy the Coulomb yield criterion; and second, the slip occurs in the direction of maximum shear stress along the fault. The computations yield the complete stress tensor, normalised by the vertical stress, and evaluate the mean coefficient of friction (μ) and the mean cohesion (C) of the faults during the time of faulting (Reches, 1987). Thus, for every selected population, two angular quality criteria are obtained: the slip misfit (SLIP), which is the mean angle between the observed and calculated slip axes of all faults in the cluster, and the principal angles misfit (PAM), which is the angle between the ideal stress axes of each nodal plane and general stress axes of the entire group according to the optimal mechanical condition for faulting (Reches, et al., 1992). In addition, the stress ratio (R) is established as proposed by McKenzie (1969), Etchecopar et al. (1981), Gephart and Forsyth (1984), Delvaux et al. (1997), among others (Equation 13, Table 3).

$$R = (\sigma_2 - \sigma_3)/(\sigma_1 - \sigma_3)\tag{13}$$

To assess the statistical representativeness of the population of focal mechanisms within each tectonic zone, a Monte Carlo bootstrapping approach was employed to determine the value of the friction coefficient with the least errors. This technique enables us to determine the potential variability of the principal stress axes, particularly the possible permutations between two principal stress axes when they have similar magnitudes.

R		Stress Regime	Vertical axis
R=1	$\sigma_1 = \sigma_2 > \sigma_3$	Radial Thrusting	σ_3
$1 > R > 0$	$\sigma_1 > \sigma_2 > \sigma_3$	Triaxial Thrusting	σ_3
R = 0	$\sigma_1 > \sigma_2 = \sigma_3$	Uniaxial Thrusting	σ_3
$0.5 > R > 0$	$\sigma_1 > \sigma_2 > \sigma_3$	Strike-slip Thrusting	σ_2
R = 0.5	$\sigma_1 = \sigma_2 > \sigma_3$	Pure Strike-slip	σ_2
$1 > R > 0.5$	$\sigma_1 > \sigma_2 > \sigma_3$	Strike-slip Normal	σ_2
R =1	$\sigma_1 = \sigma_2 > \sigma_3$	Uniaxial Normal	σ_1
$1 > R > 0$	$\sigma_1 > \sigma_2 > \sigma_3$	Triaxial Normal	σ_1
R =0	$\sigma_1 > \sigma_2 > \sigma_3$	Radial Normal	σ_1

Table 3: Relation between stress tensor (R shape factor ratio) and the stress regime.

4. Tectonic zonation for stress-strain analysis

To define the tectonic zones required for stress inversion and strain analysis, we utilise the Slip Model (De Vicente et al., 1988). This model provides unique values of the shape factor (k') and the orientation of the shortening (or minimum extension) axis (D_{ey}) for each focal mechanism. Interpolation of these values enables the generation of continuous maps that show the variation of both parameters (e.g., de Vicente et al., 2008; Olaiz et al., 2009; Arcila and Muñoz-Martín, 2021). In this study, we built interpolated maps of the shape factor (k') and the value for D_{ey} using the blockmean module of the Generic Mapping Tools (Wessel and Smith, 1991; Wessel et al., 2013). The shape factor (k') is a scalar that varies between 0 and 300. Therefore, the values are normalised to the average for each node and subsequently interpolated onto a continuous surface. These maps are a powerful tool for better defining different strain regions based on homogeneous shape factor values and similar D_{ey} trends. Thus, the grouping of the focal mechanisms is straightforward, allowing for the optimisation of results for techniques designed for populations.

The three fundamental pieces of information that we considered for the delineation of the tectonic zones in the Iberian Peninsula are (a) the available information on the neotectonic (in this case, Alpine) structural deformational style (Fig. 1), (b) the density of the available data (Fig. 2), and (c) the dominant type of focal mechanism. The global and interpolated analysis of the data using the Slip Model allows us to consider these parameters simultaneously (Figs. 3 and 4). Different search radii have been tested to balance highly populated areas and those containing isolated information, while maximizing the overall data representation.
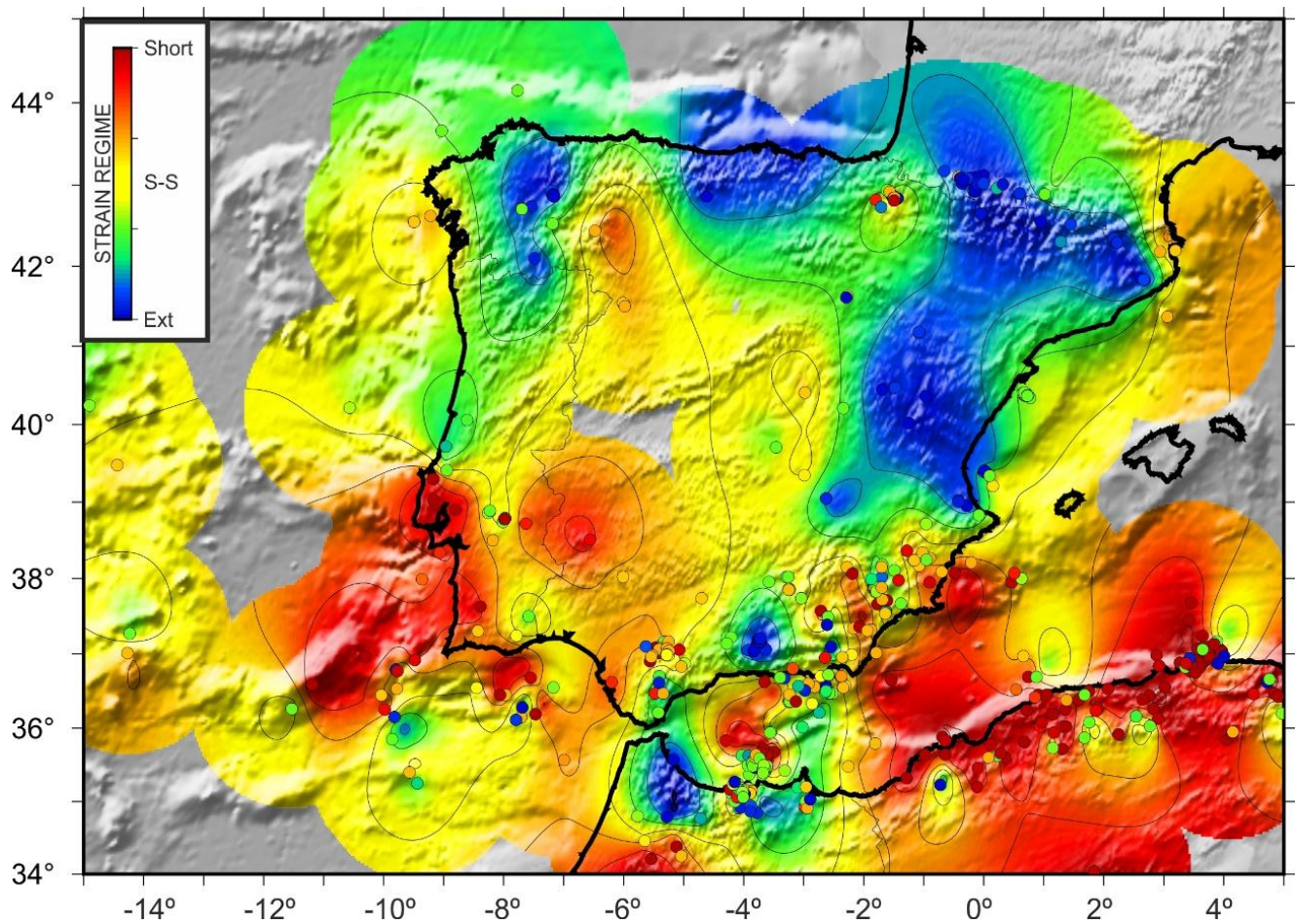
275 **Figure 3: Style of active deformation (strain regime) for Iberia determined from focal mechanisms. The map shows the shape factor (k´) determined using the Slip Model (Reches, 1983 and de Vicente, 1988). Each dot represents a focal mechanism. Search radius of 150 km. Short.: shortening. S-S: shear strain. Ext.: extension.**
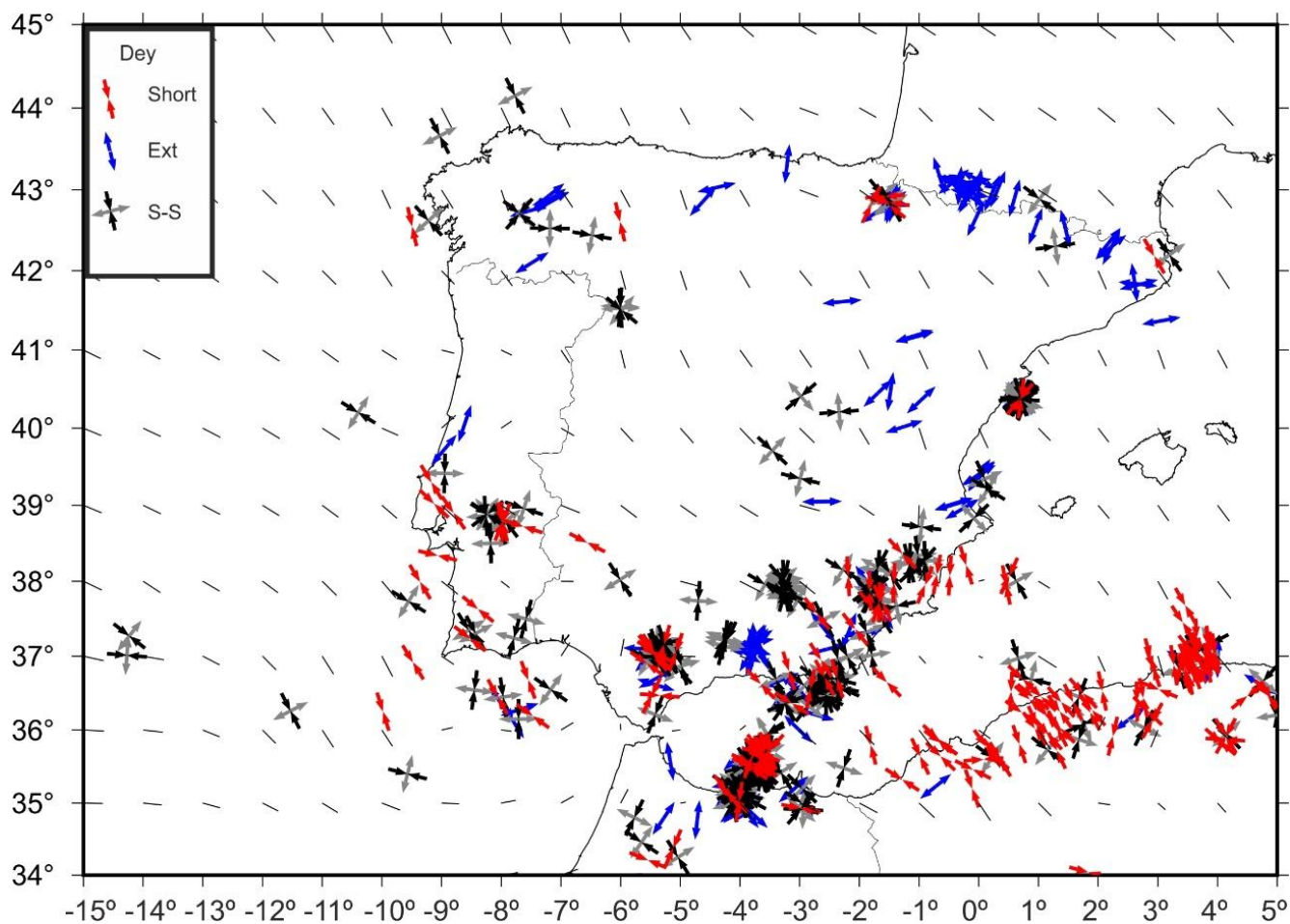
Figure 4: Solutions of the Slip Model (by assuming that one principal strain axis is vertical) for all analysed focal mechanisms. Short, and Ext denote the principal horizontal shortening and extension axes, respectively, and S-S the shear strains. Black bars are Dey (E_{Hmax}) trend interpolations.

Considering these criteria, we subdivided Iberia into the following zones (Fig. 5):

In the Pyrenees, we identified three zones: the Central Pyrenees (CP), characterised by mostly normal faulting focal mechanisms, and two additional zones at the eastern and western ends, where there are more focal mechanisms: the Western Pyrenees (WP) and the Eastern Pyrenees - Northern Catalan Coastal Range (EPCE). Further west, on the north edge, we grouped the earthquakes in North-Western Galicia (NWG), with numerous focal mechanisms in the central area, as well as offshore. In the east of the peninsula, offshore near the coast, we have differentiated two tectonic zones: the Western Valencia Trough (WVT) and the South Valencia Trough (SVT).. Onshore, we have separated the focal mechanisms in the Iberian Chain (IC) and south of the eastern SPCS (Central Basins, CB), as well as those in the tectonic zone near Lisbon, which we refer to as the Western Central System (WCS). Further south but not yet at the active plate boundary, we defined the Algarve (AL) as a tectonic zone. In the offshore Atlantic to the west, although the data are very scattered, the focal mechanisms are similar, and several correspond to earthquakes that occurred at mantle depths but are not well-constrained. Therefore, we grouped them in

the tectonic zone Offshore Atlantic (OA). Further south, primarily offshore and along the plate boundary, we examined the Gorringe-Horseshoe (GH) and Gulf of Cádiz (GC) tectonic zones. The large number and variability of focal mechanisms in the Betics require smaller tectonic zones. Thus, considering the predominance of normal faulting in the Granada Basin (GB), we differentiated the Western Betics (WB) to its west, the Betics Antequera (BA) to its north, and Western Alcaraz Arch (WAA) and the Eastern Betics (EB) to its east. In the Alboran Sea, we considered the North Alboran (NA), which also has onshore focal mechanisms, and the Alboran Ridge (AR), located at the probable plate boundary. Further south, on the African Plate, in the Rif, we considered the tectonic zones of Al Hoceima (ALH) and Rif (RF). Finally, in the Algerian Atlas, we analysed two populations: one located further east, the Eastern Tell Atlas (ETA), and the other located further west, the Western Tell Atlas (WTA). Fig. 5 shows the focal mechanisms in different colours for each area. We utilized the Rif (RF) focal mechanisms in the Slip Model analysis (Figs. 3 and 4). However, any stress inversion yielded a high-quality solution, and therefore, we will not comment on RF active tectonics (Fig. 5).
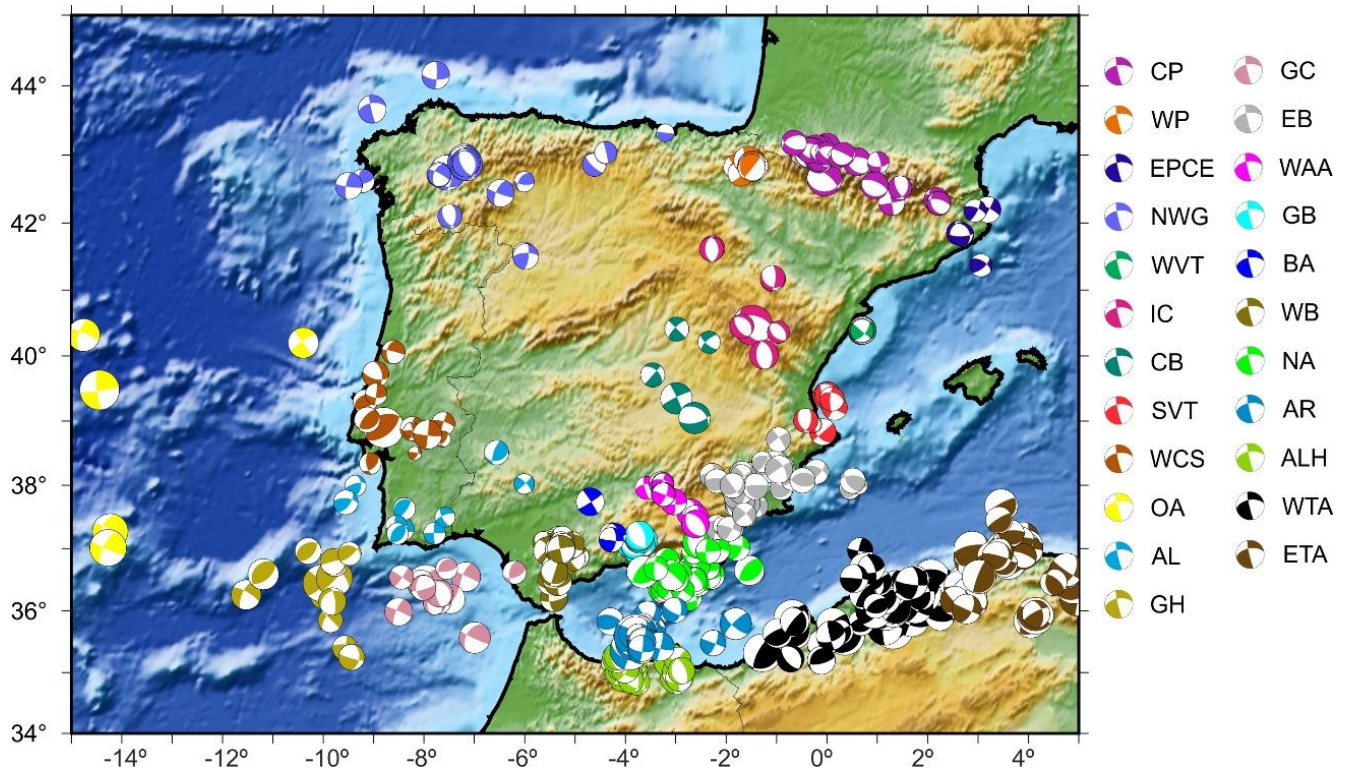
Figure 5: Color-coded focal mechanisms for every considered tectonic zone: Central Pyrenees (CP); Western Pyrenees (WP); Eastern Pyrenees-Northern Catalan Coastal Range (EPCE); North-Western Galicia (NWG); Western Valencia Trough (WVT); Iberian Chain (IC), Central Basins (CB); Western Spanish Portuguese Central System (WCS); Offshore Atlantic (OA); Gorringe-Horseshoe (GH); Southern Valencia Trough (SVT); Algarve (AL); Eastern Betics (EB); Western Alcaraz Arch (WAA); Granada Basin (GB); Northern Alboran (NA); Alboran Ridge (AR); Al Hoceima (ALH); Western Tell Atlas (WTA); Eastern Tell Atlas (ETA); Gulf of Cádiz (GC); Western Betics (WB); Betics Antequera (BA).

5 Results

The results obtained following the methodologies described above are summarised in Tables 4 and 5 for all considered tectonic zones. For additional information, see Appendices A and B.

Label	Population	Combined Seismic Moment Tensor main axes						Rupture type	fclvd	k value	Minimum Rotation Angle (°)		
		P trend	P plunge	B trend	B plunge	T trend	T plunge				N-SS	SS-R	R-N
CP	Central Pyrenees	163	76	**296**	10	28	10	N	-0.10	1.39	88.6	-	-
WP	Western Pyrenees	**99**	21	287	69	190	3	SS	-0.31	3.52	82.1	74	72.7
EPCE	Eastern Pyrenees	**344**	17	129	70	251	11	SS	-0.28	2.98	76.1	-	-
NWG	NW Galicia	**328**	14	138	76	237	2	SS	-0.34	4.09	78.5	43.8	98.4
WVT	Western Valencia Trough	**2**	29	143	54	262	19	SS-N	0.06	0.84	16.3	25.6	25.5
IC	Iberian Chain	309	86	**154**	4	64	2	N	0.04	0.89	-	-	-
CB	Central Basins	**276**	6	31	77	185	12	SS	-0.26	2.58	70.3	-	-
WCS	Western SPCS	**323**	3	229	60	55	30	SS-R	0.29	0.33	44.9	71.7	99.4
OA	Offshore Atlantic	**152**	22	297	64	57	14	SS-N	0.03	0.92	-	-	-
GH	Gorringe-Horseshoe	**164**	15	44	62	260	23	SS-R	0.33	0.26	49.6	68.7	90.2
SVT	Southern Valencia Trough	18	73	**157**	13	249	11	N	-0.25	2.56	74.1	-	-
AL	Algarve	**143**	6	31	75	234	14	SS	0.41	0.13	80.3	-	-
EB	Eastern Betics	**352**	15	119	67	258	18	SS-R	0.22	0.46	46.7	83.6	71.4
WAA	W Alcaraz Arch	**143**	3	333	87	233	0	SS	-0.23	2.30	87	-	-
GB	Granada Basin	250	76	**139**	5	48	13	N	0.08	0.77	-	-	-
NA	Northern Alboran	**334**	6	217	76	66	12	SS	-0.15	1.63	88.3	49.7	100
AR	Alboran Ridge	**337**	20	173	70	69	5	SS	0.19	0.52	64.8	76.4	98.4
AH	Al Hoceima	**329**	24	157	65	60	3	SS-N	-0.08	1.30	50.8	58.2	76.6
WTA	Western Tell Atlas	324	15	231	10	108	71	R	0.29	0.33	67.4	80.4	105.5
ETA	Eastern Tell Atlas	336	26	69	8	175	63	R	0.08	0.77	77.8	73.5	96.3
GC	Gulf of Cádiz	**161**	15	291	67	66	17	SS-R	0.24	0.42	91.9	66.6	94.4
WB	Western Betics	332	11	235	31	79	57	R-SS	0.20	0.50	35.9	58.6	59.9
	Western Betics > 20 km	**299**	18	81	67	205	13	SS-N	0.22	0.44	80.4	90.1	105.8
BA	Betics Antequera	**305**	30	101	58	209	11	SS-N	-0.05	1.16	-	-	-

315   Table 4: Summary of the combined seismic moment tensor results for all considered zones. Bold numbers represent the trend of the greatest horizontal shortening axis (E_{Hmax}), and underlined numbers represent the trend of the greatest horizontal extensional axis.

Label	Tectonic zones	Dey	SHmax	σ1 tr	σ1 pl	σ2 tr	σ2 pl	σ3 tr	σ3 pl	R	Fric	Cohe	N/Nad	PAM	SLIP
CP	Central Pyrenees	119±12	121.5	196	83	121	1	3	4	0.35	0.6	0.0187	28/28	23.11	17.7
WP	Western Pyrenees	101±24	98.6	90	59	103	31	190	6	0.7	0.1	0.0351	12/14	33.63	30.15
EPCE	Eastern Pyrenees	166±20	165.1	349	48	158	41	253	6	0.42	0.3	0.0312	6/6	36.1	21.1
NWG	NW Galicia	155±14	147.8	290	79	150	9	59	5	0.6	0.4	0.0354	17/21	17.96	27.53
WVT	Western Valencia Tr	0±14	170.8	359	35	125	39	245	31	0.34	0.2	0.0096	11/12	15.92	9.99
IC	Iberian Chain	166±9	141.8	54	87	148	0	238	3	0.43	0.1	0.0114	8/8	24.37	16.44
CB	Central Basins	78±12	84.3	270	55	80	34	173	4	0.61	0.4	0.0055	6/6	23.33	6.19
WCS	Western SPCS	140±19	137.2	134	13	209	50	54	37	0.38	0.1	0.0451	20/20	33.65	29.29
OA	Offshore Atlantic	140±28	133.9	151	15	166	72	44	10	0.92	0.1	0.0059	5/5	18.75	2.97
GH	Gorringe-Horseshoe	133±26	157.3	159	24	251	5	352	65	0.41	0.1	0.0204	8/13	38.82	11.3
SVT	Southern Valencia Tr	166±21	147.8	129	80	149	9	238	3	0.5	0.1	0.0029	8/10	20.72	6.69
AL	Algarve	117±20	146.3	140	17	334	72	232	4	0.14	0.6	0.0658	11/11	38.22	14.681
EB	Eastern Betics	163±18	169.1	171	13	112	66	256	20	0.35	0.01	0.0033	47/47	31.13	29
WAA	W Alcaraz Arch	160±13	152.5	153	8	325	82	62	1	0.8	0.6	0.0614	14/14	22.43	16.13
GB	Granada Basin	136±13	119	263	84	123	6	33	5	0.11	0.5	0.0152	16/16	18.92	14.72
NA	Northern Alboran	163±20	151.2	149	14	187	72	62	10	0.73	0.01	0.0024	42/42	28.12	24.24
AR	Alboran Ridge	166±17	161.8	161	22	159	68	251	1	0.34	0.01	0.0023	62/62	26.79	19.8
AH	Al Hoceima	147±17	153.6	152	36	159	54	64	4	0.69	0.1	0.0186	41/41	21.63	19.77
WTA	Western Atlas	146±15	145.3	145	12	199	71	58	15	0.14	0.2	0.0366	44/44	25.99	16.83
ETA	Eastern Atlas	166±17	145.6	149	20	164	13	185	65	0.4	0.01	0.0032	52/52	25.52	23.09
GC	Gulf of Cádiz	148±12	147.7	150	5	251	64	58	25	0.19	0.1	0.0144	10/12	23.09	16.14
WB	Western Betics	148±22	140.7	139	16	212	45	63	40	0.18	0.1	0.031	28/28	28.68	24.54
	Western Betics > 20 km	148±14	78.7	114	17	113	72	204	0	0.26	0.01	0.0041	6/7	24.27	23.28
BA	Betics Antequera	102±11	104.8	105	3	109	87	15	0	0.91	0.7	0.0061	5/5	13.04	7.97

Table 5: Summary of the stress inversion results for all considered zones. Dey defines the maximum shortening trend from the Slip Model. S$_{Hmax}$ is the maximum horizontal stress (σ$_1$ or σ$_2$ with radial normal faulting stress regime). R represents the stress ratio. Tr

is the trend of the axis, and pl is the plunge of the axis. N denotes the number of events, and Nad is the number of events for the given solution (adjusted). PAM is the principal angles misfit, and SLIP is the slip misfit.

5.1 CP Central Pyrenees

The majority of the focal mechanisms in this area are predominantly normal, although some strike-slip faults are also observed. The seismic moment release is controlled by the normal fault events giving rise to a combined moment tensor close to a double couple, with a *k* value of 1.39 and an *fclvd* of 0.1. The Kagan angle between the combined moment tensors of normal and strike-slip earthquakes has a value close to 90°, indicating an almost pure permutation between the B and P axes. The orientations of the principal strain axes (T and B) are consistent with each other and orthogonal to the strike of the mountain range. However, these axes show some variability with two predominant families, one N020-030°E and the other N040-050°E, which could indicate the activation of normal fault families with slightly different orientations (see Appendix A).

The 28 focal mechanisms located in the central part of the Pyrenees provide a very consistent stress inversion solution (Fig. 7 CP) that indicates a nearly uniaxial normal faulting stress regime, with a σ_3 direction of N005-030°E, sub-perpendicular to the topographic axis of the range. The solution agrees with that obtained by de Vicente et al. (2009) and Asensio et al. (2012). The latter authors also analysed GPS data with similar results (extension perpendicular to the range of 2.5±0.5 nanostrain yr-1), which they attributed to post-orogenic collapse. This normal faulting stress regime would account for the seismic activity of the main active normal faults present in the area, such as the Lourdes Fault (1, Fig. 1), which has a 50 km trace and a 50 m high fault scarp (Alasset and Meghraoui, 2005; Lacan and Ortuño, 2012), as well as those of Bedous, Laruns, Pierrefitte, and Pic de Midi du Bigorre (Lacan, 2008) (2, Fig. 1). The latter authors attribute the seismicity in this part of the Pyrenees to a process of isostatic adjustment. In this area, we also include the focal mechanisms in the easternmost part of the area, obtained close to the Têt Fault (3, Fig. 1), which is 120 km long and accommodated right-lateral movement from the Miocene to the Upper Pliocene (Cabrera et al., 1988), and which during the Pliocene-Quaternary seems to have had mainly extensional movement (Briais et al., 1990). In any case, the three nearby focal mechanisms show normal faulting, consistent with the other mechanisms used for the inversion. Recent studies, calculated with polarities and temporary seismic networks, provide very similar focal mechanisms (Ruiz et al., 2023).

5.2 WP Western Pyrenees

Seismicity in the western Pyrenees is clustered in the south of the mountain range, in the vicinity of the city of Pamplona. This seismic activity is characterised on the one hand by normal faulting, with a strike-slip component, and on the other by a series of oblique events with a significant strike-slip displacement. This component is essential in the area, with the combined moment tensor having mainly shearing characteristics, although with *fclvd* values of 0.31 and a *k* of 3.52, which indicates a prolate-type seismic deformation tensor shape. The strain extensional axis of the combined mechanism is N011°E, and that of maximum horizontal shortening (B and P permuting) is between N090°E-N110°E.

The stress inversion (Fig. 7 WP) also results in a normal faulting stress regime, as in CP (N098°E). However, the stress tensor shows characteristics closer to strike-slip, with σ_2 at N103°E, which allows activating WNW-ESE to E-W normal faults, such as those of Leiza, Aralar, and Roncesvalles (Lacan and Ortuño, 2012), but also NE-SW strike-slip faults, such as the Pamplona Fault (4, Fig.1), which is 125 km long (Ruiz et al., 2006). This is a vertical fault, inherited from the Late Variscan period, which also controlled Mesozoic and Tertiary sedimentation (Ruiz et al., 2006) and was reactivated as an oblique ramp during the Pyrenean shortening (Vergés, 2003).

5.3 EPCE Eastern Pyrenees-Northern Catalan Coastal Range

This tectonic zone, which contains only six focal mechanisms, was differentiated from the Central Pyrenees population because, here, as in the westernmost part, there seem to be more strike-slip faulting mechanisms (as opposed to the easternmost ones). Half of the population, with epicentres close to the axis of the mountain range, present pure normal faulting mechanisms, while the other half has a thrust faulting component. The Kagan angle between the combined normal and strike-slip faulting mechanisms is close to 80°, suggesting a permutation between the P and B axes. The combined moment tensor departs from a pure double couple, with an *fclvd* of 0.28 and a *k*-value of 2.98. The shape of the ellipsoid is therefore of prolate type, with the strain axis oriented at N72°E and the maximum shortening almost horizontal at N163°E.

The stress inversion (Fig. 6 EPCE) indicates a more normal faulting stress regime (σ_2 at N165°E) concerning CP, similar to that obtained by Goula et al. (1999) with normal strike-slip stresses, which differs from the one provided by these authors, which was more thrusting. The onshore focal mechanisms would indicate that the structures associated with the recent NW-SE Olot volcanism, the Amer and Empordà faults (5, Fig. 1) (Souriau and Pauchet, 1998; Lacan and Ortuño, 2012) present normal-type movements, which would have been responsible for the seismic crisis between 1427 and 1428 that caused considerable damage (Olivera et al., 2006). Active faults further south, in the Catalan Coastal Range, such as El Camp (6, Fig. 1) (Masana, 1996), Montseny, and Pla de Barcelona (7, Fig. 1) (Perea et al., 2020), seem to be more closely related to the opening of the Valencia Trough than to the Pyrenees. The El Camp Fault can be considered as part of the NVT. In any case, the stress solution is very similar to those found to the south in IC, WVT, and SVT, so it seems to be less related to the local processes affecting the Pyrenees.

5.4 NWG North-Western Galicia

The Pyrenean orogen spans across northern Iberia to the Cantabrian Mountains (Cantabrian Pyrenees), Galicia and offshore, as far as the Galicia Bank (Fig. 1). The southern part of the Bay of Biscay, the closest to Iberia, also appears to be affected by the deformation of the Pyrenees (e.g. Boillot and Malod, 1988) where the shortening took place from the Upper Eocene to the Middle Miocene (Gallastegui and Pulgar, 2002). After the Middle Miocene, much of the neotectonic activity in Galicia and Northern Portugal was concentrated in the left-lateral strike-slip NNE-SSW fault system of Vilariça-Bragança (8, Fig. 1),

Règua-Verín (9, Fig. 1), and Monforte-Orense (10, Fig. 1) (Cabral, 1989; de Vicente & Vegas, 2009; Martín González et al., 2012), which, although not strictly a part of the Pyrenees, are closely related to its evolution, as well as to that of the SPCS.

The focal mechanisms in this zone can be grouped into two families, one of normal faulting type, releasing most of the seismic moment, and the other of oblique strike-slip faults, some with normal components and others with reverse faulting components (see Appendices A and B). By using the Kiratzi & Papazachos (1995) approximation, which gives equal weight to all combined events in the tensor, we avoid the dominance of events with a much higher energy release than the others. The resulting combined moment tensor shows a prolate form, with k values close to 7 and an $fclvd$ of 0.39, dominated by ENE-WSE extension. The strain axes are very coherent in all focal mechanisms, with the combined one having an orientation of N057°E. In the horizontal shortening axes (P and B permuting with a rotation angle of 84°), there is more variability, with the P axis showing an orientation of N147°E.

The 18 focal mechanisms included in the stress inversion (Fig. 6 NWG) are of strike-slip and normal-directional types, resulting in a normal faulting stress regime, with a σ_2 strike between N147°E and N150°E. It should be noted that the most normal faulting mechanisms are concentrated in the area where small sedimentary basins developed during the Miocene, specifically in the interior of Galicia (de Vicente et al., 2011). In contrast, the offshore region is dominated by strike-slip faulting.

We were only able to obtain one focal mechanism in the Cantabrian Mountains (Cantabrian Pyrenees), which shows NW-SE normal faulting. This focal mechanism could indicate that critical faults in that orientation, such as the Ventaniella-Ubierna faults (11, Fig. 1), accommodate normal faulting deformation today. A study using a local seismic network (10 stations) on the Ventaniella Fault determined focal mechanisms for earthquakes with $M_w < 2$, but without obtaining a consistent pattern (López-Fernández et al., 2018); therefore, the results in this area are not conclusive. The two focal mechanisms with the highest double-couple component (above 80%) calculated by del Pie Perales (2016) are normal faulting solutions, and the focal nodal planes are compatible with the strike-slip fault system. Recently, on September 30th, 2023, a Mw=3.6 thrusting focal mechanism was reported by the IGN in Villamejil (León).

5.5 WVT Western Valencia Trough

The Valencia Trough, between the Mediterranean margin of Iberia and the Balearic Islands, shows a complex succession of partially inverted Mesozoic rifting events during the Cenozoic (Etheve et al., 2018). During the last 30 Myr, the emplacement of the Calabrian-Tyrrhenian subduction zone with trench retraction and back-arc extension produced intense extension in the Levantine sector of Iberia (Faccenna et al., 2004) during the Neogene (Roca and Guimerà, 1992), forming a broad rifting zone with the development of many horsts and grabens. This extension is moderately active today (Perea et al., 2020).

The Castor CO_2 storage project generated a sequence of apparently triggered seismicity. In addition to the moment tensors calculated by the IGN, several groups published focal mechanisms (Cesca et al., 2021; Villaseñor et al., 2020). The moment tensors present mainly similar solutions in both studies, in terms of plane orientations, although the depth and epicentral

location vary significantly. Due to the better epicentral relationship with the previously identified NE-SW striking faults, the results used here were those by Villaseñor et al. (2020). These mechanisms exhibit strike-slip fault displacements with a substantial normal component, very similar to those obtained by Goula et al. (1999) for the 1991 and 1995 events, based on P-wave polarities. The combined moment tensor shows an N082°E trending T axis and an immersion of 19°. The P axes show somewhat more scatter; still, the P axis of the combined moment tensor is oriented N002°E, with an immersion of 28°. The value of k obtained is 0.8, which indicates an oblate-type tensor shape, with N-S shortening and E-W extension.

The stress inversion of the 12 focal mechanisms (Fig. 6 WVT) yields a very consistent solution, indicating a normal faulting stress regime compatible with strike-slip and σ_2 oriented N170°E. This stress regime activates moderately dipping NE-SW and NW-SE faults, such as those of the Gulf of Rosas (12, Fig. 1), the Amposta Basin (13, Fig.1), Cape Cullera (14, Fig. 1), and the Columbretes Basin (Perea et al., 2020), which affect Pliocene-Quaternary sedimentary units (Perea et al., 2012). Onshore, the El Camp Fault (6, Fig. 1) (Masana, 1996) can also be activated by this type of stress. The stress solution for this zone is very similar to that of the SVT.

5.6 IC Iberian Chain

The IC is part of the Iberian intraplate orogen, characterised by a main Oligocene-Early Miocene age of deformation, which involved the inversion of Permian-Mesozoic rifts (Álvaro et al., 1979). From the Late Miocene onwards, its activity is linked to the opening of the Valencia trough (Roca and Guimerà, 1992) and therefore shows a similar evolution to the WVT. To the west, the extension deactivated the thrusts that uplifted the SPCS north of Madrid. The recent extensional process formed Neogene-Quaternary basins associated with N-S to NW-SSE normal fault activity (Simón, 1989). The related stress field, based on recent fault data, indicates triaxial normal faulting, with σ_3 oriented ENE-WSW (Arlegui et al., 2005). The most important active faults are those bounding the Jiloca graben (15, Fig. 1) (Sierra Palomera, Calamocha, Daroca, Munébrega faults) and the Teruel graben (16, Fig. 1) (Sierra del Pobo, Valdecebro, and Concud) (Simón, 2020).

The eight focal mechanisms in this tectonic zone are normal faulting events, with a few showing a strike-slip component, which combined give rise to a pure double-couple tensor with a horizontal T-axis oriented N064°E and B-axis oriented N154°E. The individual moment tensors are divided into two distinct families (see Appendices A and B), with T- and B-axis rotations of about 30°, probably due to the activation of complementary normal fault families.

The focal mechanisms used for the stress inversion, located in the north and centre of the IC, yield a triaxial normal faulting stress regime solution (Fig. 6 IC), with σ_3 oriented N058°E, similar to that of the WVT and compatible with the results obtained from recent faults analyses (Arlegui et al., 2005). Thus, the active stress field can activate the aforementioned normal faults (Simón, 2020).

5.7 CB Central Basins

In central Iberia, south of the SPCS and west of the IC, in the Cenozoic basins of Madrid and La Mancha (CB), we find six focal mechanisms, mainly showing strike-slip and normal faulting. Most of the strike-slip solutions correspond to minor seismic moment releases. The combined moment tensor shows an *fclvd* of 0.25 and a value of *k* of 2.58, corresponding to a prolate-type tensor shape dominated by a strain axis oriented N005°E and an axis of maximum shortening nearly E-W oriented. The stress inversion of the focal mechanisms (Fig. 6 CB) indicates a normal faulting stress regime solution with a small strike-slip component, with σ_3 almost perpendicular to that obtained for the CI, at N173°E, which also differs from most of the considered areas. However, geodetic velocities derived from GPS data in this region indicate a clear westward displacement—assuming a fixed Eurasian reference frame—at rates of 2 to 3 mm/yr (Cannavò and Palano, 2016; Neres et al., 2018a). This motion contrasts with the NW–SE trend observed farther south. The results published by Khazaradze et al. (2018) further support a dominant strike-slip faulting regime. On the other hand, and as a differential element, the area is characterised by volcanism(Campos de Calatrava volcanism), mainly sodic alkaline and ultra-alkaline rocks, with radiometric ages between 4 Ma to less than 0.7 Ma (Ancochea and Huertas, 2021) (17, Fig. 1), which has been related to a gentle folding of the Iberian lithosphere and the presence of an anomalous low-density sub-crustal block below the volcanic zone (Granja Bruña et al., 2015). It is therefore possible that this recent volcanic activity somehow influences the calculated stress tensor. An edge effect related to large-radius extension and uplift in the CI cannot be ruled out (Casas-Sáinz and de Vicente, 2009), nor whether it is an indentation effect about the Betics (Vegas and Rincón-Calero, 1996).

5.8 WCS Western (Spanish, Portuguese) Central System

As mentioned before, the central orogenic belt extends to the west, reaching as far as Lisbon and offshore into the Estremadura Spur. In its Portuguese stretch, the SPCS is an active mountain range (Cabral, 2012). Documented structural damage from seismic events has and digitalized seismograms been used to convert observed effects into intensity estimates and moment magnitude calculations, as in the case of the 1909 Benavente earthquake, which reached Mw = 6.0 and exhibited a significant thrust faulting component. (Stich et al., 2005; Fonseca & Vilanova, 2010). The thrust faults have predominantly NE-SW strikes with associated NW-SE shortening (de Vicente et al., 2018). East of Portugal, in the westernmost Spanish sector, and along the NE part of the Messejana-Plasencia fault (18, Fig. 1), instrumental seismicity is scarce. However, there is evidence of end-Cenozoic and Quaternary deformation (de Vicente et al., 2022).

The focal mechanisms in this tectonic zone are predominantly reverse or strike-slip faulting events, the former showing a higher release of seismic energy. There are some normal faulting events whose T and B axes are kinematically compatible with each other. Considering the combined mechanisms of strike-slip and reverse faulting, we calculated the value of the minimum rotation angle close to 70°, thus constituting a T and B permutation. The orientation of the axis of maximum shortening of the combined moment tensor is N146°E, and the axis of maximum extension is oriented N056°E. The overall

combined moment tensor, considering all earthquakes in this zone, is of oblate type, with a low k value of 0.325 and an *fclvd*
of 0.29; thus, it is dominated by NW-SE shortening.

The stress inversion for this tectonic zone (Fig. 6 WCS) was computed using 20 focal mechanisms. It resulted in a clear thrust faulting stress regime solution with a small strike-slip component, with σ_1 oriented N134°E. This stress regime activates NE-SW striking thrust faults and left-lateral NNE striking and right-lateral ESE striking strike-slip faults. Examples include the Vilariça-Bragança (8, Fig. 1) and Régua-Verín (9, Fig. 1) faults, which exhibit left-lateral movement. Additionally, there are faults from S Galicia (NWG, with σ_2 at N150°E) to the Serra da Estrela (19, Fig. 1) with a thick-skinned tectonic style without tectonic inversion, and the SPCS (Cabral, 2012) with σ_1 at N134°E. The thrusts bordering the Lusitanian Basin to the south and the Cenozoic Lower Tagus Basin to the north are also active with kinematics that are directly related to the inferred stress tensor. Focal mechanisms to the east show mainly strike-slip faulting in the Arraiolos and Évora seismic zones (20, Fig. 1), within the Ossa-Morena zone of the Variscan basement, consistent with right-lateral motion on N065°E faults (Matos et al., 2018).
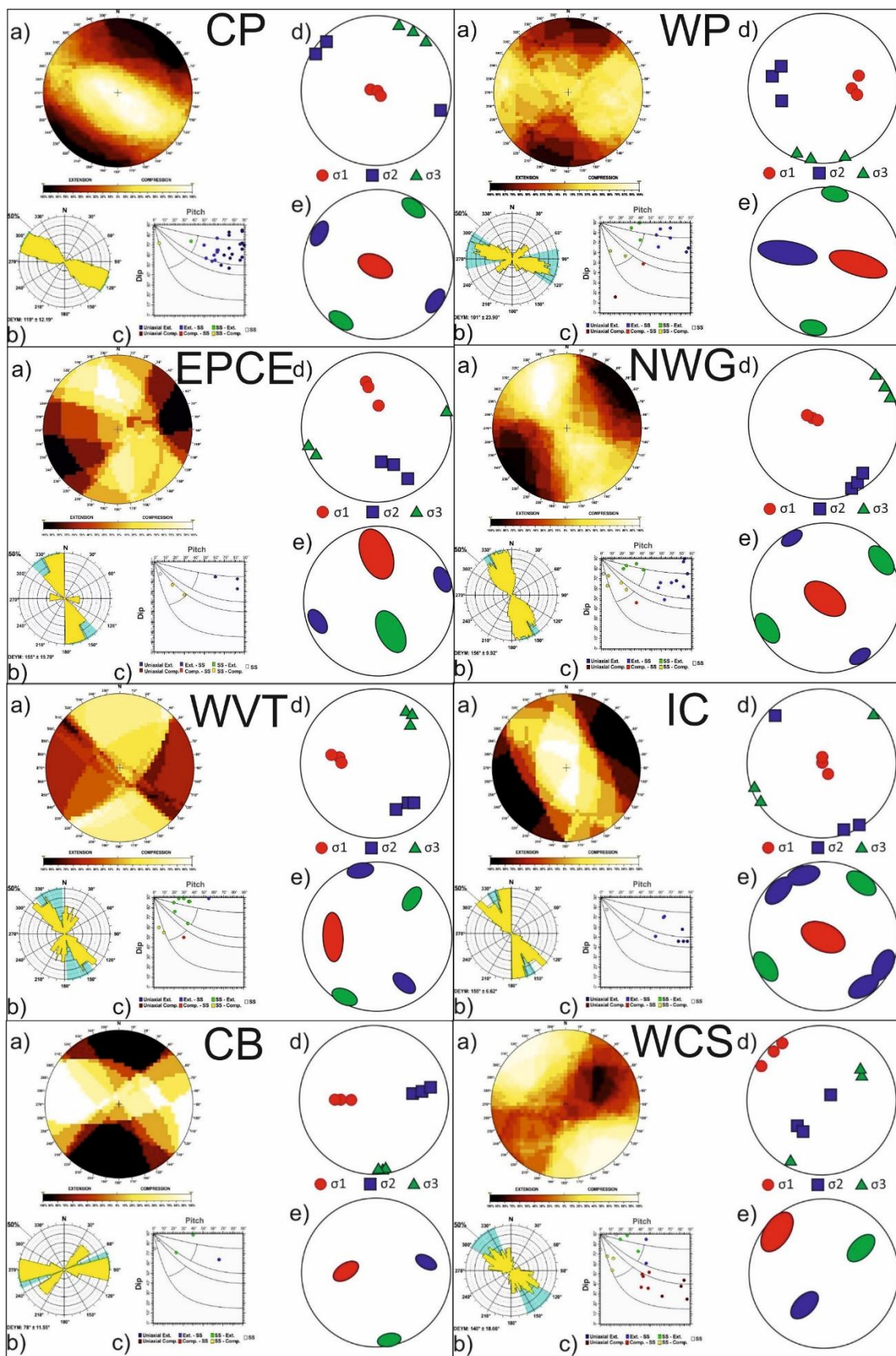
5.9 OA Offshore Atlantic

The focal mechanisms in the Atlantic offshore, to the north of the active plate boundary, are spatially scattered over a wide area, and some appear to be deeper than the Moho (although the mainland seismic networks poorly constrain the depth of these earthquakes). We grouped all these events based on their similar characteristics. Between the Tagus and the Iberian abyssal plains, there is a structural high, the Estremadura Spur, with E-W to NE-SW thrusts, which is the offshore extension of the SPCS, affecting the intermediate crust (Terrinha et al., 2009). Between this tectonic uplift and the Galicia Bank to the north, NNE-SSW faults seem to dominate, with kinematics similar to those onshore (Vilariça-Bragança (8, Fig. 1) and Régua-Verín (9, Fig. 1) fault systems). In the south, there are some focal mechanisms close to the Hirondelle structural high, to the north of the Gloria fault (21, Fig. 1). In the Estremadura Spur, an NNW-SSW shortening regime dominated the main structuring of the range during the Palaeocene-Miocene (Pereira et al., 2021). However, the most recent and active deformation appears to be transpressional (Neves et al., 2009).

There are six strike-slip focal mechanisms in this zone, some of which have a small normal component. These moment tensors show some variability in their principal axes, especially in the P axis. Therefore, the combined moment tensor presents k values below 1, an *fclvd* greater than 0 (Fig. 7 OA), and a tendency to have an oblate shape, with the P axis having a dominant N152°E orientation. The extension T-axis is in the N057°E direction. The stress inversion indicates a strike-slip stress regime with a normal component, characterised by σ_1 at N131°E and σ_3 at N044°E, which activates right-lateral ESE-WNW faults, such as the significant major strike-slip Gloria fault (21, Fig. 1) in the North Atlantic, which defines the present-day plate boundary between Eurasia and Africa.

5.10 GH Gorringe-Horseshoe

At the active plate boundary, and between the NE-SW structural highs (pop-ups and restraining steps with thick-skinned tectonic styles) of Gorringe and Horseshoe, there are 13 reverse and strike-slip focal mechanisms, several of which are below the Moho, that indicate a thrust-faulting stress regime (Fig. 7 GH) with σ_1 at N159°E. These focal mechanisms are mainly strike-slip with a vertical component and reverse faults with some horizontal component. There are also normal-type mechanisms whose T axes are kinematically compatible with the T axes of the other events. The orientations of the axes of maximum horizontal shortening and extension exhibit considerable variability, with the T axes giving rise to two well-differentiated families: one N040-060°E and the other N070-090°E (see Appendices A and B). The more E-W trending axes seem to be more associated with the strike-slip faults in the centre and south of the region, while the reverse fault events in the

northern part have NE-SW B-axis orientations. The combined moment tensor presents an oblate shape, dominated by shortening, with a k value of 0.623 and an *fclvd* of 0.14, indicating a significant distribution of deformation across different structures. The orientations of the P and T axes are N155°E and N65°E, respectively.

Deformation along the Gloria fault (21, Fig. 1) (zone OA) is purely strike-slip and locally transtensional. In contrast, between the Gorringe and Horseshoe tectonic uplifts (zone GH), it is compressional (Zitellini et al., 2009). The most prominent structure, the Gorringe Bank, is bounded by NE-SW crustal thrusts, the most significant one located on its northern edge. This structure was the source of destructive landslides during the Miocene, with renewed activity in the Pliocene-Quaternary period (Gamboa et al., 2021). Several earthquakes have hypocentres at upper mantle depths (>20 km), implying that the observed surface thrusts must be linked to structure at mantle levels (Grevemeyer et al., 2017). Active deformation has reactivated and inverted former Mesozoic normal faults (García-Navarro et al., 2005) and appears partitioned between NW-SE thrusts and WNW-ESE to W-E strike-slip faults (Terrinha et al., 2009). Further south, the Coral Patch Ridge shows a similar tectonic structuring (Martínez-Loriente et al., 2013). The inferred stress tensor activates pure NE-SW thrusts and right-lateral NW-SW reverse-strike-slip and WNW-ESE strike-slip faults, which may be the tear faults of the thrusts (Ferranti et al., 2014).

5.11 SVT Southern Valencia Trough

In the easternmost onshore part of the Prebetic front, on the undeformed foreland, Betic compression ceased approximately 10 Myr ago. This area is structured in a series of horsts and grabens, about 25 km long and 5 km wide (Navarrés, Tous) (22, Fig. 1), which triggered a diapirism of the Triassic salt (Keuper facies) when the extension associated with the opening of the Valencia Trough was imposed in the area (De Ruig, 1995). The primary trend of the grabens is perpendicular to the Betic front (NW-SE), although there are also parallel grabens, indicating triaxial extension. Their position explains why they are not plug-type diapirs, but rather linear ones, which were controlled by multiple faulting episodes (Jackson and Hudec, 2017). The diapirism is still active, affecting Quaternary materials (Gutierrez et al., 2019). The coastline also changes in this sector to NW-SE, while further north, up to the Pyrenees, it has a NE-SW orientation, which is the same as that of the primary faults in the Valencia Trough, as in the WVT. This orientation, which is transverse to the main trough, is likely influenced by the Betic front. The offshore Cabo de la Nao fault (23, Fig.1) would be one of the primary faults of this transverse fault system (Maillard and Mauffret, 1999).

We have 10 focal mechanisms in this tectonic zone. Most of them indicate normal faulting, but there are also strike-slip focal mechanisms. The combined tensors present minimum rotation angles of 74°, showing a permutation between the B and P axes. The combined tensor has an *fclvd* value of -0.25 and a prolate tensor shape with $k = 2.56$, showing the predominance of the N069°E oriented extension. The stress tensor obtained from the inversion (Fig. 7 SVT) indicates a normal faulting stress regime, with σ_3 at N058°E, which can activate the transverse fault system of the southernmost part of the Valencia Trough, located in the foreland of the Betic orogen. The stress tensor solution is very similar to those of IC, WVT, and EPCE.

5.12 AL Algarve

The southwestern corner of the Iberian Massif, in the Portuguese Algarve, also comprises a series of Mesozoic and Cenozoic materials, known as the Algarve Basin, which was inverted during the Cenozoic due to N-S to NW-SE shortening. The NW-SE shortening developed later, from the Miocene to the present (Terrinha, 1998; Ramos et al., 2015) and activated E-W to NE-SW striking thrust faults. Still in this zone but north of the basin, there are significant strike-slip faults, such as the southernmost part of the Messejana-Plasencia Fault (18, Fig. 1) (NE-SW, left lateral) and the São Marcos - Quarteira Fault (24, Fig.1) (NW-SE, right lateral). According to GPS data, the southern block of this fault exhibits notable movement to the northwest relative to the northern block (Cabral et al., 2017). It displays apparent activity during the Quaternary (Cabral et al., 2019). Offshore, the most relevant tectonic structure is the Portimão Bank, bounded by E-W thrusts and co-located with a Cretaceous magmatic intrusion (Terrinha et al., 2009; Vázquez et al., 2015; Neres et al, 2018b). Throughout the Algarve basin, there is active salt tectonics (Matías et al., 2011).

We can group the focal mechanisms in this zone into pure and reverse strike-slip faulting. Although there is some scatter in the orientation of the T-axes, the P-axes are very consistent, with the combined strain tensor having an orientation of the maximum shortening axis at N143°E. The combined moment tensor, however, is far from a double couple, showing a very high *fclvd* of 0.4 and an oblate tensor shape, with a *k* value of 0.132. This *k*-value is the lowest value of all obtained solutions, showing the dominance of the shortening deformation tensor.

The inversion of the 11 mechanisms indicates a thrust-faulting stress regime (Fig. 7 AL) with σ_1 at N140°E, which activates NE-SW striking thrust faults and left-lateral N-S and NW-SE striking right-lateral strike-slip faults. The solution is very similar to that obtained for the WCS, showing that this type of stress predominates throughout the SW corner of Iberia, to the west of the Betic front. This observation, together with the absence of thrust faulting stresses in the Iberian Betic foreland, indicates that one of the effects of the emplacement of the Alboran Domain to the west was the mechanical decoupling between Iberia and Africa (de Vicente and Vegas, 2009).

5.13 EB Eastern Betics

The easternmost part of the Betics shows a significant level of seismic activity. This area was affected by extensional tectonics during the opening of the Algero-Balearic Basin throughout the Miocene, the most significant extensional episode occurring in the Serravallian-Tortonian (Comas et al., 1999). However, it may have maintained a specific transcurrent character (Montenat and Ott d'Estevou, 1999). Since the Late Miocene, the dominant tectonics in the region has been characterised by shortening, resulting in the tectonic inversion of the Miocene basins (Sanz de Galdeano, 1990; Martínez-Díaz, 1998). The active continental indentation of the Águilas Arc to the northwest is related to this shortening, which is linked to the collision of Africa and Eurasia, in which the arc forms part of the African crust (Ercilla et al., 2022; Tendero, 2022). The overthrusting arc is bounded to the east by the right-lateral strike-slip Mazarrón Fault (25, Fig. 1) and to the west by the left-lateral strike-slip Palomares Fault (26, Fig.1). The latter extends south-westwards on the Carboneras Fault (27, Fig. 1) to the offshore

Alborán Sea. The indentation implies a progressive tilting towards the SE of the whole arc (Ercilla et al., 2022; Tendero-Salmerón, 2022). In the frontal part of the arc, once in the Iberian crust, the deformation is accommodated in a left-lateral NE-SW transpressional corridor, the Eastern Betic Shear Zone (EBSZ), specifically the Alhama de Murcia Fault (28, Fig.1), in continuity with the Trans-Alboran Transpressional Shear Zone (TASZ). In this shear zone that the most active faults of the Iberian Peninsula are found, with deformation rates between 0.5 - 1.5 mm/yr as indicated by palaeoseismological and geodetic methods (Herrero-Barbero et al., 2020; Gomez-Novell et al., 2022; Moreno et al., 2015; Echeverría et al., 2015; Martín-Banda et al., 2016). The simultaneous activity of these two macrostructures implies the presence of a deformation partitioning process (s.s), potentially with a certain degree of mechanical decoupling between the African and Iberian crust.

The focal mechanisms in this tectonic zone are dominantly strike-slip and reverse events, with the most frequent having a specific oblique character. At the same time, some normal faulting events with a strike-slip component are also present. The minimum rotation angle between the strike-slip moment tensor and the extensional moment tensor is about 47º, indicating the predominance of a transcurrent character in the normal mechanisms (see Appendices A and B). The combination of all the mechanisms gives result an oblate-shaped strain tensor, dominated by shortening, with *fclvd* values of 0.21 and a *k* value of 0.46. The P axis has an N172°E orientation, although the P axes of all mechanisms have a large scatter, which is controlled by the location of the events (see Appendices A and B). This variability of the shortening axes may be influenced by the presence of large crustal structures that generate local block rotations (Martínez-Díaz, 2002) or by local deformation distribution patterns in the area (Alonso-Henar et al., 2019).

The inversion of the 47 focal mechanisms (Fig. 7 EB) provides a thrust-to-strike-slip faulting stress regime with σ_1 at N171°E, which can activate NE-SW to ENE-WSW striking thrust faults, as well as right-lateral NW-SE and left-lateral NNE-SSW striking strike-slip faults. There are also three NW-SE striking normal fault mechanisms in the area, which have a common σ_3 (NE). This stress tensor solution explains the simultaneous movement of the Águilas Arch and Alhama de Murcia fault (28, Fig.1).

5.14 WAA Western Alcaraz Arch

This tectonic zone includes the westernmost part of the Alcaraz (or Prebetic) arch and a sector of the Guadix Basin, which has recorded intense seismic activity in recent years. The structural morphology is similar to that of other arcs in the Betics (Águilas) and the Alborán Sea, which are interpreted as resulting from tectonic indentation processes, in this case, incipient (Tendero-Salmerón, 2022). The seismicity is concentrated along two NW-SE to ESE-WNW right-lateral strike-slip faults, the Tiscar and Guadiana Menor (29, Fig. 1) faults (Tendero-Salmerón et al., 2020), which affect Quaternary materials and the Cenozoic sediments of the Cenozoic Guadalquivir Basin. The Torreperogil - Sabiote seismic series, characterized by strike-slip focal mechanisms, also appears to be related to faults possibly rooted in the basement (Pedrera et al., 2013). To the south, the intramountain Guadix Basin (30, Fig.1), with a general NW-SE trend, is filled with Tortonian to Pleistocene sediments (Pla-Pueyo et al. 2009) bounded by NW-SE normal faults (Alfaro et al., 2008; Sanz de Galdeano et al., 2012).

Of the 14 focal mechanisms, two are normal faulting events (in the Guadix Basin) and the rest are strike-slip events (also one in Guadix). The orientation of the T axes in both types of mechanisms is consistent with the minimum rotation angle between strike-slip and normal events being close to 90°. The combined strain tensor has a prolate shape, dominated by the T axis, with an *fclvd* value of -0.23 and a *k* of 2.3. The orientation of the T axis is N052°E, while the P axis has an orientation of N142°E. The stress tensor obtained by inversion (Fig. 7 WAA) indicates a strike-slip stress regime with a normal component, characterized by σ_1 at N153°E. This stress regime activates left lateral N-S and right lateral ESE-WNW strike-slip faults, as well as NW-SE normal faults. The inferred stress tensor is like that obtained by Tendero-Salmerón et al. (2020) from 5 mechanisms in the Tiscar and Guadiana Menor faults (strike-slip stress regime with σ_1 at N143°E).

5.15 Granada Basin

Within the tectonic context of NW-SE convergence between Africa and Eurasia (Iberia), as well as the westward emplacement of the Alboran Domain, accompanied by the rollback of the southern Iberian slab, the presence of NW-SE extensional basins within the orogen appears to be kinematically necessary. The easternmost part of the Betic Orogen is dominated by processes of thrust arc indentation with tectonic transport to the NW (Tendero-Salmerón 2022), while the westernmost arc formed by the Betic and Rif arcs surrounding the Strait of Gibraltar is located to the W. This kinematic pattern is supported by the presence of a NW-SE extensional basin within the orogen, which is dominated by the presence of NW-SE normal faults related to radial extension (Reicherter and Peters, 2005). This kinematics is confirmed by GPS data (Cannavò and Palano, 2016; Neres et al., 2018a, 2019). The boundary between these two zones within the Betic Orogen is marked by extensional basins aligned and bounded by NW-SE normal faults, such as the Guadix fault in WAA, and by the Granada Basin. The age of deformation in the Granada basin ranges from Late Miocene to present, defining a seismicity corridor approximately 300 km wide (Galindo-Zaldivar et al., 1999). The most prominent faults here are the Granada (31, Fig. 1), Sierra Elvira-Dílar (31, Fig.1), and Padul-Dúrcal (32, Fig.1) faults (Sanz de Galdeano et al., 2012).

The focal mechanisms in the Granada Basin are extensional and cluster into two families, whose T-axis orientations form an angle of 30-40° with each other. The combined moment tensor is of oblate type, dominated by vertical shortening and with *fclvd* values of 0.08 and *k* of 0.768. The T axis has an orientation of N048°E, and the B axis of N139°E, which is consistent with the dominant stress regimes in the surrounding zones.

The seismic sequence that occurred in 2021 enabled the determination of the stress tensor from 5 focal mechanisms of normal faulting stress regime (R=0.28), with σ_3 at N049°E (Madarieta-Txurruka et al., 2022). In our stress inversion (Fig. 7 GB), we utilized 16 focal mechanisms that yield a highly consistent triaxial normal faulting stress regime with σ_3 striking at N033°E. Therefore, this stress orientation is congruent with that obtained from the E (WAA and EB), facilitating the emplacement of WB to the W. The most recent calculated paleostress, σ_1 subvertical, σ_3 subhorizontal trending NE-SW, activates normal faults, but coevally; σ_1 subhorizontal NW directed, σ_3 NE–SW subhorizontal with a strike-slip faulting regime that has been

645 interpreted as periodic strike-slip and normal faulting events due to a permutation of the principal stress axes (Reicherter and Peters, 2005).

5.16 NA Northern Alboran

The offshore deformation of the N margin of the Alborán Sea has been explained because of the ongoing slab rollback in the Alborán Domain, in the Gibraltar Arc (Betics-Rif), and of the indentation tectonics that predominates to the east and south,
650 giving rise to a complex faulting pattern (Galindo-Zaldivar et al., 2022). On the other hand, in the easternmost part of this zone, the most important tectonic structure is the Carboneras Fault (27, Fig. 1), with the same kinematics as the the Palomares Fault (26, Fig.1) (EB). This structure has an NE-SW strike, extends offshore, and has been active since the Late Miocene until the present. This fault shows a left-lateral strike-slip movement that occurs at a rate of 1.3 mm/yr (Moreno et al., 2015) and an offset of more than 15 km (Gràcia et al., 2006; Rutter et al., 2012), four palaeoseismic events have been identified (Masana et
655 al., 2018). Among the 42 focal mechanisms analysed, we find reverse and normal solutions but mainly strike-slip ones. Except for three normal faulting focal mechanisms indicating N-S extension, the others show a T (or B) axis towards NE-SW. The shortening axes in the focal mechanisms are very consistent, with orientations between N130°E and N180°E. The minimum rotation angles between the normal faulting mechanisms and the strike-slip and thrust mechanisms are high, ranging from 90°-100°; in contrast, the minimum rotation angle between the reverse and strike-slip mechanisms is approximately 50°, indicating
660 a strong strike-slip component in the thrust earthquakes (see Appendices A and B). The combined moment tensor is a slightly prolate strike-slip deformation tensor, with a k value of 1.63 and an *fclvd* of -0.14. The extensional stress axis, which would be dominant in the deformation of the zone, has an N065°E trend, while the shortening axis has an N154°E trend. The stress inversion result is similar to those of WAA and EB. The obtained solution (Fig. 7 NA) does not seem to reflect the structural complexity indicated by the field and GPS data (Galindo-Zaldivar et al., 2022). The solution exhibits a strike-slip stress regime
665 with a normal component, characterized by σ_1 in N149°E and σ_3 in N064°E. Therefore, in this zone, the indentation process would predominate over the rollback process.
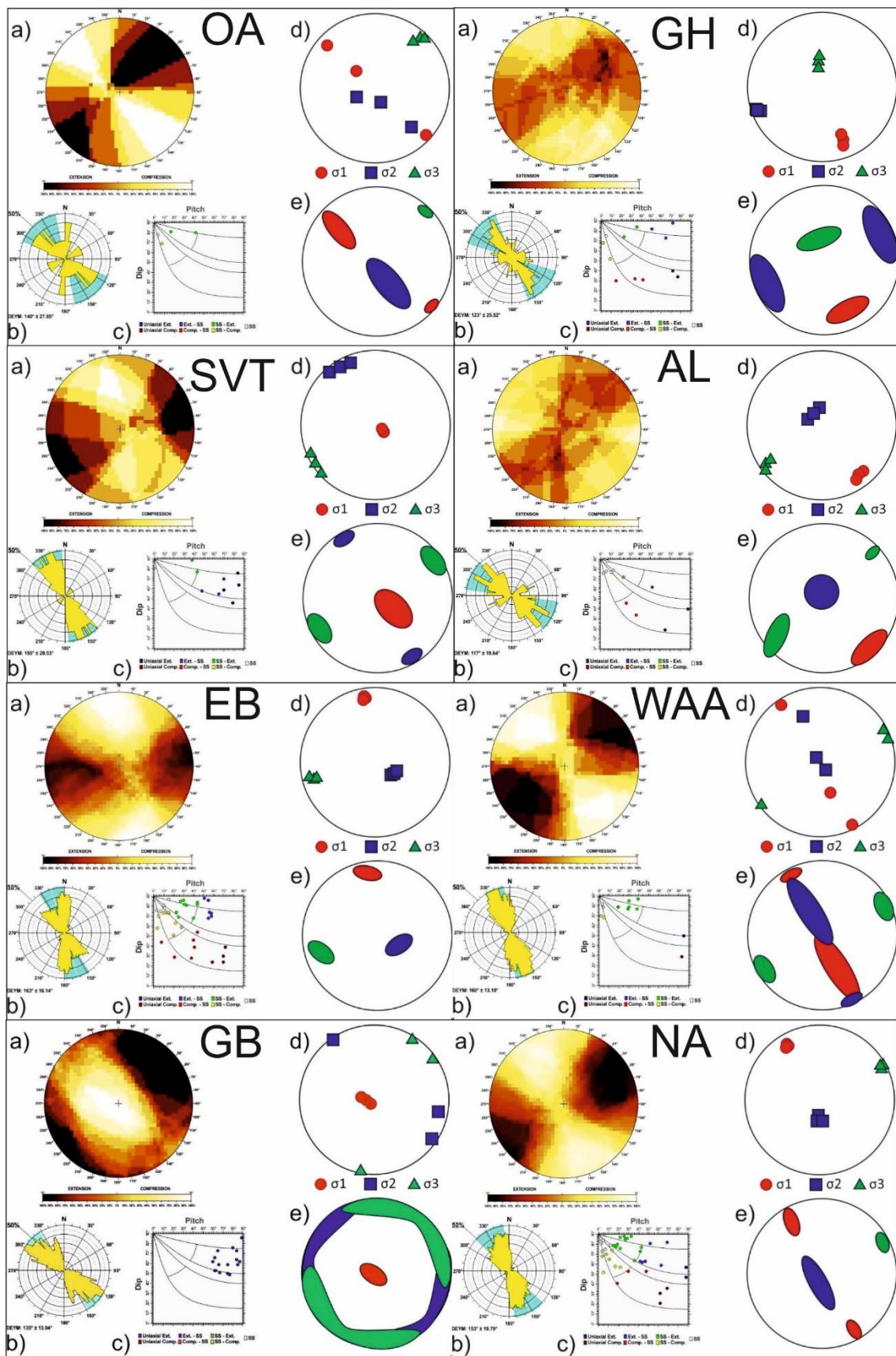
5.17 AR Alboran Ridge

The most prominent structures in the Alborán Sea, in the central part of the Alborán Domain, are the Alborán Ridge (33, Fig.1), a crustal pop-up with the main tectonic transport to the NW and outcropping Neogene volcanic materials, the left-lateral Al Idrissi Fault (34, Fig.1), and the right-lateral Yusuf Fault (35, Fig.1). The three structures draw an indentor with similar kinematics to those of Águilas and Cazorla (in EB and WAA) (e.g., Tendero-Salmerón, 2022). Since the Late Miocene, magmatic intrusions in the Alborán Ridge seem to have acted as a backstop that favoured its uplift relative to the indentation (Tendero-Salmerón, 2022). The continental crust to the S of the structures above appears to belong to the African Plate, so these faults are considered to constitute the active plate boundary between Africa and Eurasia (Iberia), with the Yusuf Fault (35, Fig. 1) extending to the Tell Mountains orogen in Algeria (Martínez-García. 2012; Gómez de la Peña, 2017). The seismic crisis of 2016, which included an M_w 6.4 earthquake located at the southern limit of the Al Idrissi fault system (34, Fig.1), enabled defining its trace by connecting it with the Bokkoya and Trougout Faults, which enter the African onshore and connect with the Nekor Fault (36, Fig.1). It is therefore a very recent plate boundary (Gràcia et al., 2019). The seismic sequence indicates the presence of restraining steps along the strike-slip fault (Stich et al., 2020).

The focal mechanisms in this tectonic zone include pure reverse faulting, oblique faulting, with mainly normal component, and normal faulting with strike-slip component. The minimum rotation angles between the three fault types are high, showing the activation of different structures in response to a consistent strain tensor. The orientation of the T axes is very congruent in all mechanisms, with directions between N050°E and N080°E. The shortening axes show somewhat more variability. The combined moment tensor has an oblate shape, with k 0.519 and fclvd 0.19, and is dominated by shortening with an N157°E orientation. The mean T strain axis is N069°E.

The inversion of the 63 focal mechanisms (Fig. 8 AR) indicates a transpressive strike-slip faulting stress regime, with σ_1 at N161°E, which activates mainly N-S to NNE-SSW left-lateral faults, NW-SW right-lateral strike-slip faults, and E-W to ENE-WSW thrust faults. There are also five normal faulting mechanisms with nodal planes sub-parallel to the inferred σ_1 orientation, indicating the presence of secondary normal faulting steps along faults in the principal direction. The stress solution is intermediate to that of the Águilas (EB) and Alcaraz (WAA) indentors.

5.18 ALH Al Hoceima

The S sector of the Alboran Domain, on the N coast of Morocco, shows significant seismic activity (2004 Mw 6.4 and 1994 Mw 5.9 earthquakes) in the Al Hoceima area (37, Fig.1) with ruptures up to 20 km, which allowed us to infer an associated strike-slip stress regime (R=0.5) with σ_1 at N161°E and σ_3 at N071°E (van der Woerd et al., 2014). However, the Trougout

700 (N171°E) and Bokkoya (N030°E) faults, which continue offshore in AR, together with the Bousekkour-Aghbal (N020°E) fault, bound the Pliocene-Quaternary Nekor basin and define a transtensional area between the Nekor (36, Fig.1) and Al-Idrissi (34, Fig.1) faults (d'Acremont, 2014). Backstripping analyses of the sediments of Al Hoceima Bay during the last 280 Kyr indicate a westward migration of deformation with vertical throw rates of 0.47 mm/year because of the interaction between the northwesternward movement of the Alboran indentor and the south-westward displacement of the Rif (Tendero-Salmerón,

705 2021). Further to the E, the NE-SW Kert and Nador faults (38, Fig.1) appear to have a normal component (Ammar et al., 2007), although the considered focal mechanisms are mainly strike-slip faults like those of Al Hoceima. Therefore, we grouped them into a single population.

The focal mechanisms indicate mainly strike-slip and normal faulting, with a significant population of oblique faults with both components. Reverse-type events with strike-slip components are also present. All focal mechanisms exhibit highly consistent

710 axes of maximum shortening and horizontal extension, with minimal variability. The combined moment tensor indicates a strike-slip deformation with an extension component close to a double couple, with an *fclvd* value of -0.08 and a *k* value of 1.3. The P axis of the combined moment tensor has an orientation N143°E and the T axis N060°E.

As there are more normal fault-type focal mechanisms in this population than in AR, the stress tensor shows a strike-slip faulting solution (Fig. 8 ALH) with a normal component, with σ_1 at N152°E and σ_3 at N064°E. Therefore, the tectonics in this

715 zone is presently transtensional.

5.19 WTA-ETA Western-Eastern Tell Atlas

The Algerian Tell Atlas is the most seismically active area in the western Mediterranean, including, among others, the 1980 El Asnam earthquake, Mw 7.3, which occurred on a 36 km long thrust linked to a NE-SW fault propagation anticline (39, Fig. 1). The focal mechanism of this earthquake indicated the presence of a NW-dipping thrust plane (Meghraoui et al., 1986). In

720 general, this is in good agreement with the tectonics of the range, characterized by dipping faults related to fault adaptation-propagation anticlines. These main neotectonic structures correspond to E-W striking to NE-SW striking thrusts that cut Quaternary rocks. The main intramountain basins are the Cheliff, Mitidja, Soummam, Hodna, and Constantine basins (Maouche et al., 2019 and references therein). The coast shows evidence of folding and uplift, with marine terraces uplifted during the Pleistocene and Holocene (Maouche et al., 2011).

725 In the WTA, the most frequent focal mechanisms are reverse, coexisting with strike-slip and some normal faulting, all of them kinematically compatible with NW-SE horizontal shortening axes. The combined moment tensor is oblate reverse, with $k = 0.328$ and *fclvd* 0.28, showing the predominance of horizontal shortening. The P axis has an orientation N143°E and the B axis N050°E. Further east, the population of focal mechanisms is similar, primarily characterized by thrusting events. The combined moment tensor is therefore of a shortening type and oblate, although it is closer to the double couple, with $k = 0.767$ and *fclvd*

730 = 0.08. The P axis is oriented N155°E and the B axis N069°E; therefore, the shortening is more northerly in this area than it is further to the west.

Because the inferred moment tensor vectors and shortening directions are not coaxial, it has recently been suggested that, from the Alboran domain to the E, transpressional tectonics predominates, activating E-W striking right-lateral strike-slip faults and NE-SW striking thrusts (Meghraoui and Pondrelli, 2012). Stress inversions based on earthquake focal mechanisms indicate that the deformation is accommodated by E-W striking reverse-strike-slip faults in the Eastern Tell. In contrast, the Western Tell is dominated by strike-slip faults (Soumaya et al., 2018). The stress inversions obtained in this study (Fig. 8 WTA, ETA) show a very similar σ_1 orientation for the eastern and western parts of the Tell-Atlas: N149°E (west) and N145°E (east), with a thrust-faulting stress regime to the east, and with a larger strike-slip component in the west, contrary to Soumaya et al. (2018). Both solutions activate NE-SW striking thrust faults, NW-SE right-lateral and N-S left-lateral strike-slip faults.

5.20 GC Gulf of Cádiz

The Gulf of Cadiz appears to be dominated by the south-westward movement of the Betic-Rif orogen, which has built up a sediment stack that is up to 12 km thick in an accretionary prism characterised by W-verging thrust-spreading anticlines (40, Fig.1). The prism is related to the subduction of the S margin of Iberia below the Rif-Betic-Alboran microplate. Subduction appears to have slowed down significantly during the last 5 Myr, although deformation in the accretionary prism still affects recent sediments (Gutscher et al., 2012). Thermo-mechanical modelling indicates that although the subduction process has ceased, deep slab motion still induces a mantle flow that produces a W-directed basal drag of the Alboran domain lithosphere (Gea et al., 2023; Neres et al., 2019). Some of the selected focal mechanisms are located in the S margin of the Algarve Basin, S of the Portimão Bank (AL) (Ramos et al., 2015; Neres et al, 2018b), providing a relatively homogeneous population.

The focal mechanisms in this tectonic zone are mainly strike-slip, although normal and reverse faulting events are also present. The combination of the mechanisms results in a strike-slip seismic moment tensor but with an oblate shape, characterized by $k = 0.417$ and $fclvd = 0.24$. The P-axis has an orientation of N161°E, and the T-axis is N066°E. The inversion provides a strike-slip stress regime (Fig. 8 GC) with σ_1 at N150°E, with less thrusting component than that obtained for AL, GH, and WCS. Therefore, it does not seem that there is significant seismicity related to thrusting with tectonic transport to the W, but rather to the SE or NW.

5.21 WB Western Betics

The emplacement of the Rif-Betic-Alboran Domain to the west during the Early Middle Miocene, together with the NW-SE oblique convergence between Eurasia and Africa, has influenced the structuring of the Betic Orogen. However, since the Late Miocene, it is the latter process that seems to have dominated (Ruiz-Constán et al., 2011). The NW Betic Mountain front is the seismically most active sector. Although seismogenic structures do not outcrop at the surface, moderate-depth earthquakes indicate the presence of NE-SW thrusts with some related tear faults (41, Fig.1) (Ruiz-Constan 2009).

In our analysis, we used only earthquakes at crustal depths. The population of focal mechanisms is dominated by strike-slip faulting, with several of these mechanisms exhibiting an oblique orientation and a reverse component. However, a significant number of thrust faulting events are also observed. The orientations of the axes of maximum shortening and horizontal extension are scattered, characterised by two families: a major one with a shortening direction N120-150°E and a minor one with a N-S shortening direction. The combination of the focal mechanisms gives rise to a shortening-strike-slip seismic moment tensor with an oblate shape, exhibiting values of k 0.376 and $fclvd$ 0.26. The shortening axis P has an orientation of N143°E and the B axis N046°E, although with a 28° plunge.

The total population of 32 mechanisms provides a well-constrained stress inversion result (Fig. 8 WB). The inferred stress tensor indicates a strike-slip stress regime with σ_1 at N139°E, which activates NE-SW striking thrusts and strike-slip faults. These faults exhibit right-lateral displacement when striking east-northeast to west-southwest (ENE-WSW) and left-lateral displacement when striking north-northeast to south-southwest (NNE-SSW).

Stress inversions in this area are considered in terms of the hypocentral depth, as the deepest stresses/deformations could be related to the Iberian slab under the Alboran Domain. Ruiz-Constán et al. (2012) obtained σ_1 trends for shallow seismicity at N166°E (4 mechanisms) and N018°E (4 mechanisms). For the intermediate earthquakes, we have received a σ_1 trend between N113°E and N126°E, encompassing 29 mechanisms. The σ_1 trend is located more towards the ESE-WSW concerning the surrounding areas, likely influenced by ongoing motion of the deeper portion of the slab which induces a mantle flow that causes basal drag of the lithospeher (Gea et al., 2023), which is more evident at depth (Ruiz-Constán et al., 2012). To test this effect, we inverted the seven focal mechanisms corresponding to earthquakes with hypocentral depths of more than 20 km in this zone (WBD), obtaining a σ_1 of N114°E trend, more E-W than the shallow ones (Fig. 8 WB>20). Therefore, our results confirm that the slab effect is more pronounced at greater depths, being negligible in shallow earthquakes.

5.22 BA Betics Antequera

Between the Granada Basin (GB) and the thrusts at the NW edge of the Betics (WB), there is a 70 km long right-lateral transpressional brittle-ductile shear zone. The Torcal Shear Zone (42, Fig.1) has been active from the Late Miocene until the Quaternary (Barcos et al., 2015). In 1989, a seismic series (117 earthquakes) was reported between Loja and Palenciana, which indicated that the fault zone had a strike of N070-080°E (Posadas et al., 1993). From the focal mechanisms obtained for this crisis, a strike-slip stress regime with σ_1 at N135°E was previously determined by Vadillo (1999).

The focal mechanisms in this tectonic zone are of strike-slip type with an extensional component, as observed in 5 events. The combination of these events results in a strain tensor very close to a double couple, with a value of $k = 1.16$ and $fclvd =- 0.04$. The orientation of the P axis is N125°E and the T axis N028°E. The inversion of the five focal mechanisms (Fig. 8 BA) reveals a strike-slip stress regime with a normal component, characterized by σ_1 at N105°E, which activates ESE-WNW right-lateral strike-slip-normal (transtensional) faults. This σ_1 orientation is more likely to be that of the WB than that of the other adjacent areas and could indicate a greater effect of the rollback process of the Iberian slab, from here to the west. The extension-normal

faulting in the Granada Basin (GB) may therefore be explained by the greater effect of the westward remanent movement of the Alboran Domain, which is partially decoupled from the indentation zone of the Betic arcs further to the east.
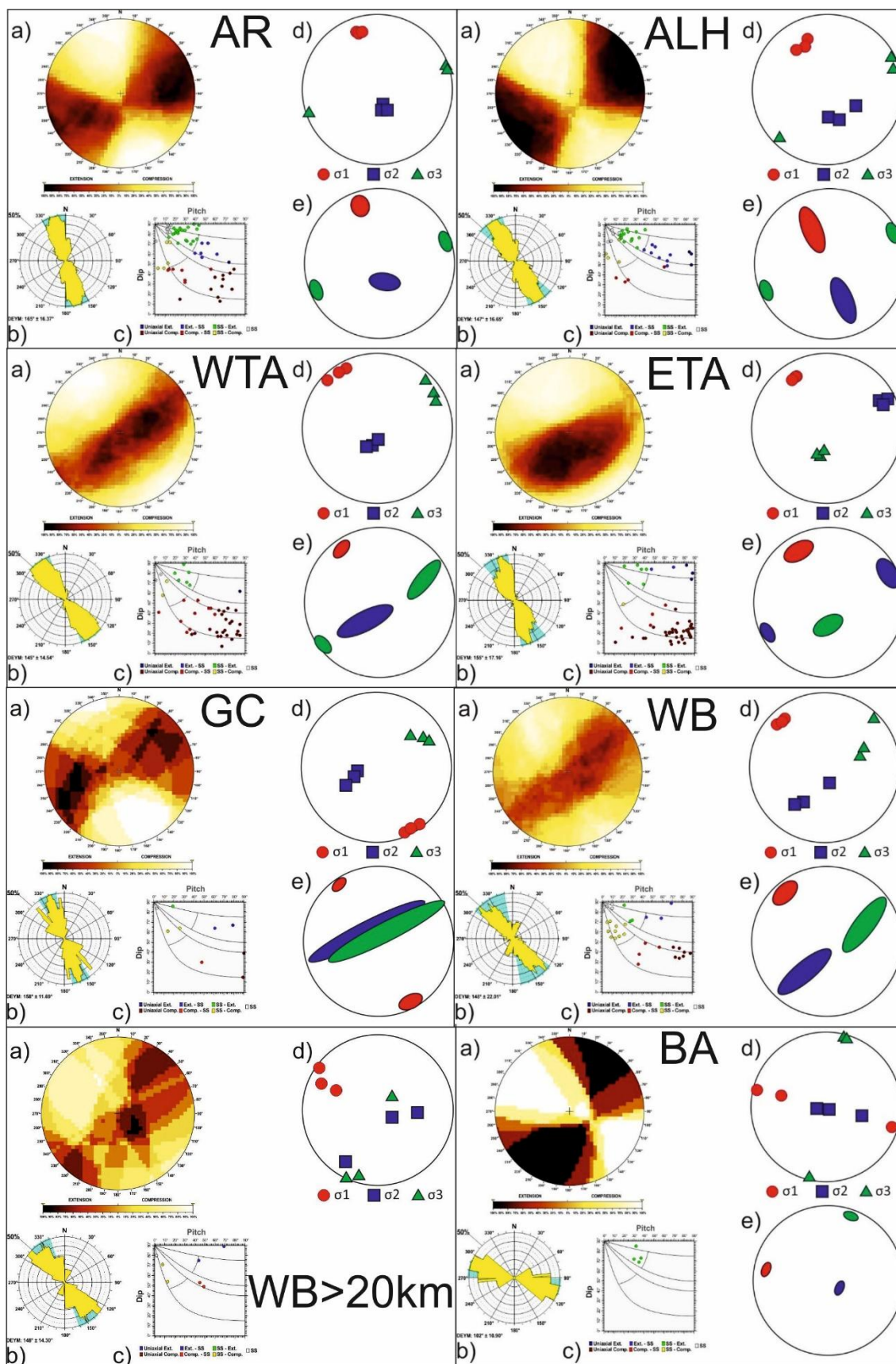
Figure 8: Results of the stress-strain analyses for different zones: a) Right Dihedra solution. b) Rose diagram of the Deys obtained from the Slip model. C) Pitch/Dip plot for the neo-formed nodal planes obtained from the Slip Model. d) Stress Inversion Results. e) Variability of the three principal stress axes of the stress inversion. AR Alboran Ridge; ALH Al Hoceima; WTA Western Tell Atlas; ETA Eastern Tell Atlas; GC Gulf of Cádiz; WB Western Betics (WB depth > 20 km); BA Betics Antequera.

6 Stress map of Iberia

The new compilation of earthquake focal mechanisms and the results from the stress inversions can be used to update the stress map of Iberia using the quality ranking scheme of the World Stress Map (WSM) project. The WSM is the global resource for stress information on the present-day stress field of the Earth's crust (Heidbach, 2016; Heidbach et al., 2018; Zoback, 1992) and compiles the orientation of maximum horizontal stress (S_{Hmax}) from a wide range of stress indicators such as earthquake focal mechanism solutions (FMS), drilling-induced tensile fractures (DIF), borehole breakouts (BO), hydraulic fracturing tests (HF), overcoring (OC) as well as geologic data from seismogenic fault-slip analysis (GFI, GFS) and volcanic vent alignments (GVA) (Amadei and Stephansson, 1997; Ljunggren et al., 2003; Sperner et al., 2003). The stress information is compiled in a standardized data format and quality-ranked to make data from very different methods comparable (Heidbach et al., 2010). The various stress indicators reflect the in-situ stress of different rock volumes ranging from 10^3 to 10^9 m³. Furthermore, except for the earthquake focal mechanisms and a few very deep boreholes, all stress indicators sample only the stress patterns within the upper 6 km of the Earth's crust, with deep boreholes as a major contributor. The most common visualization of stress data is through stress maps, where data from depths between 0 and 40 km is integrated (Heidbach et al., 2004; Heidbach and Höhne, 2008), assuming that the S_{Hmax} orientation does not change significantly with depth. This assumption was initially tested qualitatively at the beginning of the WSM project (Zoback, 1992) and subsequently confirmed with significantly higher data density on both global (Heidbach et al., 2018) and regional scales (Pierdominici and Heidbach, 2012; Rajabi et al., 2017a).

For the new stress map of Iberia, we re-evaluate all data records from geological data (n=141), borehole breakouts (n=129), overcoring (n=16), and hydraulic fracturing (n=5) and combine these with the S_{Hmax} orientations derived from the new compilation of earthquake focal mechanisms (FMS) and stress inversion results (FMF) obtained in this study. Given that the majority of the WSM data records have not been revisited for almost 30 years, our re-evaluation resulted in a reduction of data records due to double entries and typos (from n=295 to n=271) and down-ranking in quality due to a stricter data assessment. Therefore, the number of stress data records with A-C quality decreased from n=172 to n=132. A-C quality means that the σ_{Hmax} orientation is reliable within ± 25°, D quality data records are only reliable within ± 40° and thus should be used with caution (Rajabi et al., 2024; Tingay et al., 2006; Tingay et al., 2005). E-quality data are of poor quality, and X-quality data have insufficient or missing information to assign a quality. The latter is a new assignment class that is already used in the new WSM quality ranking for stress magnitude data records (Morawietz et al., 2020) and will also be used in the next WSM database release for stress orientation data records (Table 6).

Type/Quality	A	B	C	D	E	X	Total

FMS	0	0	456	0	86	0	**542**
FMF	5	15	0	0	11	18	**49**
FMA	0	0	0	24	0	1	**25**
BO	8	30	36	38	5	5	**122**
HF	1	0	1	1	0	0	**3**
OC	0	0	0	2	0	14	**16**
GFS	0	0	0	12	0	0	**12**
GFI	0	8	48	10	22	30	**118**
Total	**14**	**53**	**541**	**53**	**148**	**68**	**887**

Table 6: Overview of data quality and stress indicators in the new compilation of stress in Iberia shown in Fig. 10. Note that most of the downranking of data records from borehole breakouts (BO), hydraulic fracturing (HF), overcoring (OC) and geological indicator (GFI, GFS) are due to missing information in the papers and reports where data are presented. The other abbreviations are FMS for single focal mechanisms, FMF for stress inversion from population of focal mechanisms, and FMA for composite focal mechanisms.

The resulting stress map shows that, at first order, the data records from boreholes agree with earthquake focal mechanisms data from greater depths. An exception is the borehole data in the Aquitaine Basin north of the Pyrenees, where some σ_{Hmax}

835   orientations from borehole breakouts confirm the prevailing WNW-ESE strike, but others show different orientations. These data results from a comprehensive study of 55 wells by Bell et al. (1992). The authors discuss in detail the somewhat controversial result of varying S_{Hmax} orientations on local scales, which has not been observed in other foreland basins (Reinecker et al., 2010; Reiter et al., 2014). However, for the remaining areas, there is an overall agreement between the S_{Hmax} orientations inferred from borehole data and those from earthquake focal mechanisms results.

840   To analyse the prevailing S_{Hmax} orientation pattern, we estimate the mean S_{Hmax} orientation on a 0.5° grid using the tool stress2grid from Ziegler and Heidbach (2019) with a 150 km search radius. For the estimation, a minimum of five data records is required within the search radius. Weights are applied considering data quality and distance to the grid point. The distance weight is cut off when the data record is within 15 km of the grid point to avoid an overrepresentation of data records close to the grid point. Furthermore, we distinguish the resulting mean S_{Hmax} orientations according to their standard deviation SD.

845   Dark grey bars in Fig. 9 denote mean S_{Hmax} orientations with SD ≤ 25°, light grey ones with SD > 25°. The resulting mean S_{Hmax} orientation in Fig. 9 shows that, in particular, in the center of Iberia, the stress pattern does not show a clear trend, in contrast to almost all the other regions, except the Pyrenees. This is reflected in the rotations of the mean S_{Hmax} orientation and the significantly higher standard deviation (SD) values in the center of Spain. The changes of the mean S_{Hmax} orientation on short scales could be either due to low data density, which allows for a single outlier or local deviation from the stress pattern

850   to have a high impact on the mean trend, or to the stress pattern being indeed quite variable, for example, due to low anisotropy of the horizontal stresses, which results in less stable horizontal stress orientations (Heidbach et al., 2007; Lundstern and Zoback, 2020; Rajabi et al., 2017b).
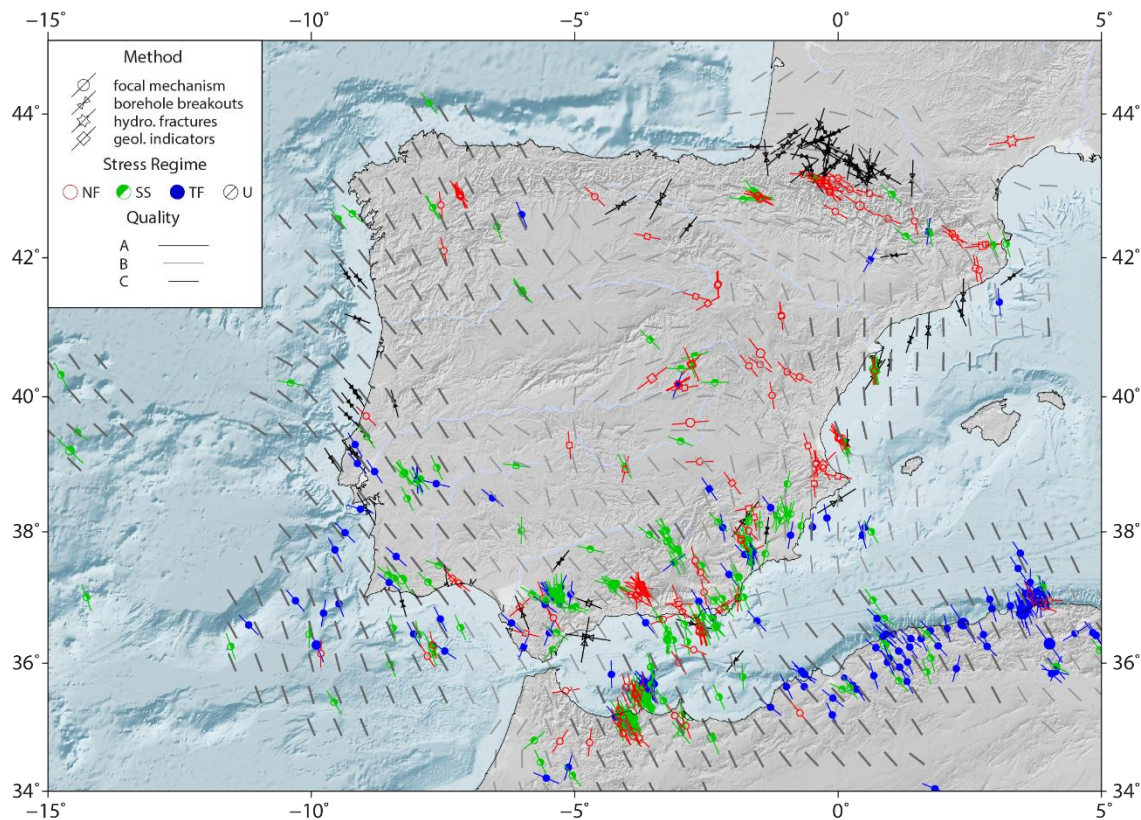
Figure 9: Stress map of Iberia based on A-C quality data records from this study and from re-evaluated data of the WSM database release 2016 (*Heidbach et al.*, 2016). Plotted is the orientation of maximum horizontal stress S_{Hmax} for depths between 0-40 km. See the inset legend for details on data types, stress regime (NF= normal faulting, SS= strike-slip, TF= thrust faulting, U= unknown). Data symbols indicate the type of stress indicator and line length are proportional to data quality. Grey bars on a 0.5° grid show the mean S_{Hmax} orientation that is estimated with a search radius of 150 km using weights for data quality and distance to the grid point. Dark grey bars on the grid show mean σ_{Hmax} orientations with a standard deviation ≤ 25°, light grey bars with standard deviation > 25°. Topography and bathymetry is taken from SRTM15+ (Tozer et al., 2019)

7 Discussion

Our analysis focuses on the Iberian Peninsula, excluding the Gloria Fault, which lies between the Terceira Ridge in the Azores Islands and the Gorringe Bank. Along the Gloria Fault, tectonic stresses responsible for seismicity are primarily associated with strike-slip faulting, with localized thrust components at restraining bends to the east (e.g., de Vicente et al., 2008).

As illustrated in Fig. 10a, the combined focal mechanism tensors exhibit distinct characteristics depending on their tectonic setting. Thus, in the plate boundary zone, the tensors typically reflect of reverse or reverse strike-slip faults with positive *fclvd* values. In contrast, the tensors from the Pyrenees and the central-eastern Iberian Peninsula display normal or normal-directional focal mechanisms, characterised by negative *fclvd* values. An exception is observed in the Granada Basin, where the combined tensor indicates a nearly pure normal faulting regime.

When analysing the combined moment tensor by rupture type, the reverse component (Fig. 10 b) reveals a predominant NW-SE shortening orientation across the area, with nodal planes striking approximately N040°E to N070°E. This general northeast to east-northeast orientation is consistently observed in all combined plate boundary tensors from northern Algeria to the Gulf of Cádiz. An exception is found at the easternmost tip of the Betic Cordillera (EB), where the nodal planes exhibit a more E–W orientation, indicative of N–S shortening. These fault orientations are characteristic of the northern sector of the Aguilas Arch and the Alhama fault system. In contrast, reverse faulting in the northern Iberian Peninsula contributes significantly less to the overall seismic moment release. In this area, the tensors are predominantly oblique, with P-axes aligned with the regional shortening directions—more clearly expressed in the combined strike-slip faulting tensors. The combined strike-slip tensors (Fig. 10c) present nodal planes oriented from N000°E to N050°E for the left-lateral kinematics, which is compatible with the NW-SE shortening orientation described above. All the strike-slip tensors share these characteristics, except the tensor from the Western Pyrenees (WP) and Central Basins (CB), which display right-lateral kinematics along NE–SW-striking planes. These two cases are also distinguished by E-W shortening axis orientations and prolate tensor shapes (k values > 1, $fclvd$ < 0), having the highest k values alongside the tensor from the northwest of the Iberian Peninsula (NWG). While strike-slip tensors are dominant throughout the peninsula (Fig. 10e), they are particularly prevalent within the Alboran domains.

The combined normal faulting tensors can be grouped into two distinct categories. The first includes tensors with extension axes oriented E–W to NE–SW, while the second comprises those with N–S-oriented extension axes. The latter are observed in the central and western Pyrenees (CP, WP), as well as in the Central Basins (CB). Across the rest of the Iberian Peninsula, normal faulting tensors present nodal planes that are approximately parallel to the axes of maximum horizontal shortening. The normal tensors are particularly prominent along a band that connects the Al Hoceima (ALH) area in North Africa to the Central Pyrenees (CP), passing through the Iberian chain (IC) (Figs. 10d and 11b). Also, in the northwest of the Iberian Peninsula (NWG), normal faulting mechanisms plays a dominant role in the combined tensor (Fig. 12 b).

When the combined tensors are projected onto the classification diagram (Fig. 10e), most are located within the fields corresponding to pure rupture types, with a predominance of strike-slip mechanisms—often accompanied by compressional or extensional components. When the tensors are further categorized by rupture type for each zone (Fig. 10f), pure mechanisms remain dominant. This suggests that the coexistence of different rupture styles arises from permutations of principal stress axes that are mechanically compatible, thereby reflecting a regime of distributed deformation. The orientations of the principal axes for each zone are shown in Fig. 11a. NW-SE shortening is predominant in North Africa, the Alboran Sea, and the western half of the Iberian Peninsula. In contrast, in the eastern part, the shortening trends tend to be N-S, except in the areas where extensional regimes dominate (Fig. 11 b), i.e., in the Pyrenees and the Central Basins, where extension is oriented N–S, implying maximum horizontal shortening in the E–W direction.

For each zone where focal mechanisms have determined across different faulting types, we computed the minimum rotation angle between pairs of tensors (Fig. 11c). Most of the rotation angles fall between 60° and 110°, suggesting the activation of fault system governed by a common strain field, where permutation of principal stress axes, particularly 90° rotations, reflect a coherent tectonic framework. A typical example is the permutation between the shortening axis of reverse faults and the

intermediate axis of normal faults. The results for the WVT zone warrant special mention. It includes focal mechanisms related to the Castor Project seismic crisis, a natural gas submarine storage project (Villaseñor et al., 2020; Cesca et al., 2021). In this case, the rotation angle between the tensors of the different rupture types is minimal indicating a consistent rupture type across all events. These are characterized by oblique focal mechanisms located near the centre of the classification diagram (Fig. 10f).

910 In Fig. 11d, the combined tensors are plotted on a Flinn-type diagram for moment tensors, with the colour showing the k-value. Zones characterized by prolate ellipsoids (k > 1), located above the plane strain diagonal, correspond to areas with a significant normal faulting component, namely Pyrenean zones (EPCE, WP, NWG), the Valencia Trough (SVT) and the Central Basins (CB). These results evidence the relationship of these prolate ellipsoids with extensional and transtensional tectonic settings. Conversely, regions exhibiting oblate ellipsoids are linked to transpressional tectonic settings, particularly along the

915 southwestern margin of the Iberian Peninsula (AL, GH, WB, GC, WCS). This relationship between strain tensor shape and proximity to the plate boundary becomes more evident when plotting the k-value as a function of latitude (Fig. 12). Near the plate boundary the shapes of the strain tensors are predominantly oblate, with $k < 1$; whereas farther north, beyond the Betics, k values increase, indicating a prevalence of prolate strain tensors.
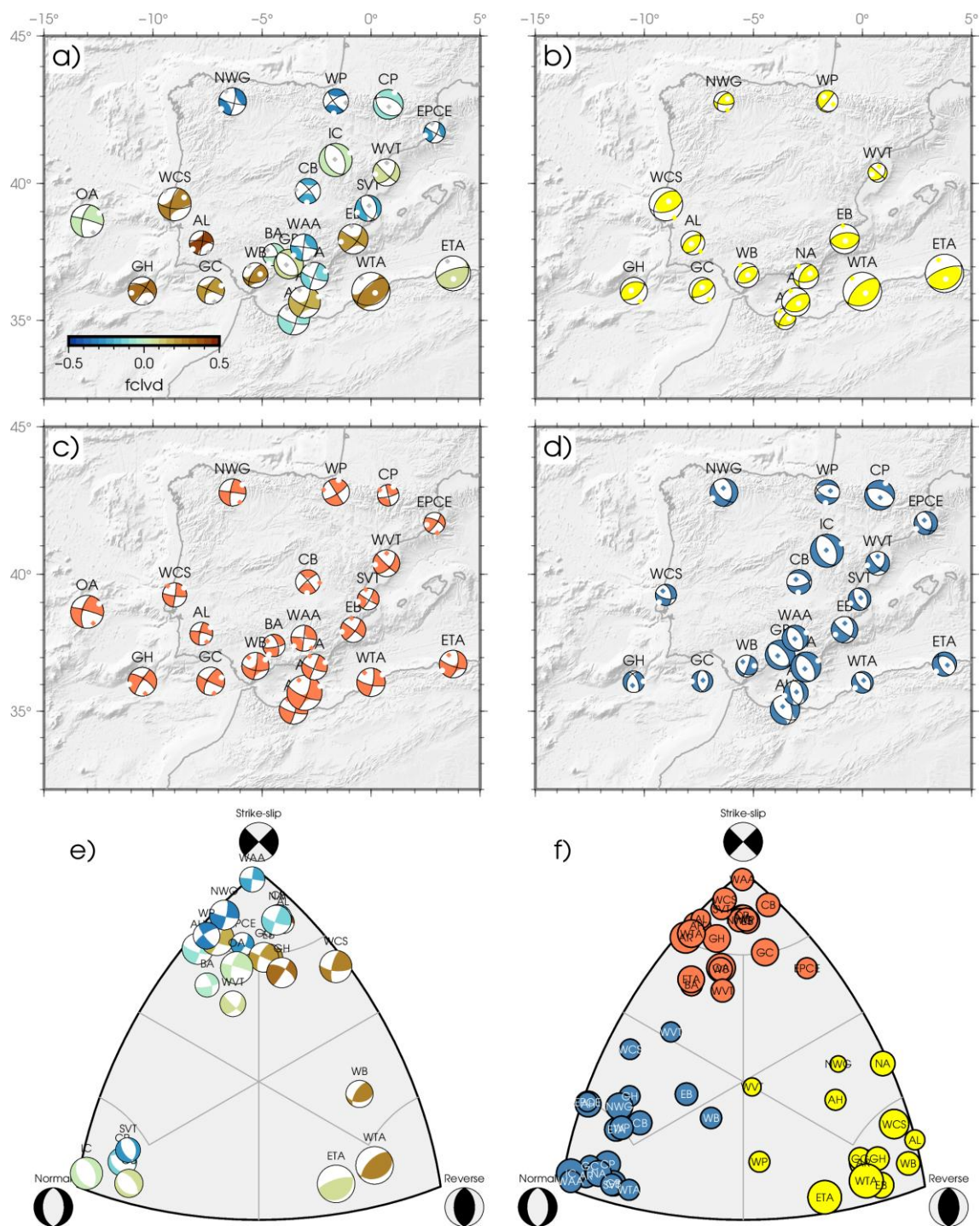
Figure 10: a) Combined strain focal mechanisms for each of the tectonic zones. The colour of the beach ball represents the compensated linear vector dipole factor fclvd. b) Combined focal mechanism for reverse faulting earthquakes in each zone. c) Combined focal mechanism for strike-slip earthquakes in each zone. d) Combined focal mechanism for normal earthquakes in each

zone. e) Focal mechanism classification diagram for the combined mechanisms shown in a). f) Focal mechanism classification diagram for the different rupture type combined mechanisms shown in b), c) and d).

925
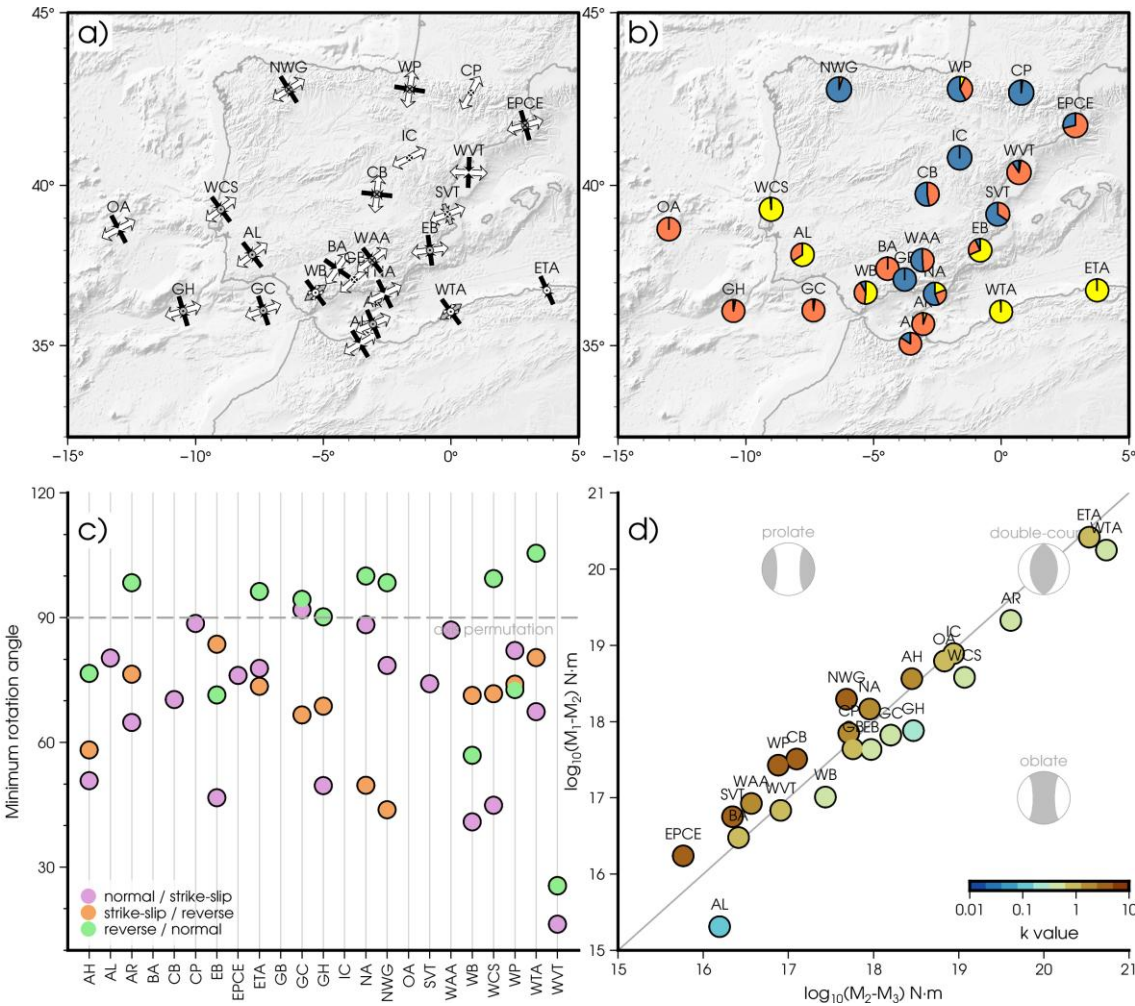
Figure 11: a) Strain principal directions derived from the combined moment tensors. Black shows the orientation of the shortening (P) axis; in white is shown the stretching axis (T) and grey the intermediate axis. The orientations are simplified showing only the trend of the principal axes and omitting the plunge. Note that the intermediate axis (in grey) can be a shortening or a stretching axis; when it is the vertical axis it is represented by a circle with a cross or with a dot respectively. **b)** Pie diagram showing the proportion of seismic moment released by strike-slip (red), reverse (yellow) and normal (blue) events on each zone. **c)** Representation of the minimum rotation angle (Kagan angle) between combined focal mechanisms for the different rupture types in each zone. A 90° angle represents a pure axes permutation. **d)** Flinn diagram adapted to the combined seismic strain tensor. Each circle represents the position on the diagram of each zone considered in the study. The color is proportional to the k value as is shown in the color scale. The gray tensors represent the seismic strain tensors for prolate, double-couple (plane strain) and oblate shape ellipsoids. The diagonal line represents the plane strain shapes, pure double couple in seismic tensor terminology. Note that the scales used for color and graph axes are logarithmic.
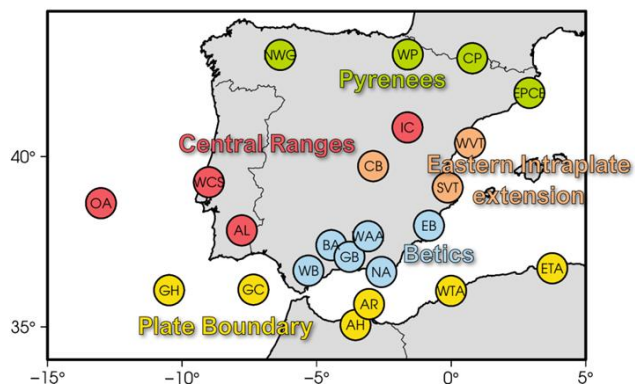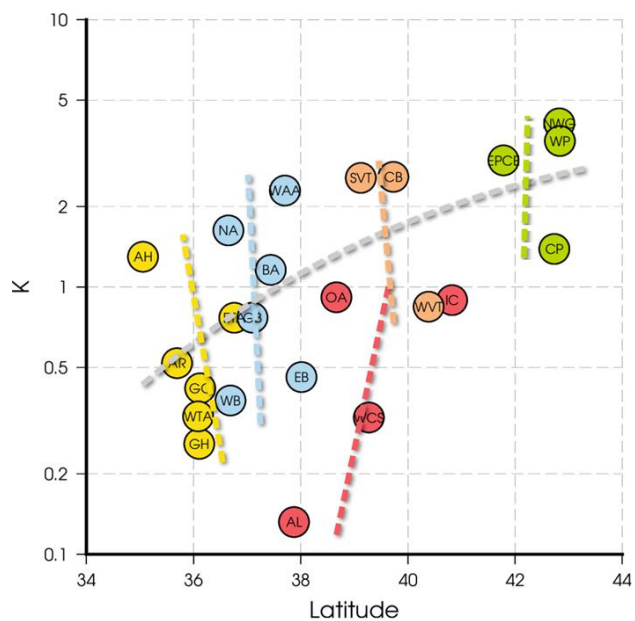
Figure 12: Relationship between the k-value of the strain tensor and the latitude of the zone. The colours are related to the tectonic setting as shown in the map. The coloured dashed lines show the trend of each population, while the grey dashed line shows the general trend of K-value increment with latitude.
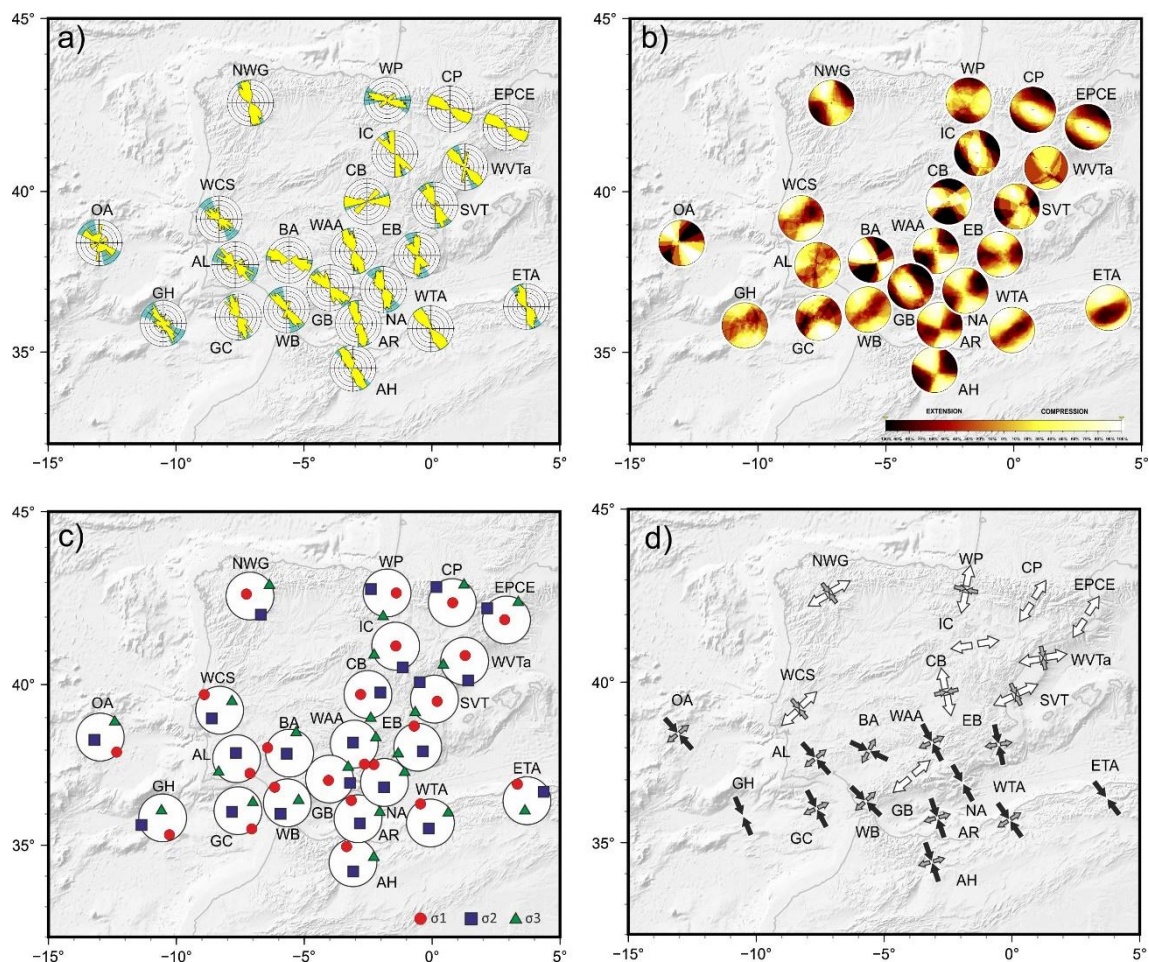
Figure 13: a) Deduced E$_{Hmax}$ (Dey, maximum horizontal shortening / minimum horizontal extension) in every considered zone from the Slip Model. b) Combined Right Dihedra plots. c) Stress inversions from focal mechanism populations in all the zones. d) scaled sizes of the stress horizontal axes, σ$_1$ (black), σ$_2$ (grey) and σ$_3$ (white).

945   The results of the Slip Model analysis regarding active deformation types are presented in Fig. 3. Variations in data density lead to poorly constrained interpolations in areas sparse coverage. Nevertheless, the inferred E$_{Hmax}$ (D$_{ey}$, maximum horizontal shortening / minimum horizontal extension) for each analysed zone (Fig. 13a) provided a coherent image of the progressive rotations of E$_{Hmax}$ in Iberia. Composed Right Dihedra plots yield qualitatively similar patterns (Fig. 13 b).

The stress inversion solutions (Figs. 13c, 13d, and 14) indicate that the most clearly defined thrust faulting stress regimes occur

950   at the margins of the study area, specifically in the Gorringe and Eastern Atlas, characterized by a vertical σ$_3$ and a stress ratio (R) around 0.4. In between, much of southern Iberia is dominated by strike-slip faulting stress regimes with a thrusting component (transpression), marked by vertical σ$_2$ and 0.5< R > 0. This pattern also extends into (WCS and AL). An exception is the Granada Basin, where the stress regime is nearly radial, dominated by normal faulting. This extensional regime influences nearby areas to the east and west—namely Western Alcaraz (WAA) and Antequera (BA)—where transtensional stress fields

955   prevail (vertical σ_2 and $0.5 < R < 1$) (Fig. 14). Similar transtensional regimes are also observed in Al Hoceima (AL) and the Offshore Atlantic (OA). The remaining inversions in the northern and northeastern sectors yield normal faulting stress regimes, with vertical σ_1 and R close to 0.5. Along the plate boundary (yellow in Fig. 14), the σ_1 orientation remains remarkably consistent, trending close to N154ºE. In the Betic Cordillera (blue in Fig. 14), some variability is observed, although the mean σ_1 orientation remains near N155°E, except in the Granada Basin, Antequera (BA), and the deeper seismicity of the Western

960   Betics, where σ_1 trends shift toward N114°E, likely reflecting the residual influence of the Alboran Slab. In the Central Ranges and Offshore Atlantic (red in Fig. 14), σ_1 rotates slightly counterclockwise to approximately N140°E, aligning with the Euler pole of Africa–Eurasia plate motion. In the Pyrenees, the eastern and western flanks of the range exhibit σ_1 orientations similar to those of the broader Iberian domain (around N154°E). However, in the central Pyrenees (CO and WPCP), σ_3 is oriented perpendicular to the mountain belt, suggesting that local stress sources—such as post-orogenic collapse

965   or isostatic rebound, dominate over the regional stress field. The Central Basins deviate from this overall pattern. The stress solution in the Eastern Pyrenees closely resembles those of the Valencia Through and the Iberian Chain (EPCE, WVT, SVT and IC), defining a coherent cluster of extensional stress regime in eastern Iberia (Fig. 14). Notably, in these solutions, σ_2 is oriented NW-SE rather than NE-SW, suggesting that the present-day normal faulting stress regime is likely to be more affected by the Africa-Eurasia convergence than by the back-arc extension of the easternmost subduction zones.

970   The presence of thrusting focal mechanisms along the leading edge of the Alboran Domain supports the hypothesis that its westwards emplacement facilitated the mechanical decoupling of Iberia from Africa. Similarly, the SPCS has progressively lost its thrust faulting stress regime from east to west, with thrusts activity north of Madrid ceasing since the Late Miocene. However, in its Portuguese sector, SPCS remains an active intraplate orogen. Consequently across central Iberia, from east to west, the stress regime transitions from a well-defined normal faulting stress regime in the IC, where σ_1 is vertical and R=0.43,

975   trough continued normal faulting in the Central Basins, to a thrust-faulting stress regime in the WCS, and finally to a strike-slip faulting stress regime in the offshore (OA)- This progression is accompanied by a gradual clockwise rotation of σ_2 or σ_1 from N148°E to N131°E (with the exception of CB), consistent with the expected stress orientation imposed by the Euler pole of Africa-Eurasia plate motion. Accordingly, the offshore continuation of the SPCS is expected to be governed by a transtensional tectonic regime.

980   Fig. 15 summarizes the results of the stress inversion. In regions where normal faulting stress regimes are inferred (blue arrows in Fig. 15), Cenozoic thrusts are no longer active, such as in North, Central, and Northeast Iberia. However, normal faulting stress regimes are active in areas that previously experienced compressional deformation, such as in the IC. Transtensional areas (green arrows in Fig. 15) are also likely responsible for the deactivation of thrusts in the Estremadura Spur (OC) and in areas adjacent to the Granada Basin (WAA and BA), where active normal faulting is observed. Mapped thrusts are predominant

985   in the Gorringe Bank and eastern Algeria (red arrows in Fig. 15). In the remaining areas, including the easternmost and westernmost Betics, and southwestern Iberia, transpressional regimes domains. Therefore, both mapped thrusts and strike-slip faults in these areas should be considered tectonically active structures.
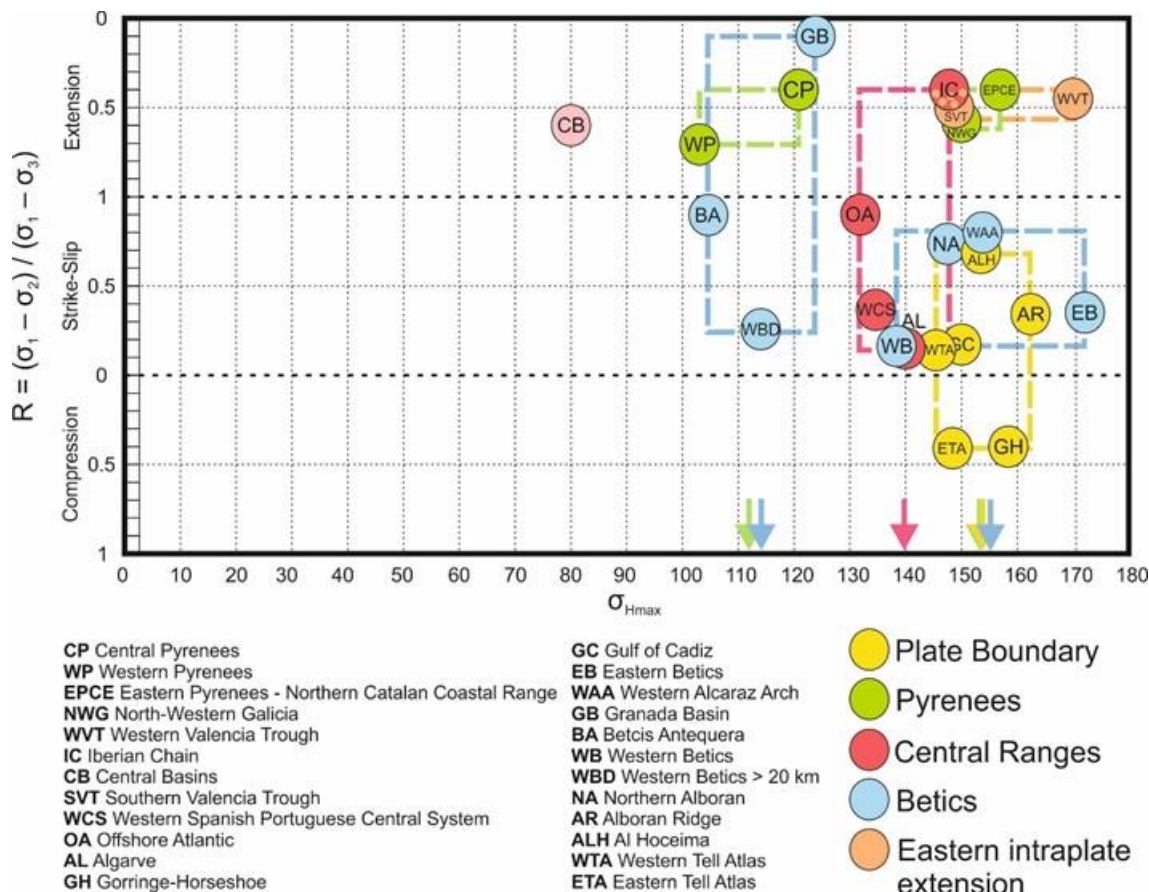
Figure 14: R (Stress tensor ratio) Vs S$_{Hmax}$ trend (σ_1 for thrusts and strike-slip faults stress regimes, σ_2 normal faulting stress regimes). The N-S direction is marked by 0° and 180°, while the E-W direction coincides with the value of 90. The areas considered have been grouped into those at the plate boundary (yellow, AR, GH, ETA, GC, WTA, and ALH), those in the Pyrenees (green, EPCE, NWG, CP, and WP), those in the Central Ranges (in red, OA, WCS, AL and IC), those in the Betics (in blue, separated BA, GB, WBD from the strike-strike solutions BA, GB, WBD), those related to the intraplate extension in E Iberia (Mediterranean) (in orange, WVT, SVT and IC. The latter is also included in the Central Ranges solution. CB (in pink) does not seem to be related to any of the previous groupings. The dashed rectangles mark each group's maximum and minimum values of R and S$_{Hmax}$, with their corresponding colour. The lower arrows indicate the average values of S$_{Hmax}$ for each group.

Figure 15: Summarized state of stress of Iberia based on focal mechanism stress inversion from this study.
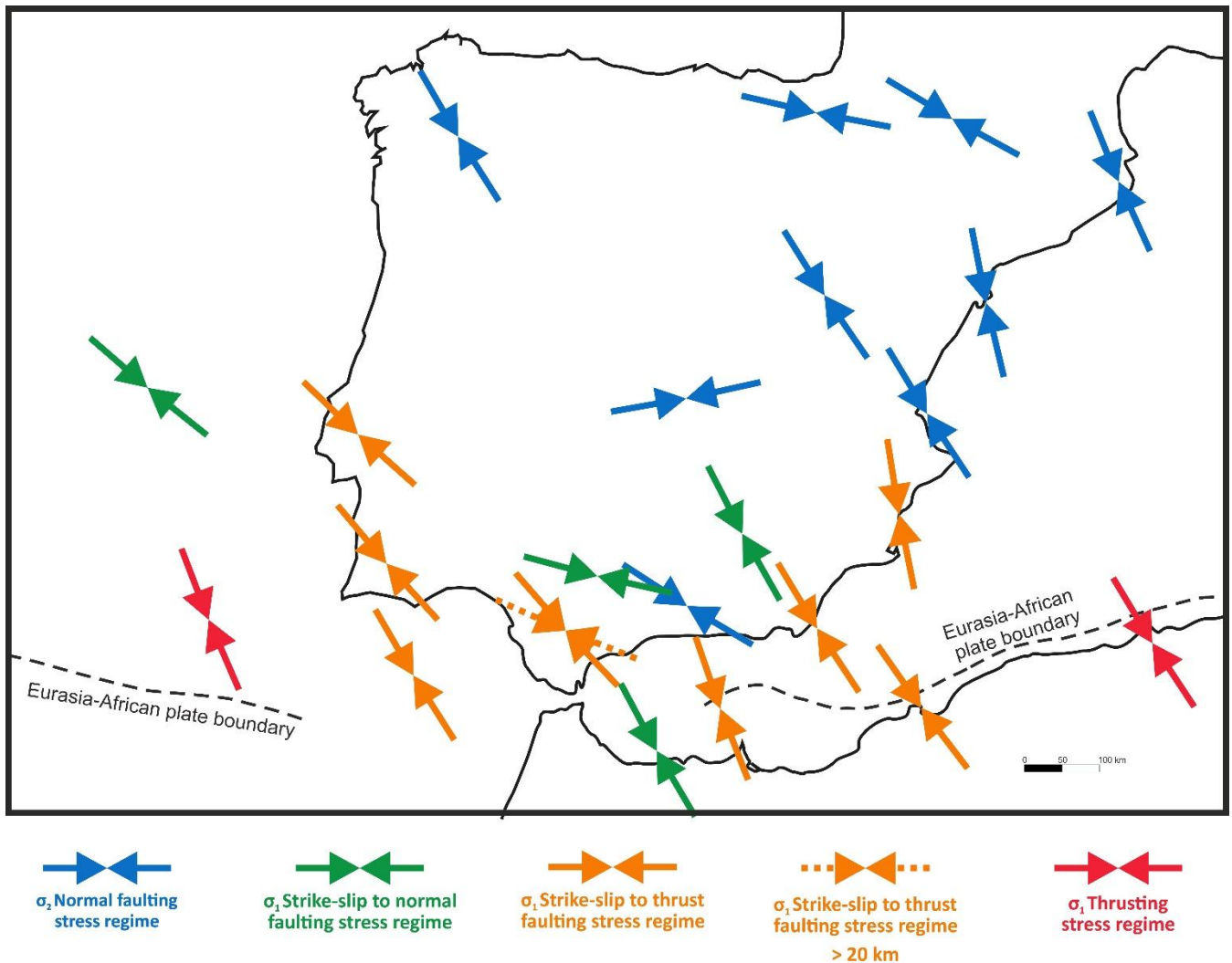
7 Conclusions

- Based on the combination of methods used to establish the characteristics of the type of active deformation and the associated stresses, it should be noted that they are all complementary, providing compatible results that highlight different tectonic features. Thus, the direct application of the Slip Model yields results that are easy to obtain and useful when establishing a tectonic zoning framework for applying the set of methodologies. The Right Dihedral method provides handy visual information for understanding the results of the Composite Analysis of focal mechanisms and Stress Inversion. These last two methods are the most comprehensive, with numerical results that

can be used to compare the tectonic characteristics of the different analysed areas. In any case, the use of diverse

1010 methods provides a more comprehensive overview of the characteristics of active tectonics in Iberia.

- From the Slip Model results and the available information on the neotectonic structural deformation, we have subdivided Iberia in this way: In the Pyrenees, we identified three zones: the Central Pyrenees (CP), with normal faulting focal mechanisms, and two more zones at the eastern and western ends, the Western Pyrenees (WP) and the Eastern Pyrenees - Northern Catalan Coastal Range (EPCE). On the north edge, we grouped the earthquakes in North-

1015 Western Galicia (NWG). In the east of the peninsula, offshore near the coast, we have differentiated two tectonic zones: the North Valencia Trough (NVT) and the South Valencia Trough (SVT). In central Iberia, we have separated the focal mechanisms in the Iberian Chain (IC) and south of the eastern SPCS (Central Basins, CB), as well as those in the tectonic zone near Lisbon, which we refer to as the Western Central System (WCS). Further south but not yet at the active plate boundary, we defined the Algarve (AL) as a tectonic zone in SW Iberia. In the offshore Atlantic to the

1020 west, we grouped them in the tectonic zone Offshore Atlantic (OA). Further south, primarily offshore and along the plate boundary, we examined the Gorringe-Horseshoe (GH) and Gulf of Cádiz (GC) tectonic zones. Considering the predominance of normal faulting in the Granada Basin (GB), we differentiated the Western Betics (WB) to its west, the Betics Antequera (BA) to its north, and the Eastern Betics (EB) to its east. In the Alboran Sea, we considered the North Alboran (NA), which also has onshore focal mechanisms, and the Alboran Ridge (AR), located at the

1025 probable plate boundary. Further south, on the African Plate, in the Rif, we considered the tectonic zones of Al Hoceima (ALH) and Rif (RF). Finally, in the Algerian Atlas, we analysed two populations: one located further east, the Eastern Tell Atlas (ETA), and the other located further west, the Western Tell Atlas (WTA).

- In CP, the combined moment tensor is close to a double couple with an almost pure permutation between the B and P axes. Meanwhile, the stress inversion indicates a nearly uniaxial normal faulting stress regime, with a σ_3 direction

1030 of N005°E-N030°E, sub-perpendicular to the topographic axis of the range. In WP, the combined moment tensor has mainly sheared characteristics with a prolate tensor with the extensional axis in N011°E and permutation between B and P axes. The stress inversion also results in a normal faulting stress regime, similar to that in CP. However, the stress tensor shows characteristics closer to strike-slip, with σ_2 at N103°E. EPCE has a combined moment tensor that departs from a pure double couple with permutation between the P and B axes and a prolate ellipsoid with the

1035 maximum shortening almost horizontal at N163°E. The stress inversion indicates a more normal faulting stress regime (σ_2 at N165°E) concerning CP and very similar to those found to the south in IC, WVT, and SVT, so it seems to be less related to the local processes affecting the Pyrenees. The NWG combined moment tensor shows a prolate form, dominated by ENE-WSE extension, with the P (or B) axis showing an orientation of N147°E. The stress inversion provides a normal faulting stress regime, with a σ_2 strike between N147°E and N150°E. The most normal faulting

1040 mechanisms are concentrated in the area where small sedimentary basins developed during the Miocene. In contrast, the offshore region is dominated by strike-slip faulting. The Castor CO_2 storage project generated a sequence of apparently triggered seismicity in the NVT. The combined moment tensor shows an N082°E trending T axis and an

immersion of 19°, whereas the P axis is oriented N002°E, with an immersion of 28°. The stress inversion is a very consistent solution, revealing a normal faulting stress regime compatible with strike-slip and σ_2 oriented N170°E. The eight focal mechanisms in the IC indicate normal faulting, with some events exhibiting strike-slip component, which combined give rise to a pure double-couple tensor characterized by a horizontal T-axis oriented N064°E and B-axis oriented N154°E. The stress inversion yields a triaxial normal faulting stress regime solution, with σ_3 oriented N058°E, closely resembling the stress field observed in the WVT. In CB, the combined moment tensor displays a prolate-type shape dominated by a strain axis oriented N005°E and a maximum shortening axis oriented approximately E-W. The stress inversion indicates a normal faulting stress regime solution with a minor strike-slip component, characterized by σ_3 oriented N173°E, nearly orthogonal to that inferred for the CI and distinct from most other analysed areas. In WCS, the focal mechanisms are predominantly reverse or strike-slip faulting events, with some normal faulting events whose T and B axes are kinematically compatible. The combined mechanisms have a T and B permutation. The axis of maximum shortening trends N146°E, while the axis of maximum extension is oriented N056°E. The stress inversion yields a well constrained thrust faulting stress regime solution with a minor strike-slip component, with σ_1 oriented N134°E. This stress regime activates NE-SW striking thrust faults and left-lateral NNE striking and right-lateral ESE striking strike-slip faults. OA, with dispersed focal mechanisms, strike-slip displacements with a minor normal component predominates. The combined moment tensor exhibits an oblate shape, with the P axis orientation of N152°E. The extension T-axis is in the N057°E direction. The stress inversion indicates a strike-slip stress regime with a normal component, characterised by σ_1 trending N131°E and σ_3 at N044°E. At the active plate boundary, the GH zone has 13 reverse and strike-slip focal mechanisms, several of which are below the Moho, that indicate a thrust-faulting stress regime with σ_1 at N159°E. The combined moment tensor presents an oblate shape, dominated by shortening. The orientations of the P and T axes are N155°E and N065°E, respectively. In the eastern SVT, the combined tensor reveals a permutation between the B and P axes, with extension predominantly oriented N069°E. The corresponding stress tensor yields a normal faulting stress regime with σ_3 at N058°E, which is very similar to those of IC, WVT, and EPCE. The AL zone has a combined strain tensor with an orientation of the maximum shortening axis at N143°E, but is far from a double couple with an oblate tensor shape. The inversion indicates a thrust-faulting stress with σ_1 at N140°E, which activates NE-SW striking thrust faults and left-lateral N-S and NW-SE striking right-lateral strike-slip faults. The solution is very similar to that obtained for the WCS, showing that this type of stress predominates throughout the SW corner of Iberia, to the west of the Betic front. Results from the Betics have a higher variability. The EB zone has a combined mechanism that gives rise to an oblate-shaped strain tensor, dominated by shortening. The P axis has an N172°E orientation, although the P axes of all mechanisms have a large scatter. The stress inversion provides a thrust-to-strike-slip faulting stress regime with σ_1 at N171°E, which can activate NE-SW to ENE-WSW striking thrust faults, as well as right-lateral NW-SE and left-lateral NNE-SSW striking strike-slip faults. The WAA zone has a combined strain tensor with a prolate shape, with the orientation of the T axis at N052°E, while the P axis has an orientation of N142°E. The stress tensor obtained by inversion indicates

a strike-slip stress regime with a normal component, characterized by σ_1 at N153°E. This stress regime activates left lateral N-S and right lateral ESE-WNW strike-slip faults, as well as NW-SE normal faults. The GB zone has normal focal mechanisms and clusters into two families, whose T-axis orientations form an angle of 30-40° with each other. The combined moment tensor is of oblate type with the T axis having an orientation of N048°E, and the B axis of N139°E. Our stress inversion provides a highly consistent triaxial normal faulting stress regime with σ_3 striking at N033°E. Therefore, this stress orientation is congruent with that obtained from the E (WAA and EB). In the NA zone, the combined moment tensor is a slightly prolate strike-slip deformation tensor, with an extensional stress axis at N065°E, while the shortening axis has an N154°E trend. The stress inversion result is similar to those of WAA and EB, with a strike-slip stress regime with a normal component, characterized by σ_1 in N149°E and σ_3 in N064°E. The AR zone is characterized by a combined moment tensor that has an oblate shape, with shortening at N157°E. The mean T strain axis is N069°E. The inversion indicates a transpressive strike-slip faulting stress regime, with σ_1 at N161°E, which activates mainly N-S to NNE-SSW left-lateral faults, NW-SW right-lateral strike-slip faults, and E-W to ENE-WSW thrust faults. The stress solution lies between that of the EB and WAA. The ALH zone exhibits focal mechanisms with highly consistent axes of maximum shortening and horizontal extension, showing minimal variability. The combined moment tensor indicates a strike-slip deformation with an extension component close to a double couple, with the P axis at N143°E and the T axis N060°E. The WTA zone has an oblate reverse combined moment tensor with the P axis having an orientation N143°E and the B axis N050°E. In contrast, the ETA zone is also of a shortening type and oblate, although it is closer to the double couple, with the P axis oriented N155°E and the B axis N069°E. The stress inversions show a very similar σ_1 orientation for both zones N149°E (west) and N145°E (east), with a thrust-faulting stress regime to the east, and with a larger strike-slip component in the west. Both solutions activate NE-SW striking thrust faults, NW-SE right-lateral and N-S left-lateral strike-slip faults. In GC, there is a strike-slip seismic moment tensor but with an oblate shape, with the P-axis having an orientation of N161°E, and the T-axis is N066°E. The inversion provides a strike-slip stress regime with σ_1 at N150°E, with less thrusting component than that obtained for AL, GH, and WCS. We have separated the WB zone focal mechanisms according to their hypocentral depth (20 km). For the intermediate earthquakes, we have received a σ_1 trend between N113°E and N126°E. In contrast, earthquakes with hypocentral depths of more than 20 km provide a σ_1 of N114°E trend, more E-W than the shallow ones, confirming that the Alboran slab effect is more pronounced at greater depths. The combination of the focal mechanisms gives rise to a shortening-strike-slip seismic moment tensor with an oblate shape, with a P axis oriented at N143°E and the B axis at N046°E, although with a 28° plunge. Finally, the BA zone results in a combined strain tensor very close to a double couple, with a P axis of N125°E and the T axis of N028°E. The inversion of the five focal mechanisms reveals a strike-slip stress regime with a normal component, characterized by σ_1 at N105°E, which activates right-lateral strike-slip-normal (transtensional) faults.

- The overall interpretation of the results indicates that, in general, the shape of the combined seismic moment tensors at the plate boundary is oblate ($k < 1$), indicative of a predominance of transpressive deformation. As we move away

from the plate boundary, the tensors become prolate in shape ($k > 1$), consistent with extensional context of the Pyrenees, the Valencia Trough, and the Central Basins. An exception to this rule is the combined tensor of the Granada Basin, which yielded a pure normal faulting tensor close to the plate boundary. Similar tendencies are observed from the rescaled shape factor of the Slip Model (k'). Northern Algeria and southwestern Portugal represent the areas of maximum compression, closely associated with the plate boundary, whereas the Pyrenees and the Iberian Chain are characterized by extension. Individual calculations obtained from the Slip Model allow for distinguishing local variations. The proposed methodology optimizes the selection of focal mechanism populations for both kinematic and dynamic analyses. Although most of the defined tectonic zones exhibit focal mechanisms of different faulting types, the minimum rotation angle between their combined mechanisms indicates that they are compatible with each other, considering the axes permutation, in a context of distributed deformation. The orientations of the shortening and extension axes derived from the combined deformation tensors are generally consistent with the principal stress axes obtained from stress inversion, although notable discrepancies exist in certain regions

- Stress inversion results indicate that outside of the Iberian Peninsula, thrust faulting stress regimes dominate in the Gorringe and Eastern Atlas zones, characterized by a vertical σ_3 and R around 0.4. In southern Iberia, transpressional regime predominates, defined by strike-slip faulting stress regimes with a thrusting component, where vertical σ_2 and $0.5 > R > 0$. This stress configuration also extends into the southwestern corner of the Iberian Peninsula, particularly in the Western Spanish Portuguese Central System and the Algarve. Transtensional (strike-slip faulting stress regimes with a normal faulting component, vertical σ_2 and $1 > R > 0,5$) surround the normal faulting stress regime inferred for the Granada Basin (Western Alcaraz and Antequera) and are also present in northern Morocco (Al Hoceima) and Offshore Atlantic. Towards the Betics foreland and to the east of the westernmost sector of the Spanish Portuguese Central System, including the Pyrenees, a normal faulting stress regime predominates. Within these zones, a slight strike-slip component is observed west of the Central Pyrenees, in Western Pyrenees and North-Western Galicia. Regardless, R values in these zones are close to 0.5, except in the Granada Basin, where an almost radial normal faulting stress regime is found. The S_{Hmax} mean values range from N105°E to N155°E (except for the Central Basins solution). The S_{Hmax} orientation derived from this study, based on both individual focal mechanisms and stress inversion, is broadly consistent with data records from other stress indicators, particularly from the numerous borehole logging data previously published as part of the World Stress Map (Heidbach et al., 2018). Central part of Iberia is an exception, likely due to sparse data coverage resulting in large rotations of S_{Hmax} from the regional trend, or to horizontal stress magnitudes being close to each other, allowing for local stress variability due to stiffness and density contrasts. Regionally anomalous ESE–WNW S_{Hmax} orientations are found in the Granada Basin and the Pyrenees, where local stress fields dominate. Elsewhere, the Central Ranges (IC, WCS, OA, and AL) exhibit a consistent S_{Hmax} trend around N140°E. Although the Betic Cordillera (excluding the Granada Basin) shows some variability, it generally follows a mean S_{Hmax} N155°E, similar to the trends observed in the NW and NE corners of Iberia (EPCS and NWG). Solutions along the plate boundary also align with this S_{Hmax} trend N155°E, which likely reflects

1145   convergence direction of the Africa and Iberia plates. The 15º anticlockwise rotation to the north is interpreted as a consequence of the Euler pole location between the two plates. This general tectonic context seems to be overprinting the back-arc subduction-related extension in the east of Iberia and the Alboran Sea.
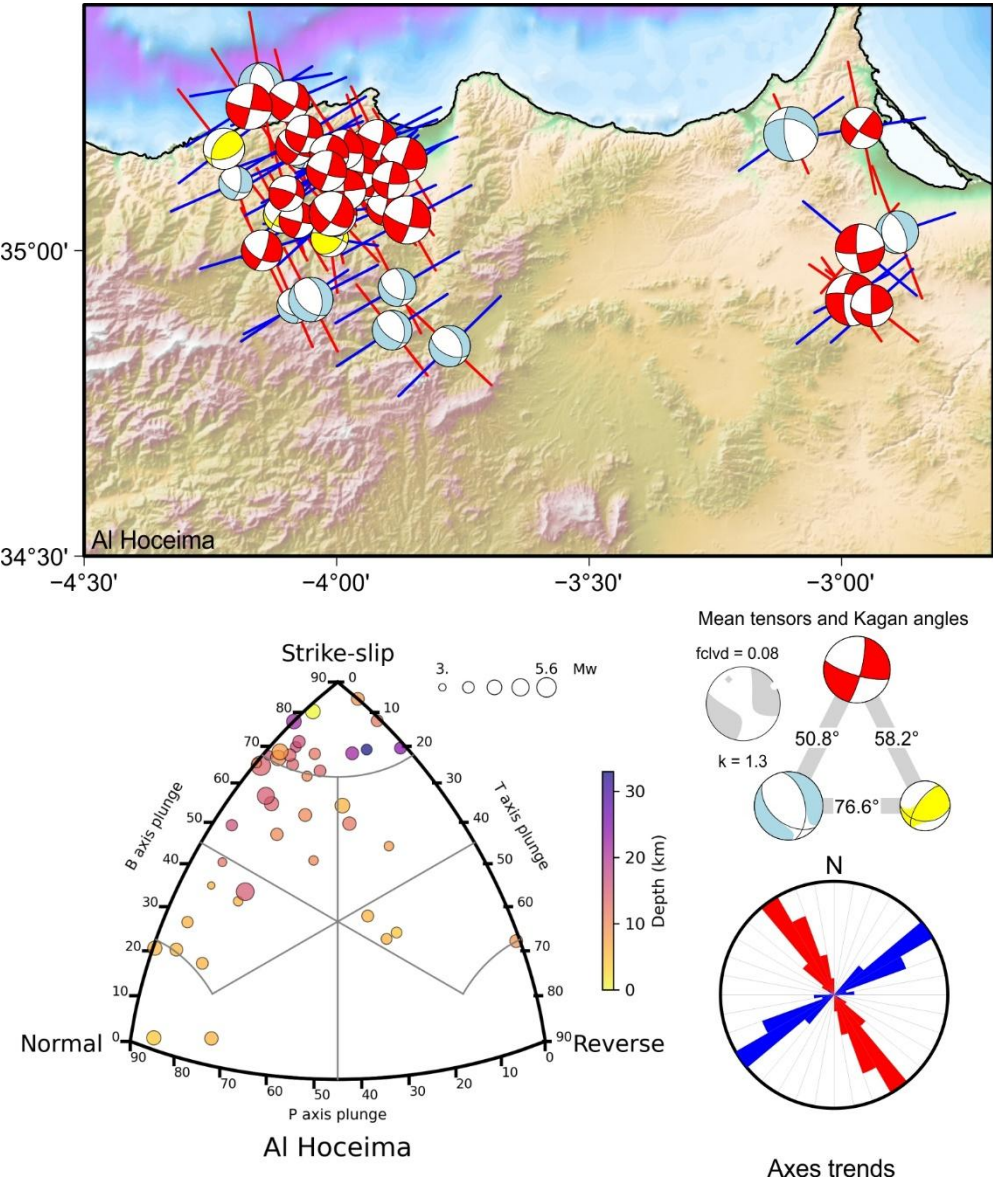
Fig. A1: Al Hoceima tectonic zone. Top map: focal mechanisms with maximum horizontal axis (P or B for normal ruptures) and minimum horizontal axis (T or B for reverse ruptures) orientation. Bottom left classification diagram for earthquake rupture types.
1155 **Middle right: Average tensors (complete in gray) and Kagan angles between the average tensors for each rupture type. Bottom right: Rose diagram of maximum and minimum horizontal axes orientation.**
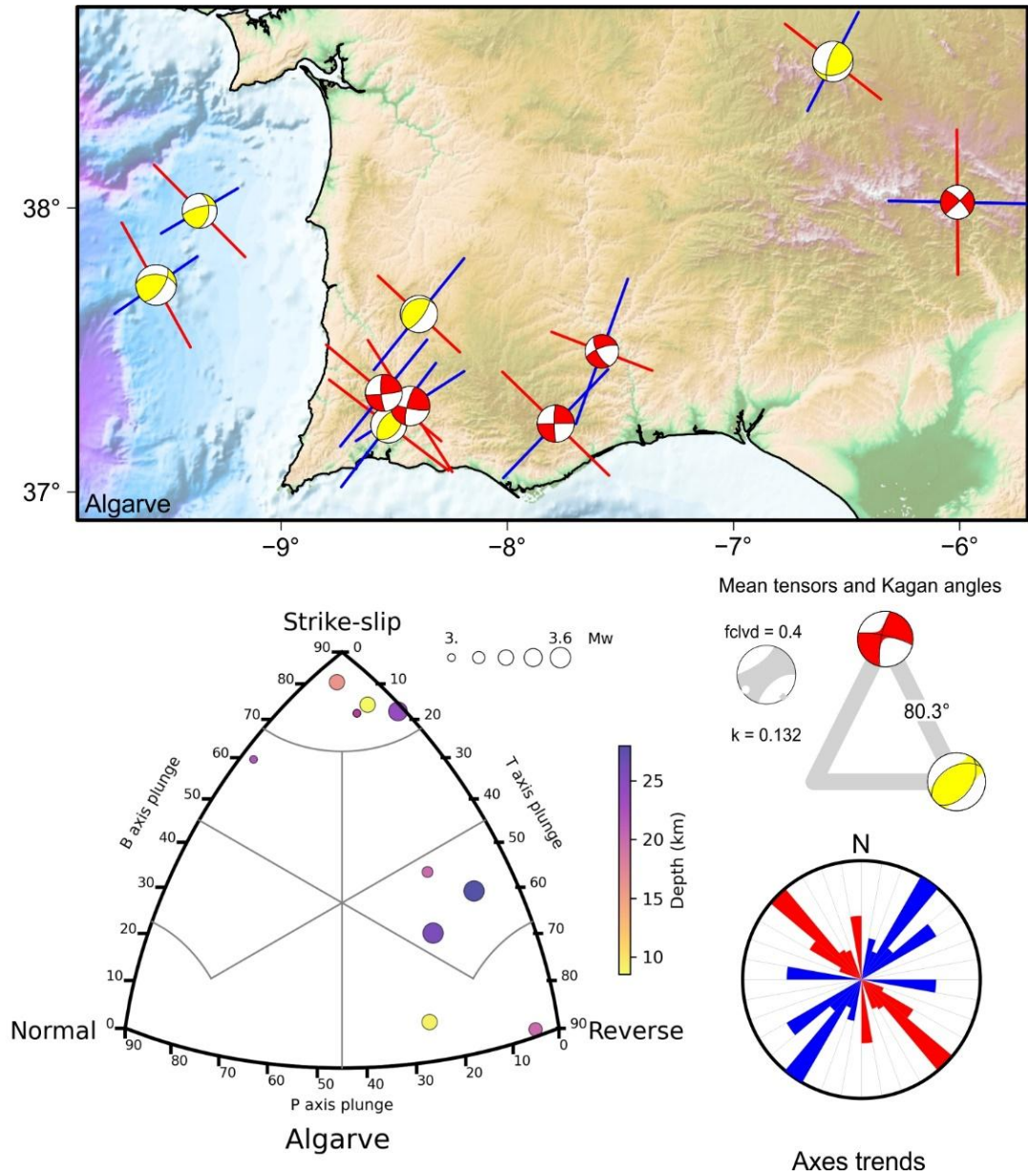
Fig. A2: Algarve tectonic zone. Top map: focal mechanisms with maximum horizontal axis (P or B for normal ruptures) and minimum horizontal axis (T or B for reverse ruptures) orientation. Bottom left classification diagram for earthquake rupture types. Middle right: Average tensors (complete in gray) and Kagan angles between the average tensors for each rupture type. Bottom right: Rose diagram of maximum and minimum horizontal axes orientation.
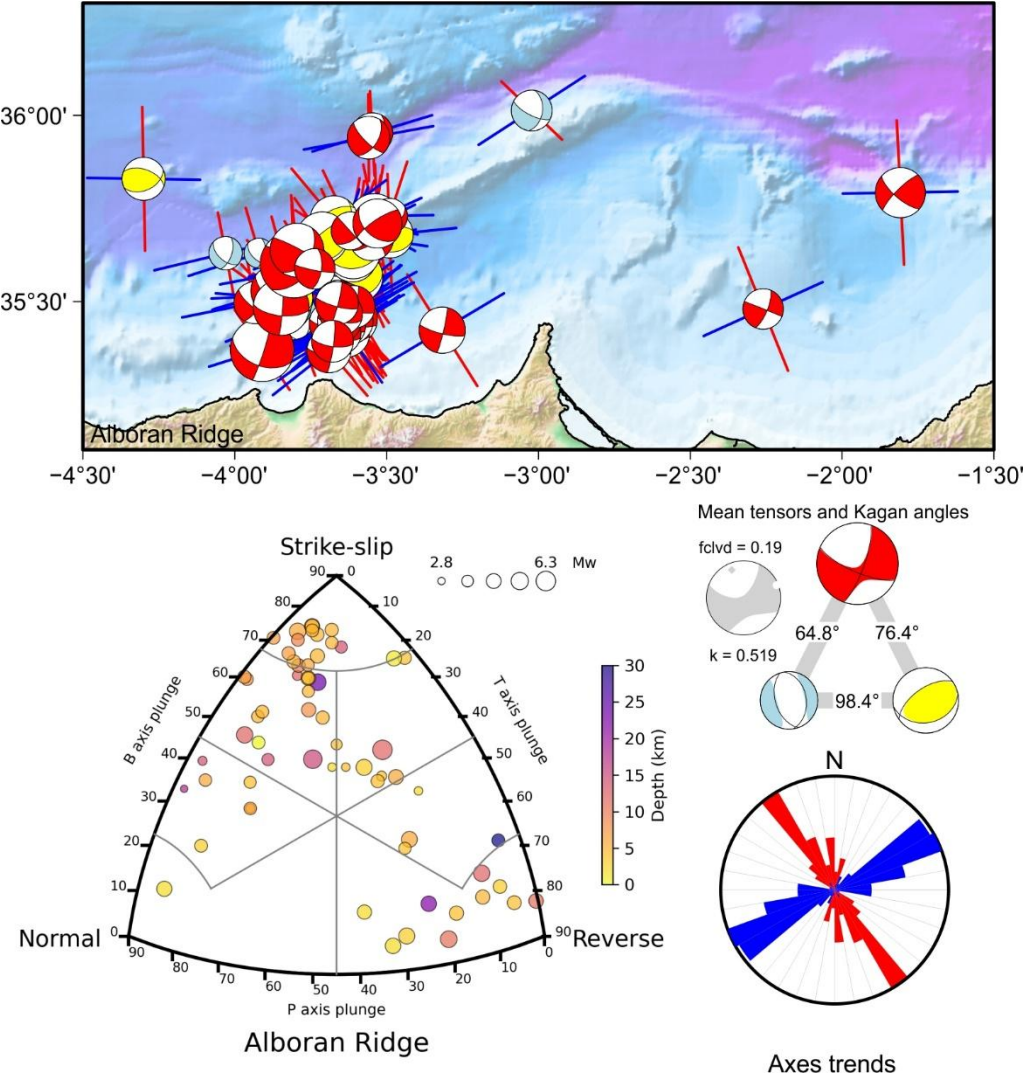
Fig. A3: Alboran Ridge tectonic zone. Top map: focal mechanisms with maximum horizontal axis (P or B for normal ruptures) and minimum horizontal axis (T or B for reverse ruptures) orientation. Bottom left classification diagram for earthquake rupture types. Middle right: Average tensors (complete in gray) and Kagan angles between the average tensors for each rupture type. Bottom right: Rose diagram of maximum and minimum horizontal axes orientation.
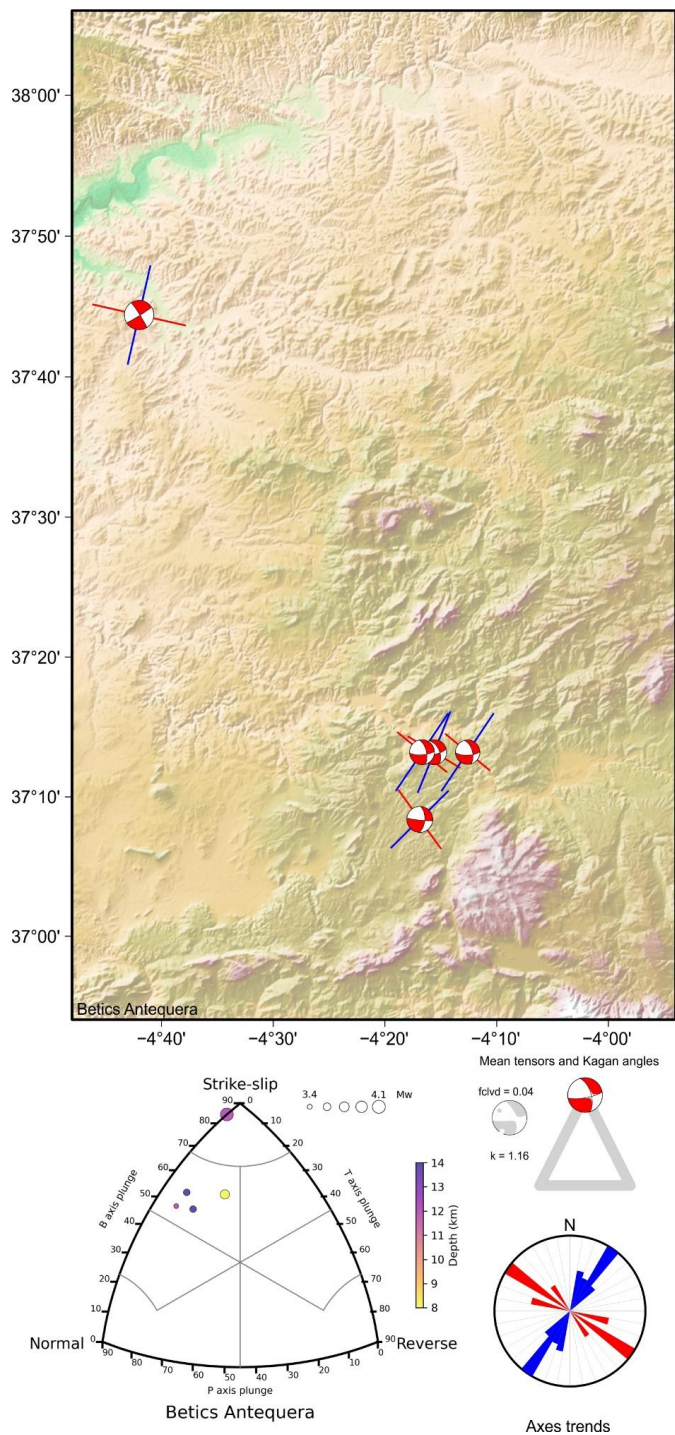
Fig. A4: Betics Antequera tectonic zone. Top map: focal mechanisms with maximum horizontal axis (P or B for normal ruptures) and minimum horizontal axis (T or B for reverse ruptures) orientation. Bottom left classification diagram for earthquake rupture types. Middle right: Average tensors (complete in gray) and Kagan angles between the average tensors for each rupture type. Bottom right: Rose diagram of maximum and minimum horizontal axes orientation.
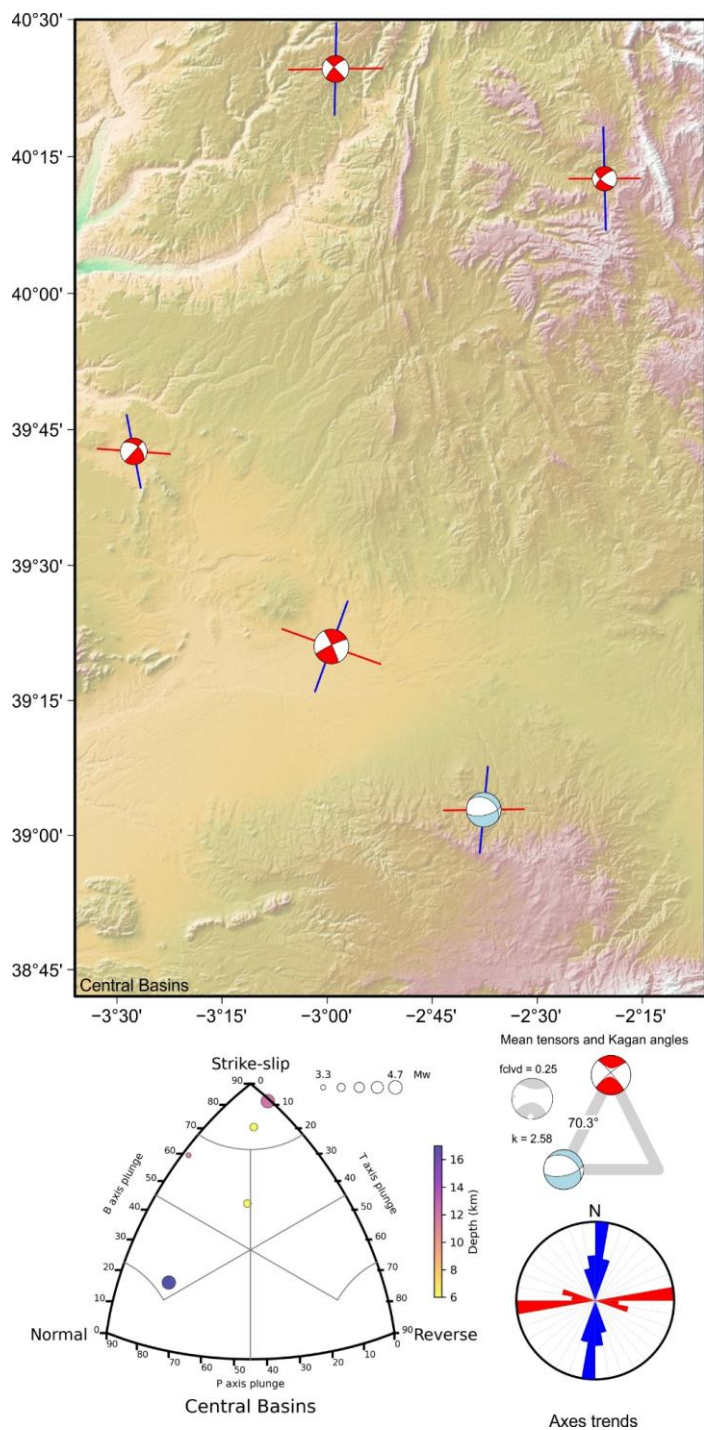
Fig. A5: Central Basins tectonic zone. Top map: focal mechanisms with maximum horizontal axis (P or B for normal ruptures) and minimum horizontal axis (T or B for reverse ruptures) orientation. Bottom left classification diagram for earthquake rupture types. Middle right: Average tensors (complete in gray) and Kagan angles between the average tensors for each rupture type. Bottom right: Rose diagram of maximum and minimum horizontal axes orientation.
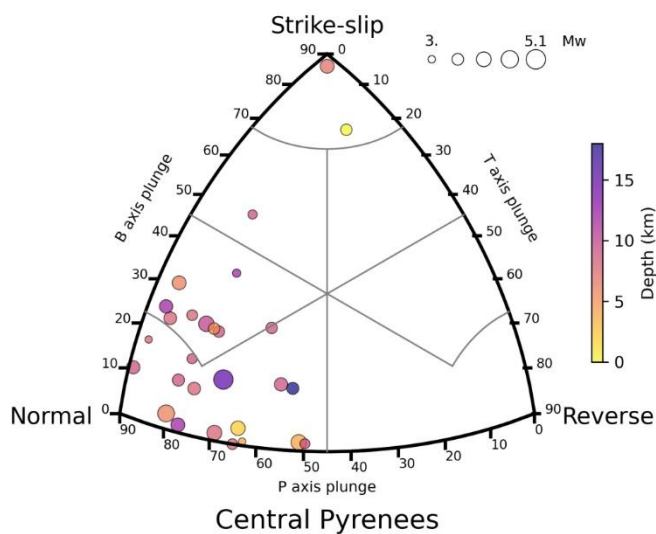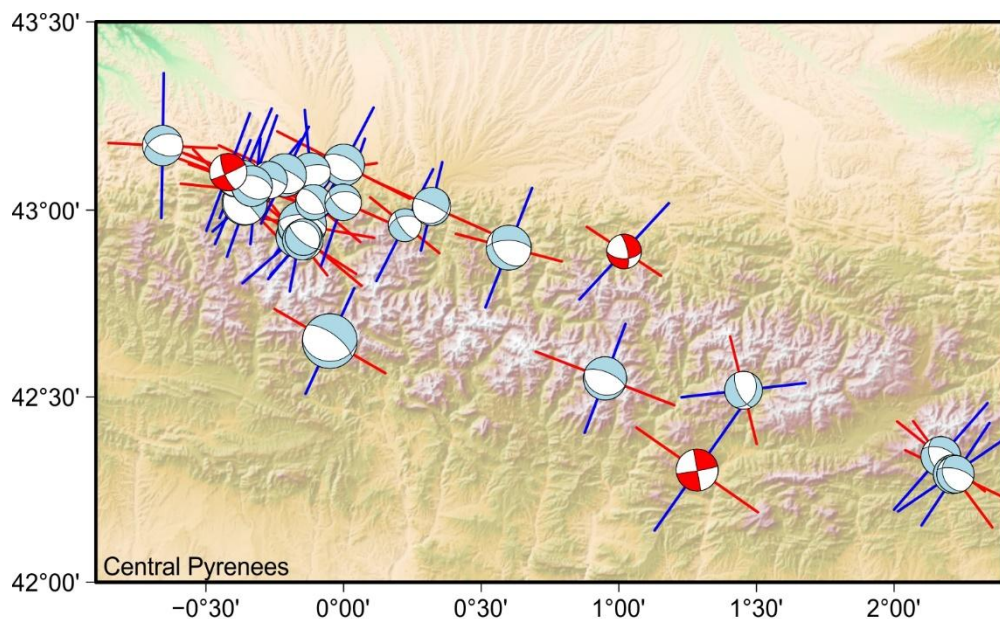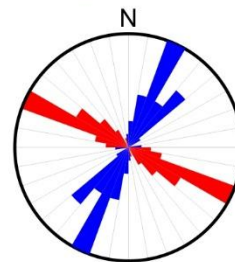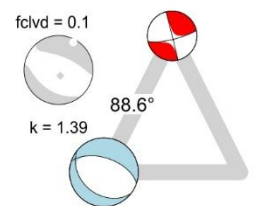
Fig. A6: Central Pyrenees tectonic zone. Top map: focal mechanisms with maximum horizontal axis (P or B for normal ruptures) and minimum horizontal axis (T or B for reverse ruptures) orientation. Bottom left classification diagram for earthquake rupture types. Middle right: Average tensors (complete in gray) and Kagan angles between the average tensors for each rupture type. Bottom right: Rose diagram of maximum and minimum horizontal axes orientation.

Fig. A7: Eastern Betics tectonic zone. Top map: focal mechanisms with maximum horizontal axis (P or B for normal ruptures) and minimum horizontal axis (T or B for reverse ruptures) orientation. Bottom left classification diagram for earthquake rupture types. Middle right: Average tensors (complete in gray) and Kagan angles between the average tensors for each rupture type. Bottom right: Rose diagram of maximum and minimum horizontal axes orientation.
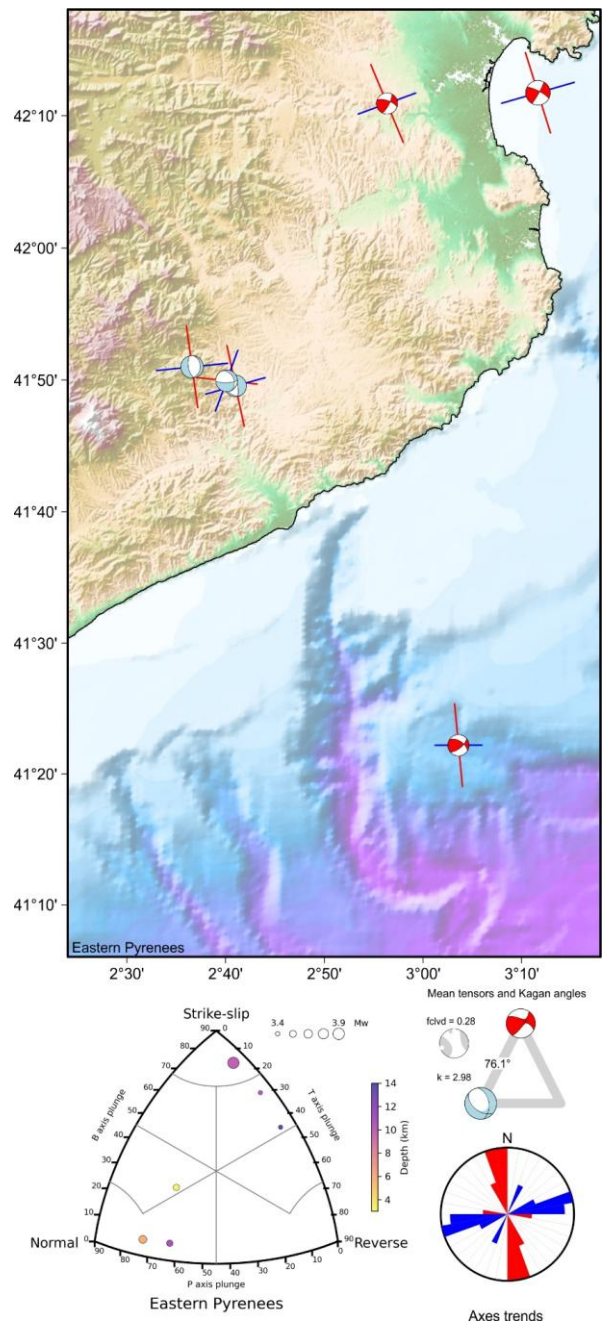
Fig. A8: Eastern Pyrenees tectonic zone. Top map: focal mechanisms with maximum horizontal axis (P or B for normal ruptures) and minimum horizontal axis (T or B for reverse ruptures) orientation. Bottom left classification diagram for earthquake rupture types. Middle right: Average tensors (complete in gray) and Kagan angles between the average tensors for each rupture type. Bottom right: Rose diagram of maximum and minimum horizontal axes orientation.
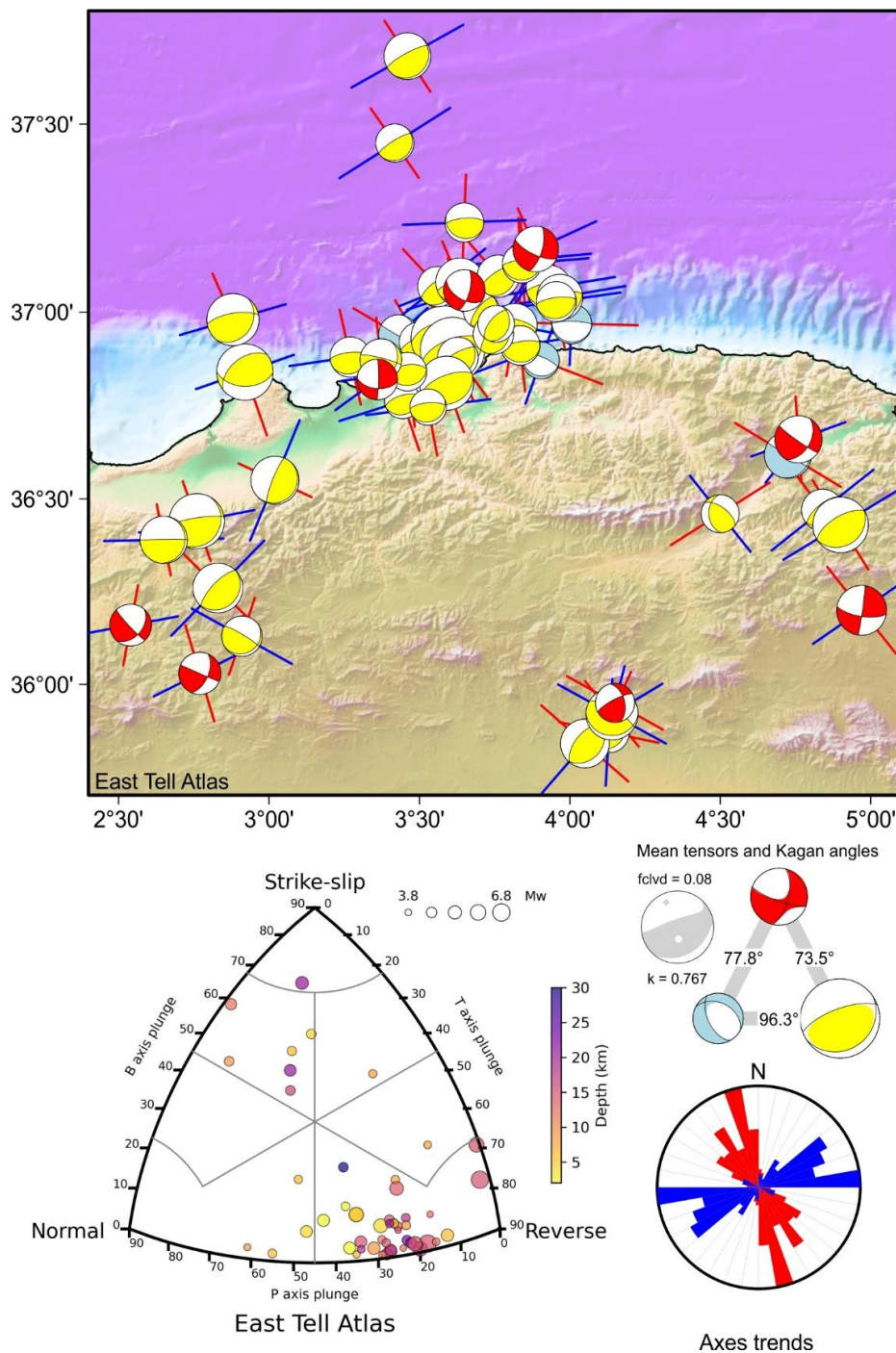
Fig. A9: East Tell Atlas tectonic zone. Top map: focal mechanisms with maximum horizontal axis (P or B for normal ruptures) and minimum horizontal axis (T or B for reverse ruptures) orientation. Bottom left classification diagram for earthquake rupture types. Middle right: Average tensors (complete in gray) and Kagan angles between the average tensors for each rupture type. Bottom right: Rose diagram of maximum and minimum horizontal axes orientation.
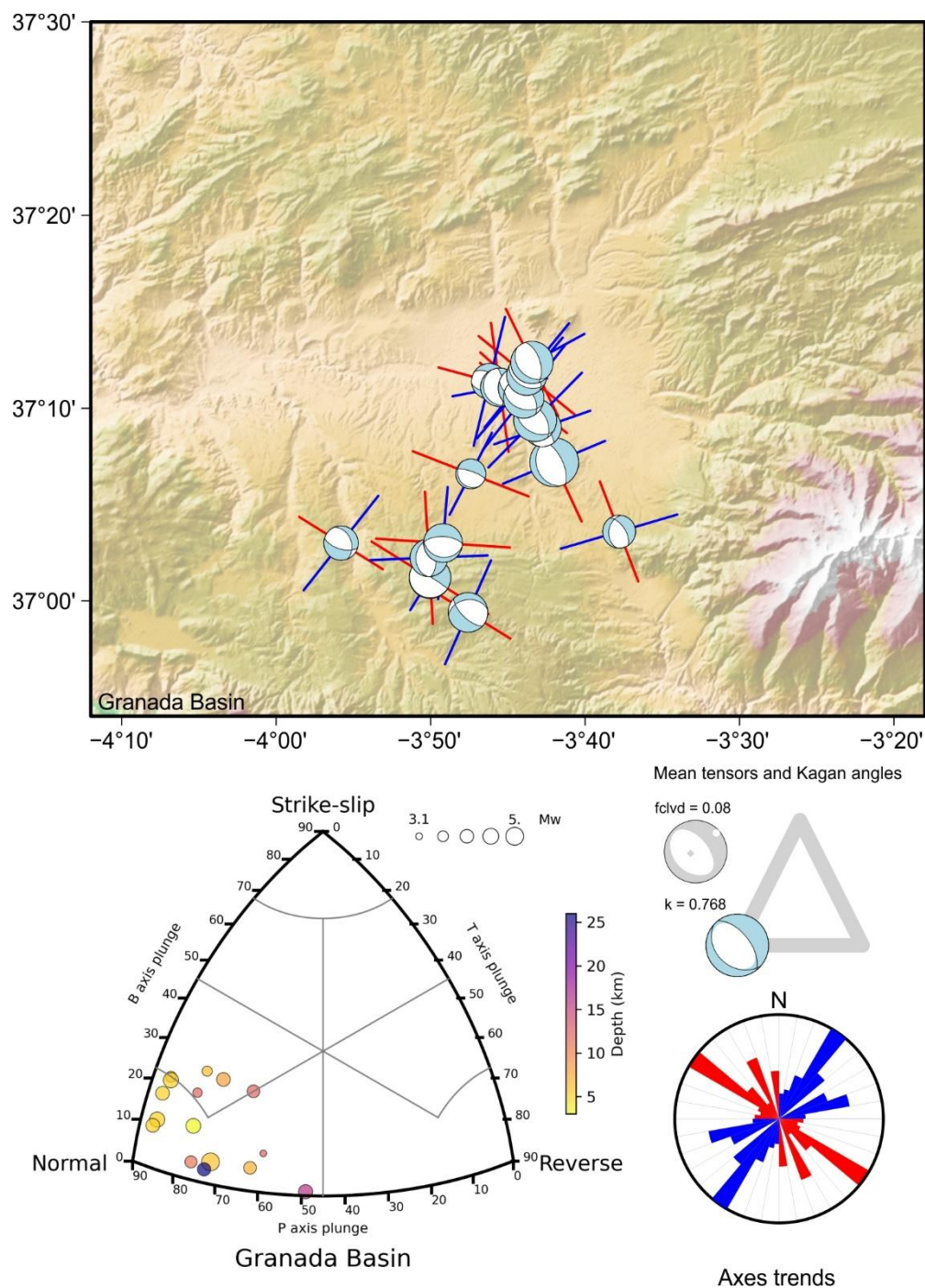
Fig. A10: Granada Basin tectonic zone. Top map: focal mechanisms with maximum horizontal axis (P or B for normal ruptures) and minimum horizontal axis (T or B for reverse ruptures) orientation. Bottom left classification diagram for earthquake rupture types. Middle right: Average tensors (complete in gray) and Kagan angles between the average tensors for each rupture type. Bottom right: Rose diagram of maximum and minimum horizontal axes orientation.
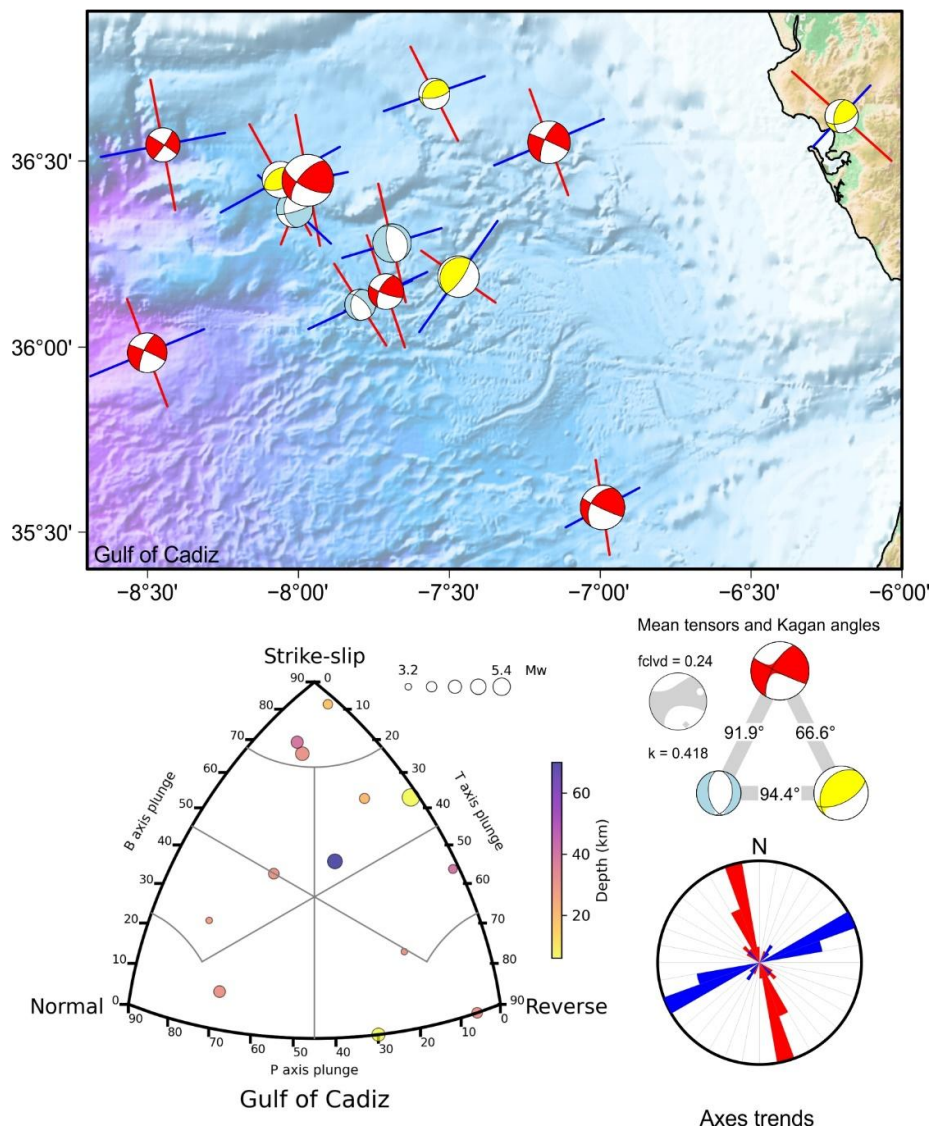
Fig. A11: Gulf of Cádiz tectonic zone. Top map: focal mechanisms with maximum horizontal axis (P or B for normal ruptures) and minimum horizontal axis (T or B for reverse ruptures) orientation. Bottom left classification diagram for earthquake rupture types. Middle right: Average tensors (complete in gray) and Kagan angles between the average tensors for each rupture type. Bottom right: Rose diagram of maximum and minimum horizontal axes orientation.
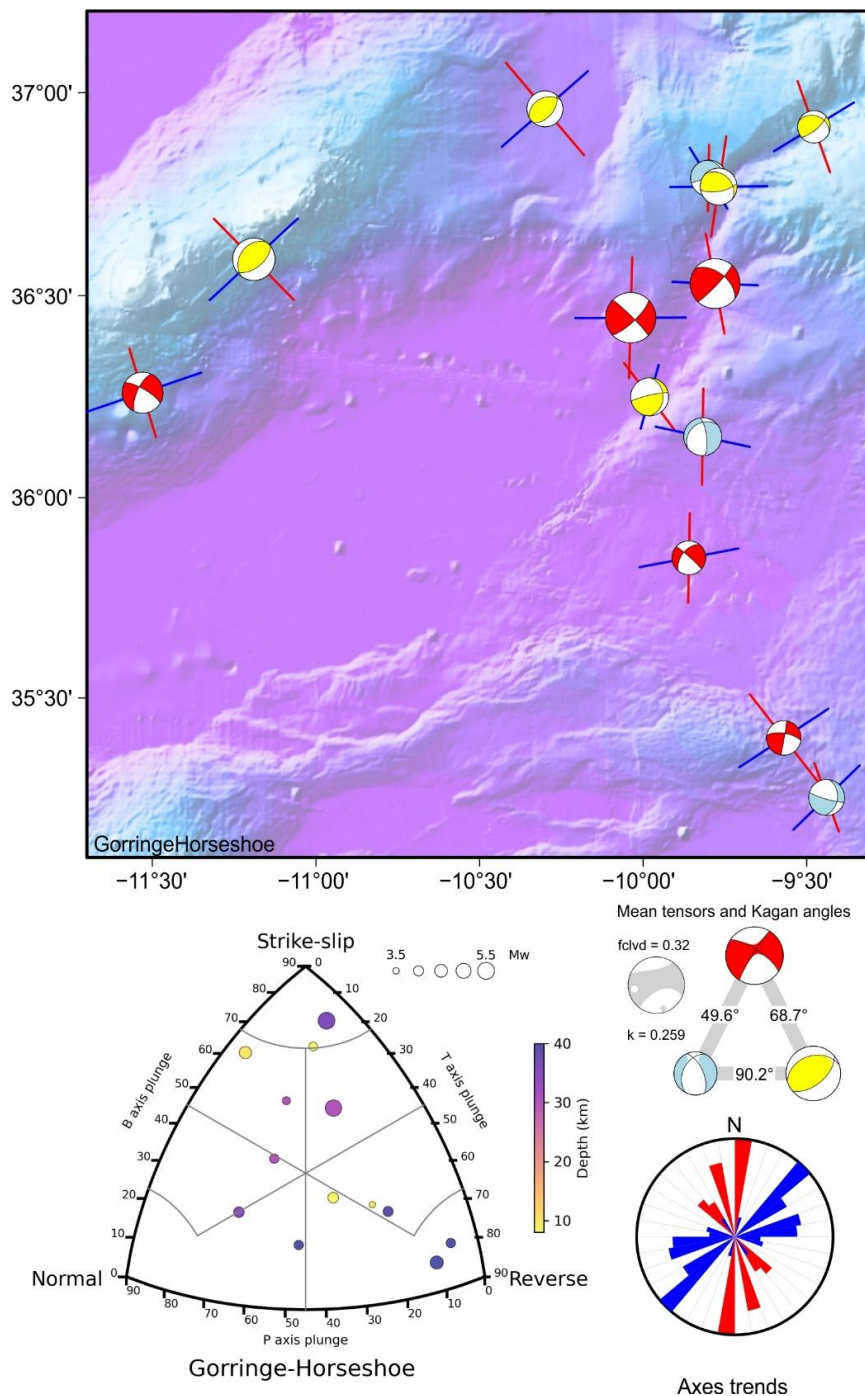
 Fig. A12: Gorringe-Horseshoe tectonic zone. Top map: focal mechanisms with maximum horizontal axis (P or B for normal ruptures) and minimum horizontal axis (T or B for reverse ruptures) orientation. Bottom left classification diagram for earthquake rupture types. Middle right: Average tensors (complete in gray) and Kagan angles between the average tensors for each rupture type. Bottom right: Rose diagram of maximum and minimum horizontal axes orientation.

1235 **Fig. A13: Iberian Chain tectonic zone. Top map: focal mechanisms with maximum horizontal axis (P or B for normal ruptures) and minimum horizontal axis (T or B for reverse ruptures) orientation. Bottom left classification diagram for earthquake rupture types. Middle right: Average tensors (complete in gray) and Kagan angles between the average tensors for each rupture type. Bottom right: Rose diagram of maximum and minimum horizontal axes orientation.**
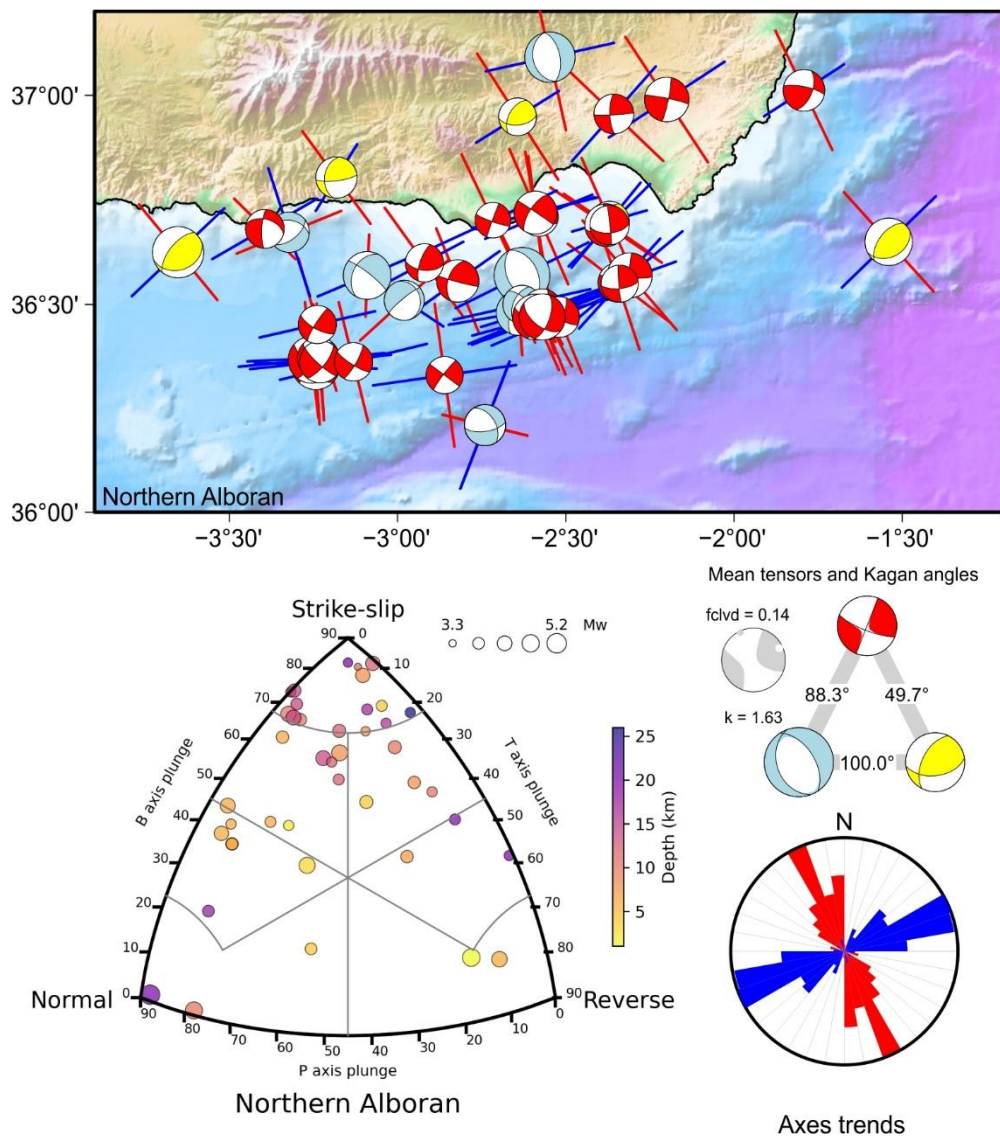
1240 **Fig. A14: Northern Alboran tectonic zone. Top map: focal mechanisms with maximum horizontal axis (P or B for normal ruptures) and minimum horizontal axis (T or B for reverse ruptures) orientation. Bottom left classification diagram for earthquake rupture types. Middle right: Average tensors (complete in gray) and Kagan angles between the average tensors for each rupture type. Bottom right: Rose diagram of maximum and minimum horizontal axes orientation.**
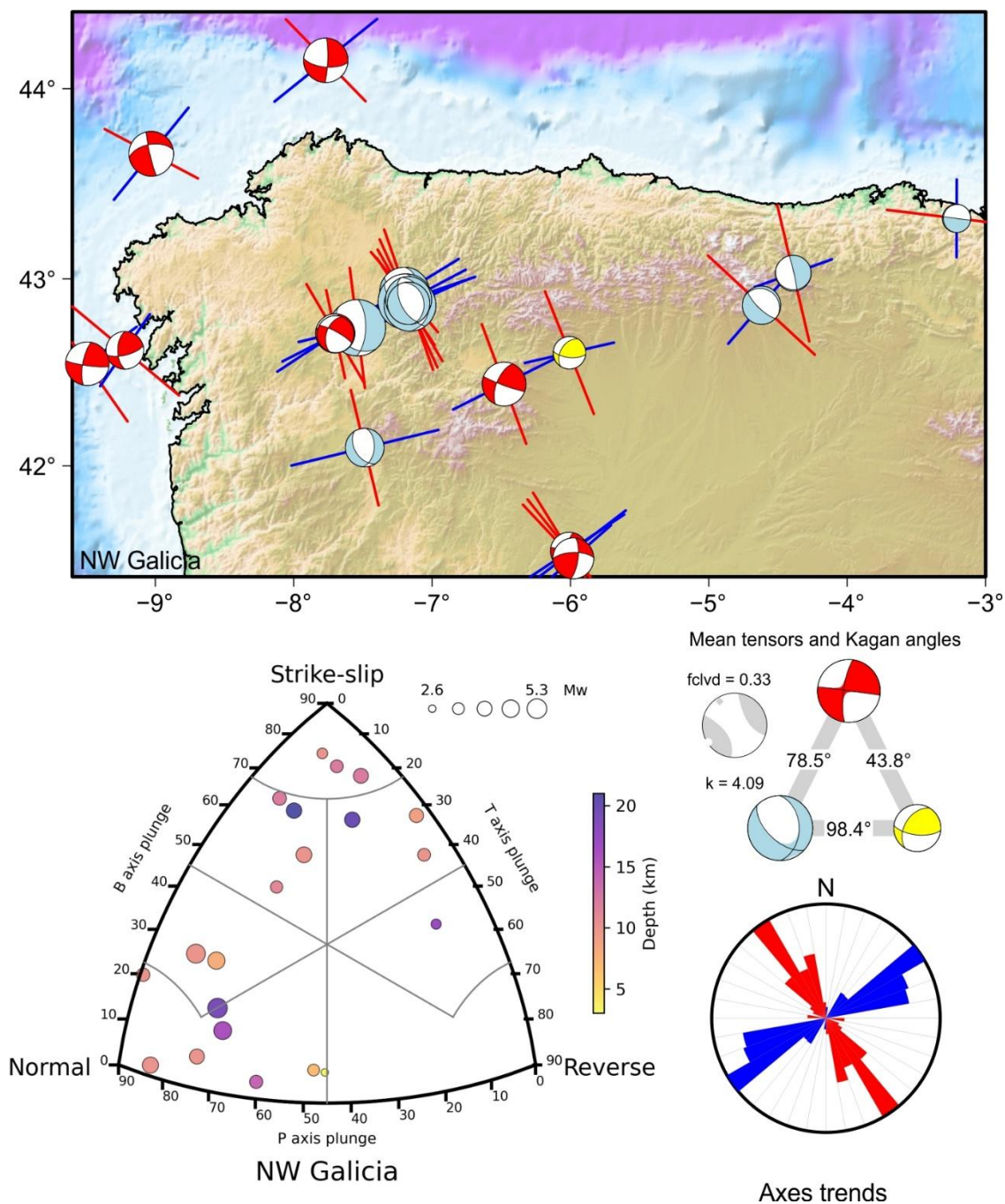
Fig. A15: NW Galicia tectonic zone. Top map: focal mechanisms with maximum horizontal axis (P or B for normal ruptures) and minimum horizontal axis (T or B for reverse ruptures) orientation. Bottom left classification diagram for earthquake rupture types. Middle right: Average tensors (complete in gray) and Kagan angles between the average tensors for each rupture type. Bottom right: Rose diagram of maximum and minimum horizontal axes orientation.

Fig. A16: Offshore Atlantic tectonic zone. Top map: focal mechanisms with maximum horizontal axis (P or B for normal ruptures) and minimum horizontal axis (T or B for reverse ruptures) orientation. Bottom left classification diagram for earthquake rupture types. Middle right: Average tensors (complete in gray) and Kagan angles between the average tensors for each rupture type. Bottom right: Rose diagram of maximum and minimum horizontal axes orientation.

1250
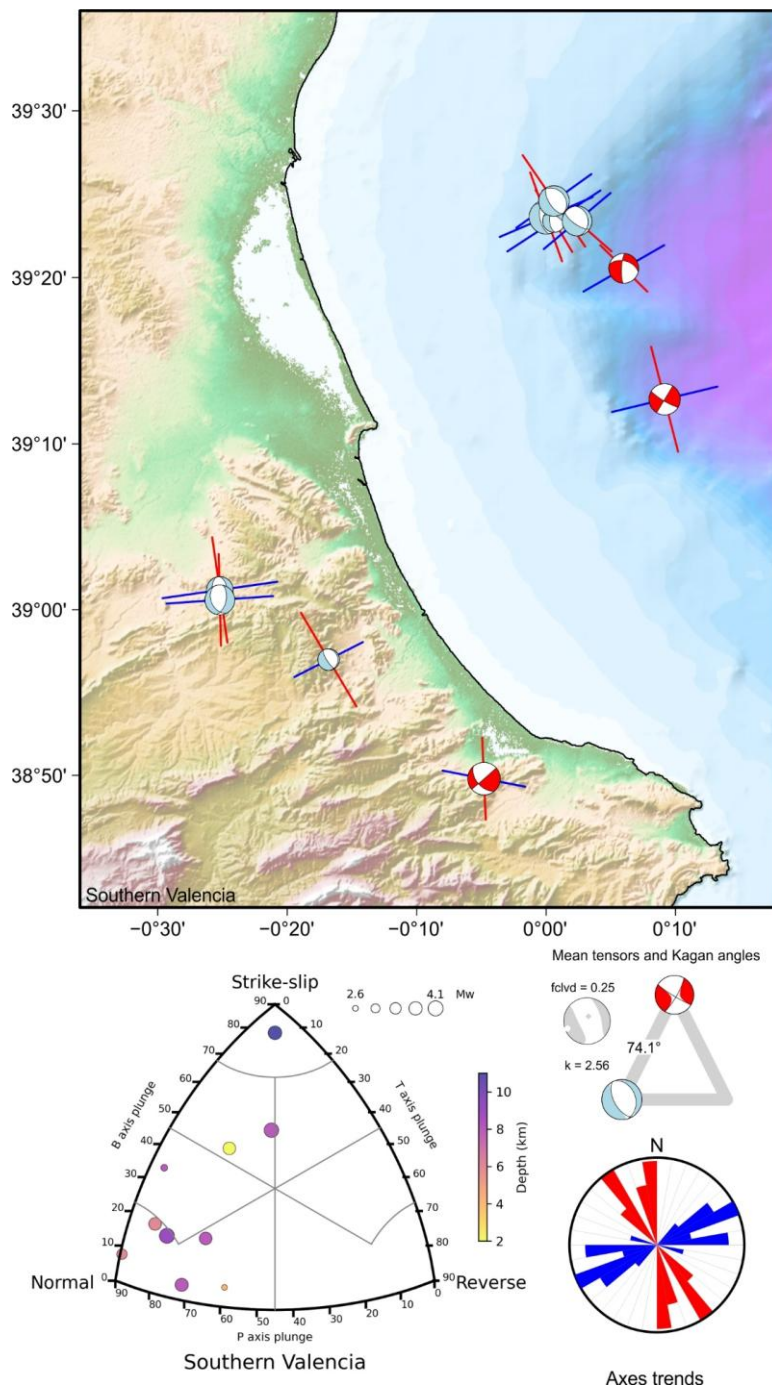
Fig. A17: Southern Valencia tectonic zone. Top map: focal mechanisms with maximum horizontal axis (P or B for normal ruptures) and minimum horizontal axis (T or B for reverse ruptures) orientation. Bottom left classification diagram for earthquake rupture types. Middle right: Average tensors (complete in gray) and Kagan angles between the average tensors for each rupture type. Bottom right: Rose diagram of maximum and minimum horizontal axes orientation.

1255

Fig. A18: Western Alcaraz Arch tectonic zone. Top map: focal mechanisms with maximum horizontal axis (P or B for normal ruptures) and minimum horizontal axis (T or B for reverse ruptures) orientation. Bottom left classification diagram for earthquake rupture types. Middle right: Average tensors (complete in gray) and Kagan angles between the average tensors for each rupture type. Bottom right: Rose diagram of maximum and minimum horizontal axes orientation.
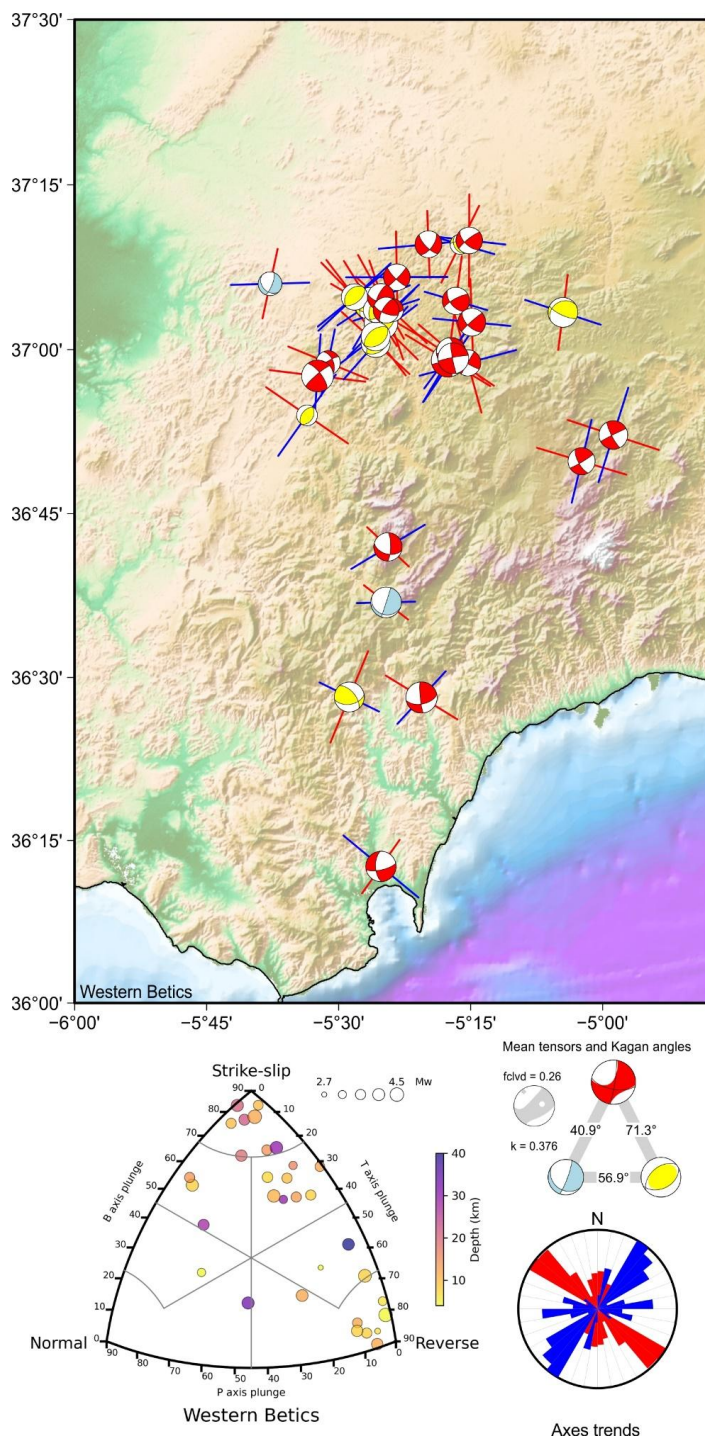
Fig. A19: Western Betics tectonic zone. Top map: focal mechanisms with maximum horizontal axis (P or B for normal ruptures) and minimum horizontal axis (T or B for reverse ruptures) orientation. Bottom left classification diagram for earthquake rupture types. Middle right: Average tensors (complete in gray) and Kagan angles between the average tensors for each rupture type. Bottom right: Rose diagram of maximum and minimum horizontal axes orientation.
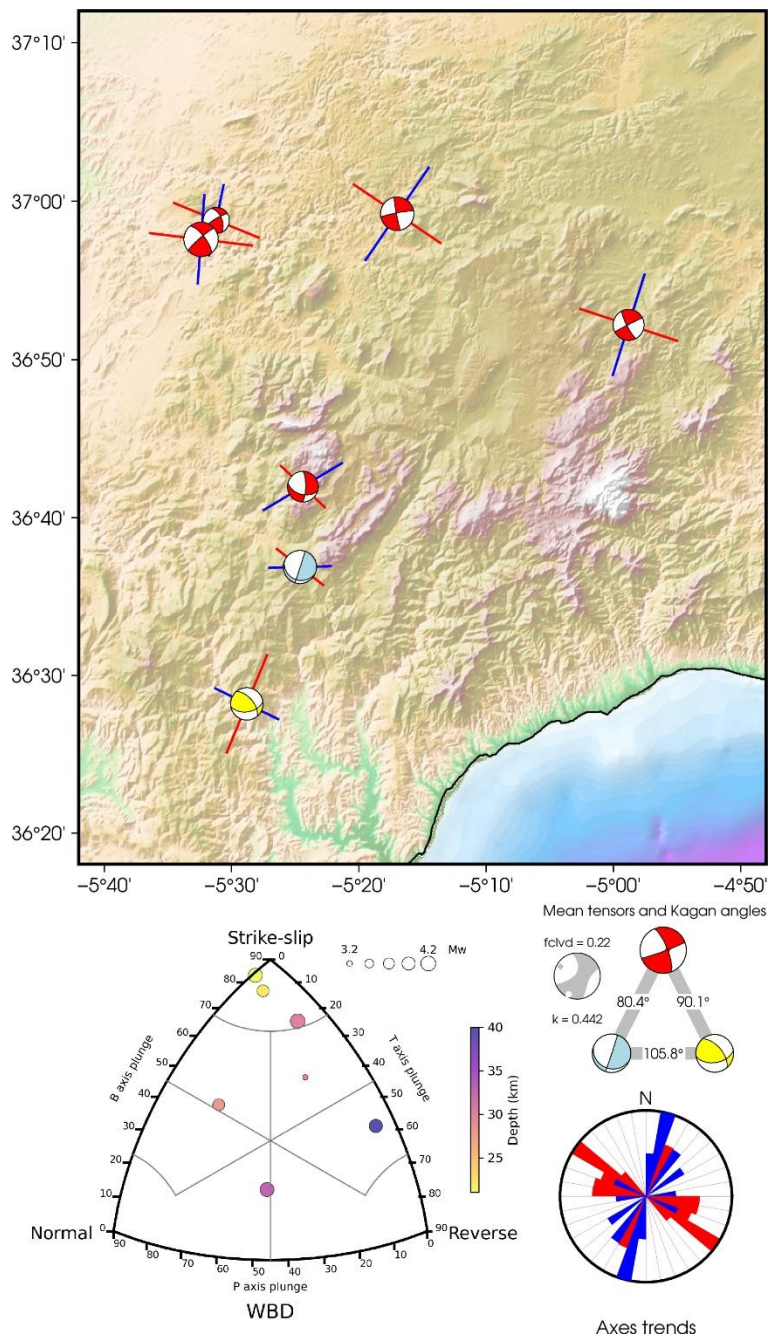
Fig. A20 Western Betics >20 km tectonic zone. Top map: focal mechanisms with maximum horizontal axis (P or B for normal ruptures) and minimum horizontal axis (T or B for reverse ruptures) orientation. Bottom left classification diagram for earthquake rupture types. Middle right: Average tensors (complete in gray) and Kagan angles between the average tensors for each rupture type. Bottom right: Rose diagram of maximum and minimum horizontal axes orientation.
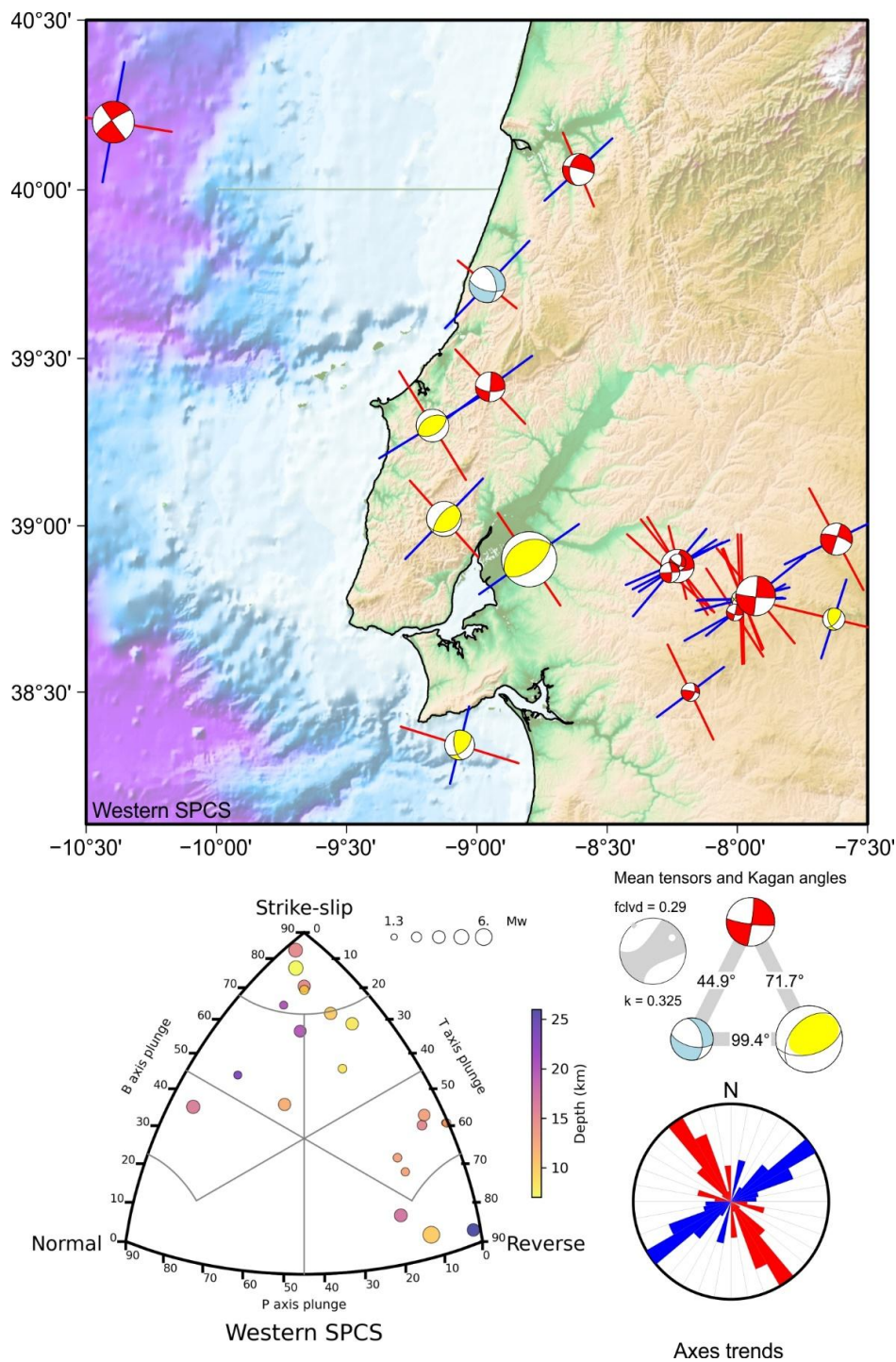
Fig. A21: Western Spanish Portugues Central System tectonic zone. Top map: focal mechanisms with maximum horizontal axis (P or B for normal ruptures) and minimum horizontal axis (T or B for reverse ruptures) orientation. Bottom left classification diagram for earthquake rupture types. Middle right: Average tensors (complete in gray) and Kagan angles between the average tensors for each rupture type. Bottom right: Rose diagram of maximum and minimum horizontal axes orientation.
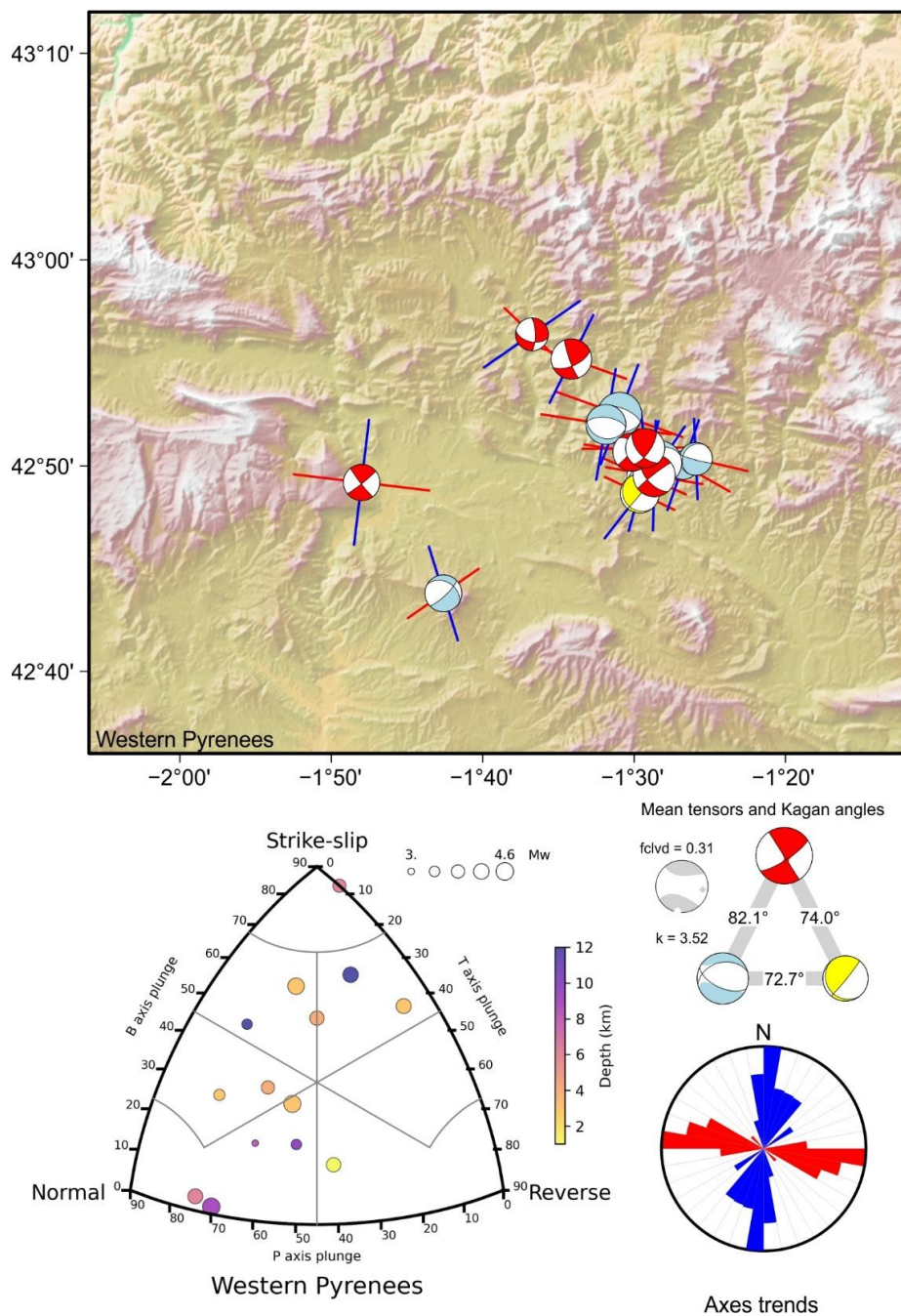
Fig. A22: Western Pyrenees tectonic zone. Top map: focal mechanisms with maximum horizontal axis (P or B for normal ruptures) and minimum horizontal axis (T or B for reverse ruptures) orientation. Bottom left classification diagram for earthquake rupture types. Middle right: Average tensors (complete in gray) and Kagan angles between the average tensors for each rupture type. Bottom right: Rose diagram of maximum and minimum horizontal axes orientation.
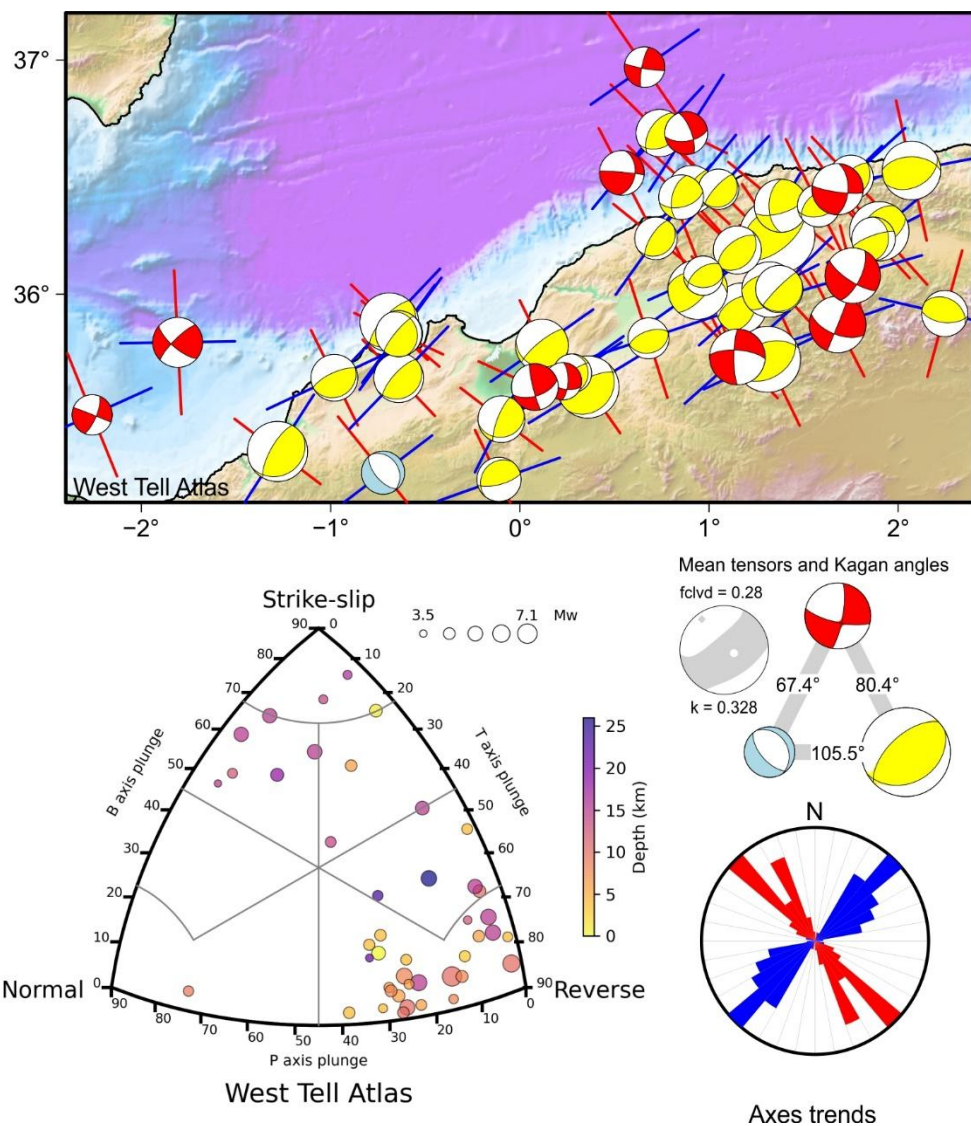
Fig. A23: West Tell Atlas tectonic zone. Top map: focal mechanisms with maximum horizontal axis (P or B for normal ruptures) and minimum horizontal axis (T or B for reverse ruptures) orientation. Bottom left classification diagram for earthquake rupture types. Middle right: Average tensors (complete in gray) and Kagan angles between the average tensors for each rupture type. Bottom right: Rose diagram of maximum and minimum horizontal axes orientation.

 Fig. A24: Western Valencia tectonic zone. Top map: focal mechanisms with maximum horizontal axis (P or B for normal ruptures) and minimum horizontal axis (T or B for reverse ruptures) orientation. Bottom left classification diagram for earthquake rupture types. Middle right: Average tensors (complete in gray) and Kagan angles between the average tensors for each rupture type. Bottom right: Rose diagram of maximum and minimum horizontal axes orientation.

Fig. B1 Al Hoceima tectonic zone. Results of the stress and strain analyses for different zones: a) Right Dihedra solution. b) Rose diagram of the Dey (horizontal shortening direction) obtained from the Slip model. C) Pitch/Dip plot for the neo-formed nodal planes obtained from the Slip Model. d) Stress Inversion Results. e) Variability of the three principal stress axes of the stress inversion. e) Variability of the three principal stress axes of the stress inversion.

1305

1310

1315
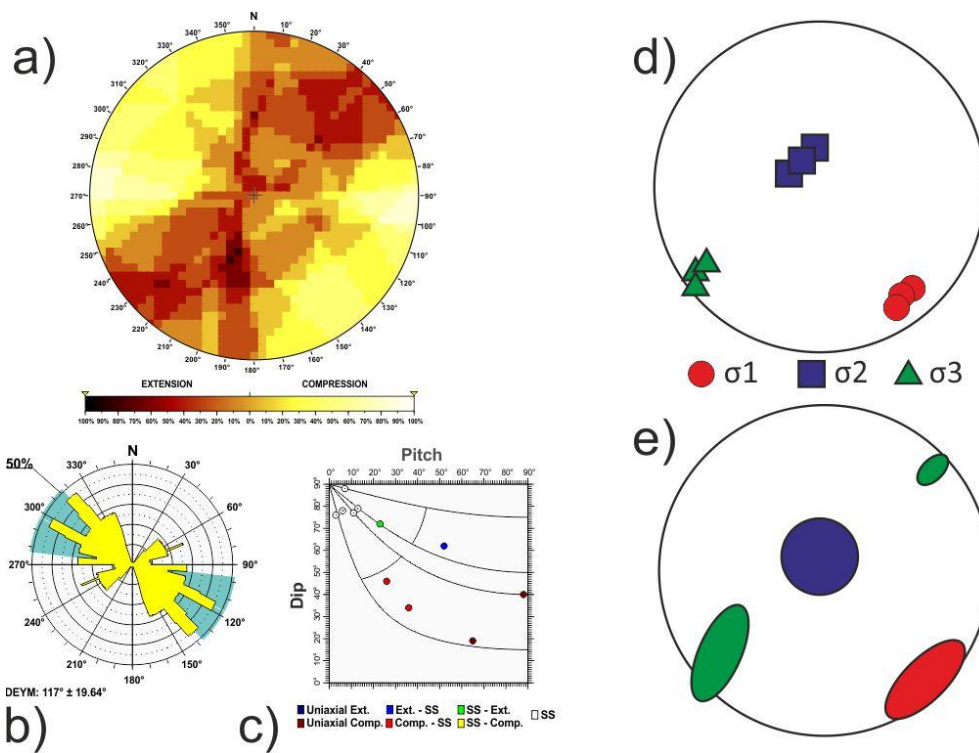
Fig. B2 Algarve tectonic zone. Results of the stress and strain analyses for different zones: a) Right Dihedra solution. b) Rose diagram of the Dey (horizontal shortening direction) obtained from the Slip model. C) Pitch/Dip plot for the neo-formed nodal planes obtained from the Slip Model. d) Stress Inversion Results. e) Variability of the three principal stress axes of the stress inversion.
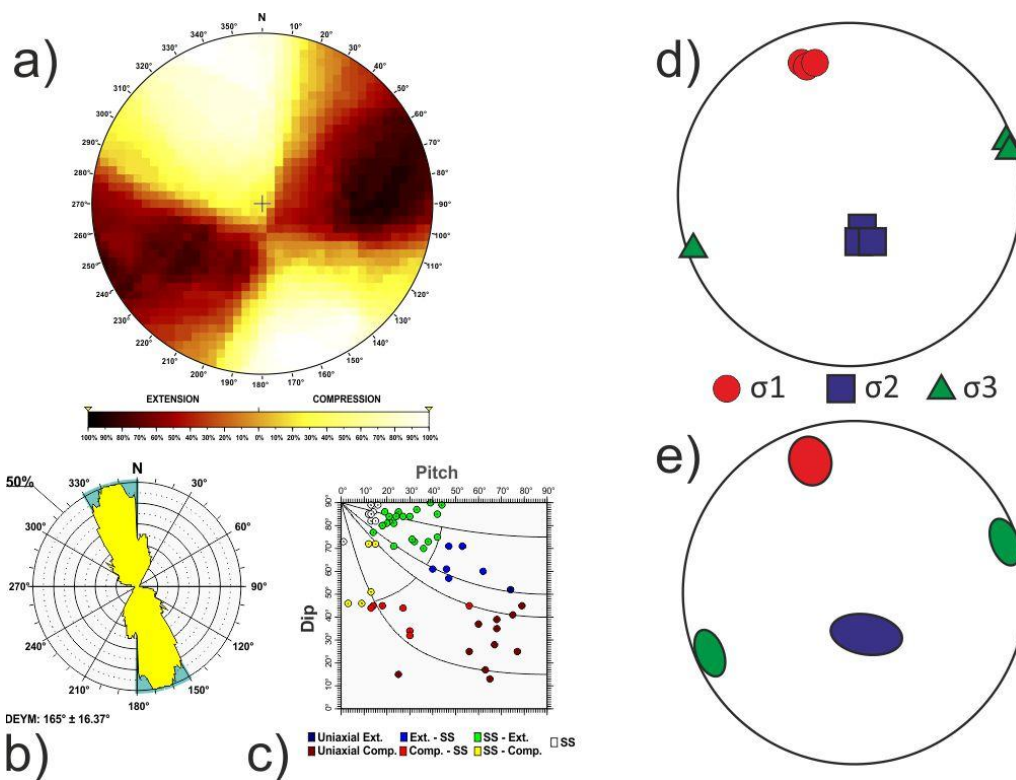
Fig. B3 Alboran Ridge tectonic zone. Results of the stress and strain analyses for different zones: a) Right Dihedra solution. b) Rose diagram of the Dey (horizontal shortening direction) obtained from the Slip model. C) Pitch/Dip plot for the neo-formed nodal planes obtained from the Slip Model. d) Stress Inversion Results. e) Variability of the three principal stress axes of the stress inversion.
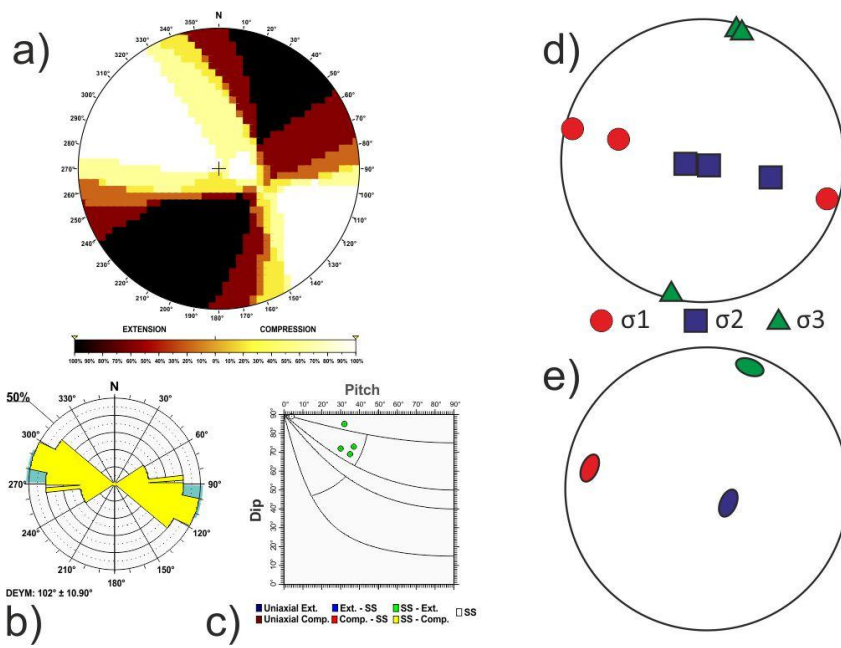
Fig. B4 Betics Antequera tectonic zone. Results of the stress and strain analyses for different zones: a) Right Dihedra solution. b) Rose diagram of the Dey (horizontal shortening direction) obtained from the Slip model. C) Pitch/Dip plot for the neo-formed nodal planes obtained from the Slip Model. d) Stress Inversion Results. e) Variability of the three principal stress axes of the stress inversion.
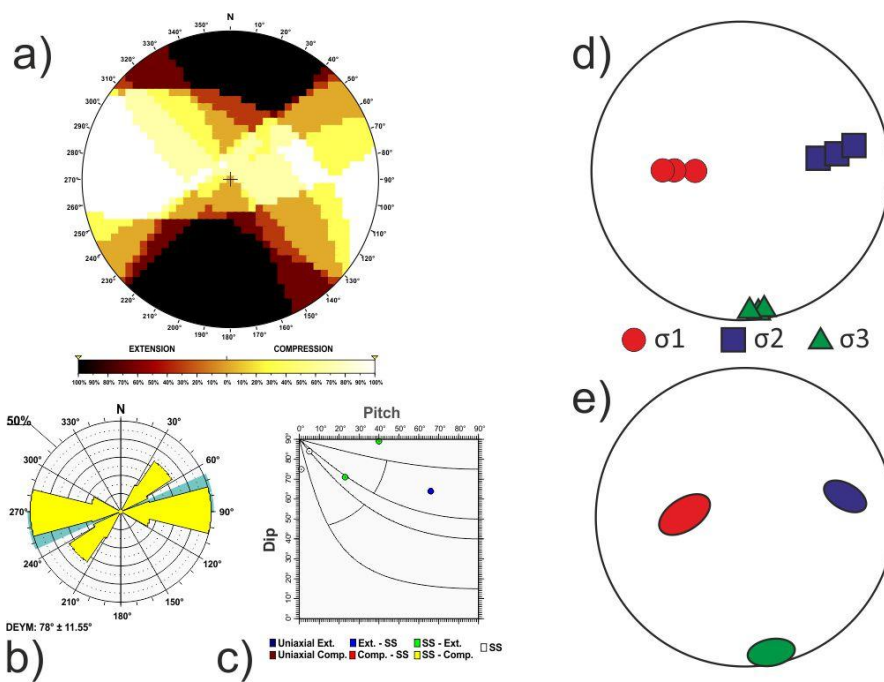
Fig. B5 Central Basins tectonic zone. Results of the stress and strain analyses for different zones: a) Right Dihedra solution. b) Rose diagram of the Dey (horizontal shortening direction) obtained from the Slip model. C) Pitch/Dip plot for the neo-formed nodal planes obtained from the Slip Model. d) Stress Inversion Results. e) Variability of the three principal stress axes of the stress inversion.

1365

1370
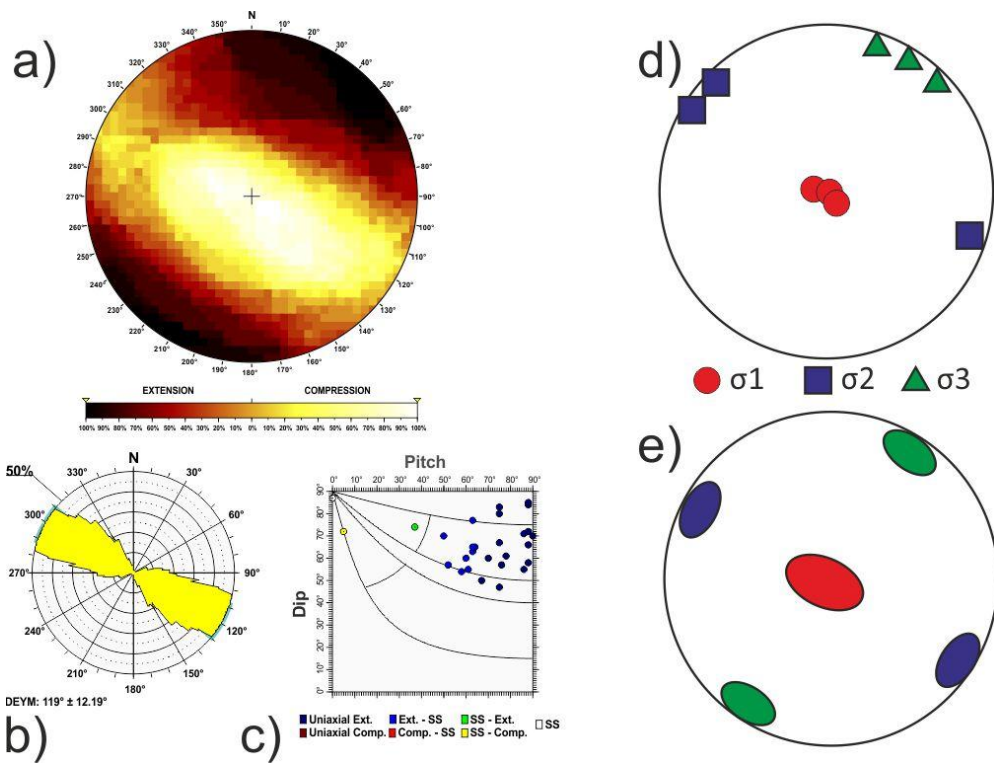
Fig. B6 Central Pyrenees tectonic zone. Results of the stress and strain analyses for different zones: a) Right Dihedra solution. b) Rose diagram of the Dey (horizontal shortening direction) obtained from the Slip model. C) Pitch/Dip plot for the neo-formed nodal planes obtained from the Slip Model. d) Stress Inversion Results. e) Variability of the three principal stress axes of the stress inversion.

Fig. B7 Eastern Betics tectonic zone. Results of the stress and strain analyses for different zones: a) Right Dihedra solution. b) Rose diagram of the Dey (horizontal shortening direction) obtained from the Slip model. C) Pitch/Dip plot for the neo-formed nodal planes obtained from the Slip Model. d) Stress Inversion Results. e) Variability of the three principal stress axes of the stress inversion.

1390

1395
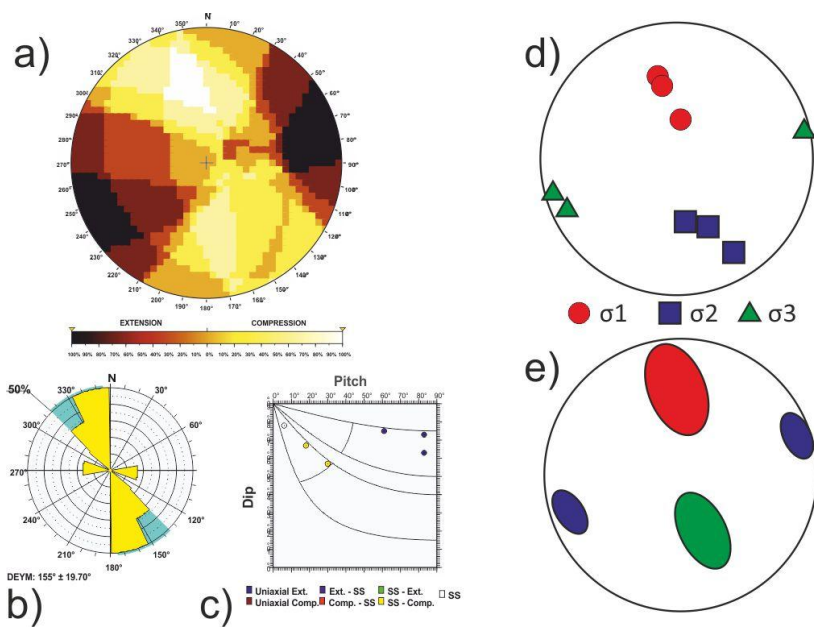
 Fig. B8 Eastern Pyrenees tectonic zone. Results of the stress and strain analyses for different zones: a) Right Dihedra solution. b) Rose diagram of the Dey (horizontal shortening direction) obtained from the Slip model. C) Pitch/Dip plot for the neo-formed nodal planes obtained from the Slip Model. d) Stress Inversion Results. e) Variability of the three principal stress axes of the stress inversion.

Fig. B9 East Tell Atlas tectonic zone. Results of the stress and strain analyses for different zones: a) Right Dihedra solution. b) Rose diagram of the Dey (horizontal shortening direction) obtained from the Slip model. C) Pitch/Dip plot for the neo-formed nodal planes obtained from the Slip Model. d) Stress Inversion Results. e) Variability of the three principal stress axes of the stress inversion.
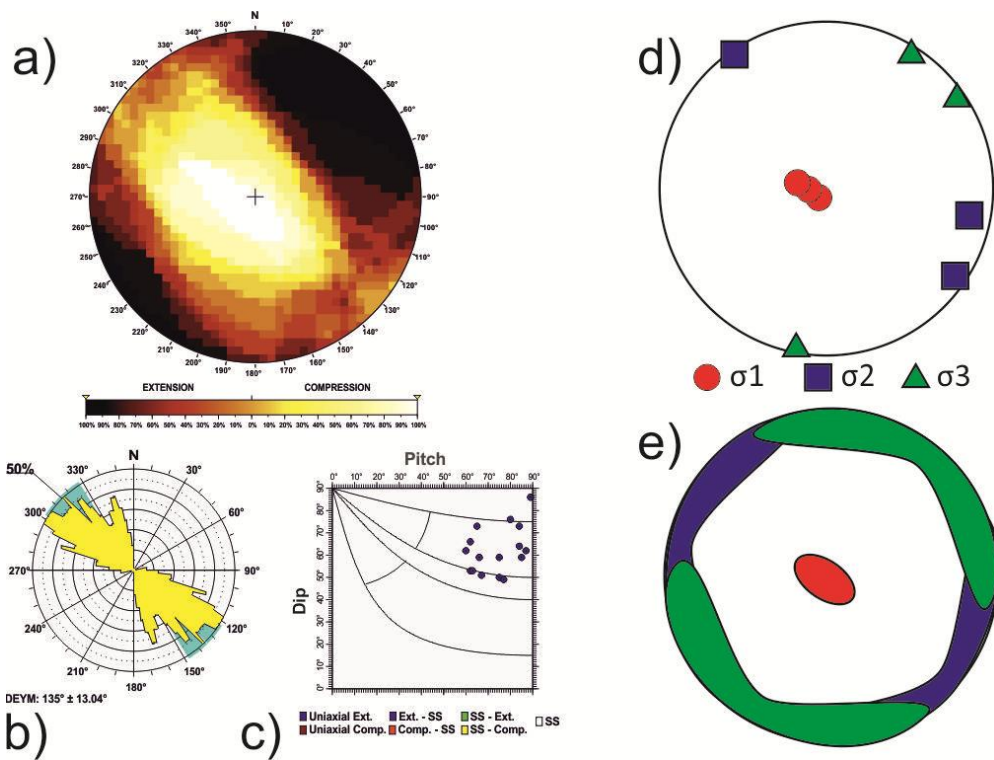
Fig. B10 Granada Basin tectonic zone. Results of the stress and strain analyses for different zones: a) Right Dihedra solution. b) Rose diagram of the Dey (horizontal shortening direction) obtained from the Slip model. C) Pitch/Dip plot for the neo-formed nodal planes obtained from the Slip Model. d) Stress Inversion Results. e) Variability of the three principal stress axes of the stress inversion.

1425

1430
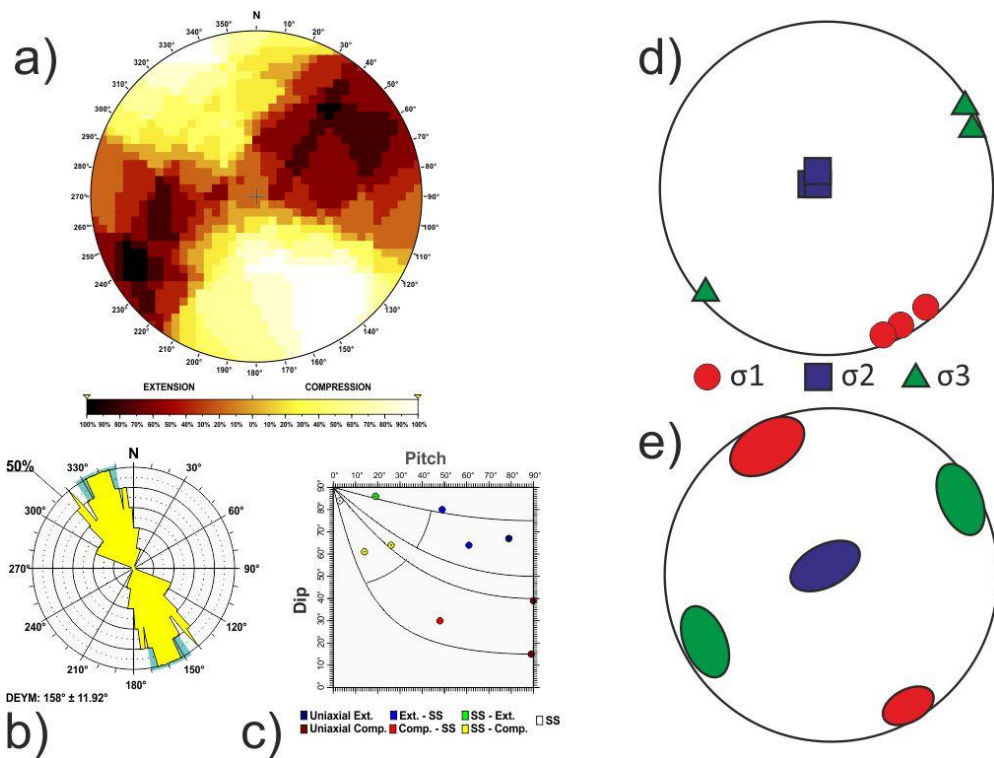
1435   **Fig. B11 Gulf of Cádiz tectonic zone. Results of the stress and strain analyses for different zones: a) Right Dihedra solution. b) Rose diagram of the Dey (horizontal shortening direction) obtained from the Slip model. C) Pitch/Dip plot for the neo-formed nodal planes obtained from the Slip Model. d) Stress Inversion Results. e) Variability of the three principal stress axes of the stress inversion.**

1440

1445
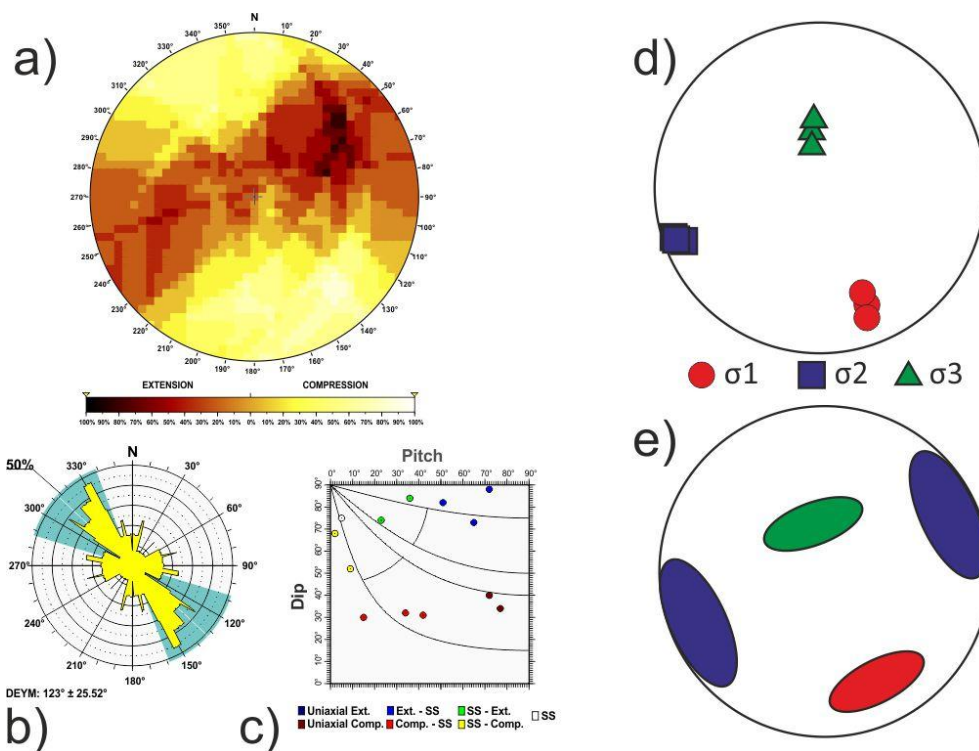
1450   **Fig. B12 Gorringe - Horseshoe tectonic zone. Results of the stress and strain analyses for different zones: a) Right Dihedra solution. b) Rose diagram of the Dey (horizontal shortening direction) obtained from the Slip model. C) Pitch/Dip plot for the neo-formed nodal planes obtained from the Slip Model. d) Stress Inversion Results. e) Variability of the three principal stress axes of the stress inversion.**

1455

1460

1465

Fig. B13 Iberian Chain tectonic zone. Results of the stress and strain analyses for different zones: a) Right Dihedra solution. b) Rose diagram of the Dey (horizontal shortening direction) obtained from the Slip model. C) Pitch/Dip plot for the neo-formed nodal planes obtained from the Slip Model. d) Stress Inversion Results. e) Variability of the three principal stress axes of the stress inversion.

1470

1475

Fig. B14 Northern Alboran tectonic zone. Results of the stress and strain analyses for different zones: a) Right Dihedra solution. b) Rose diagram of the Dey (horizontal shortening direction) obtained from the Slip model. C) Pitch/Dip plot for the neo-formed nodal planes obtained from the Slip Model. d) Stress Inversion Results. e) Variability of the three principal stress axes of the stress inversion.
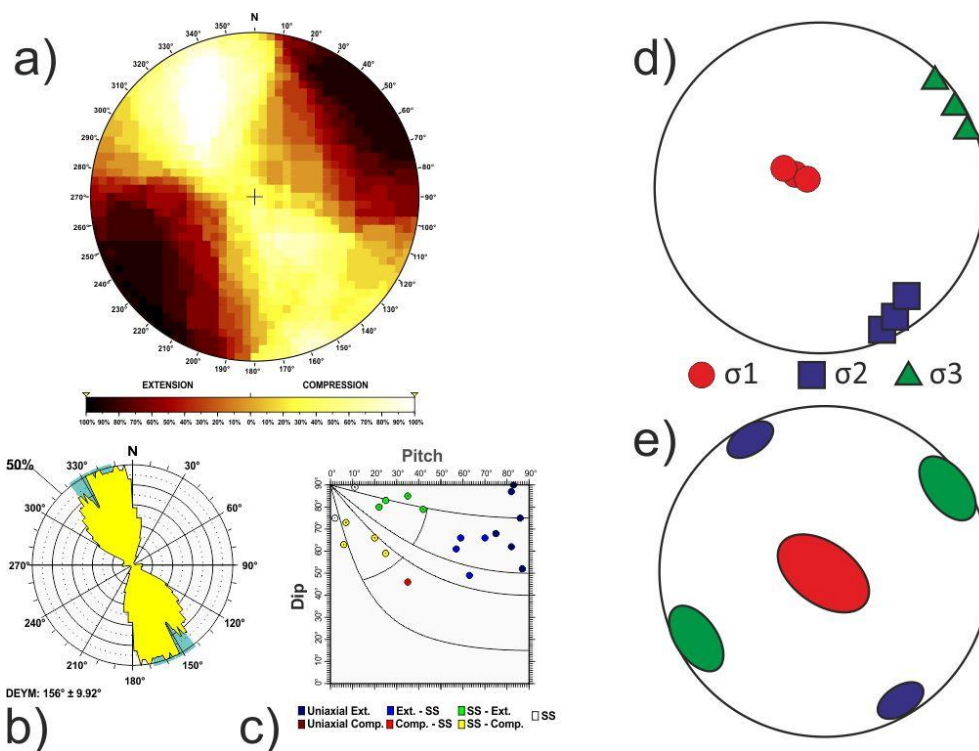
Fig. B15 NW Galicia tectonic zone. Results of the stress and strain analyses for different zones: a) Right Dihedra solution. b) Rose diagram of the Dey (horizontal shortening direction) obtained from the Slip model. C) Pitch/Dip plot for the neo-formed nodal planes obtained from the Slip Model. d) Stress Inversion Results. e) Variability of the three principal stress axes of the stress inversion.
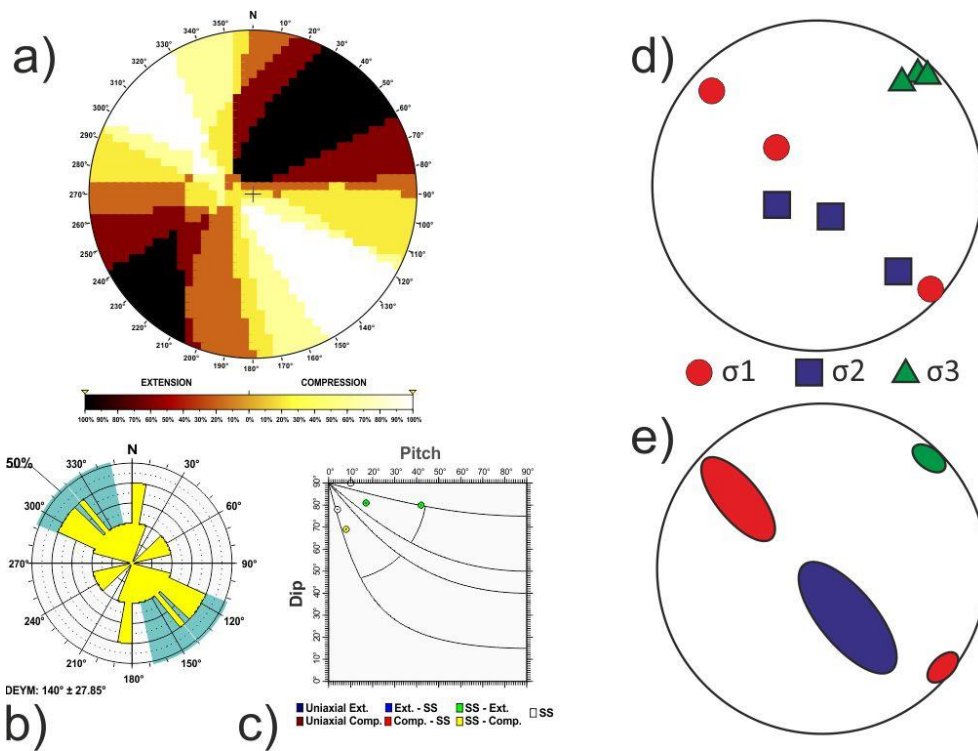
Fig. B16 Offshore Atlantic tectonic zone. Results of the stress and strain analyses for different zones: a) Right Dihedra solution. b) Rose diagram of the Dey (horizontal shortening direction) obtained from the Slip model. C) Pitch/Dip plot for the neo-formed nodal planes obtained from the Slip Model. d) Stress Inversion Results. e) Variability of the three principal stress axes of the stress inversion.

1530

1535
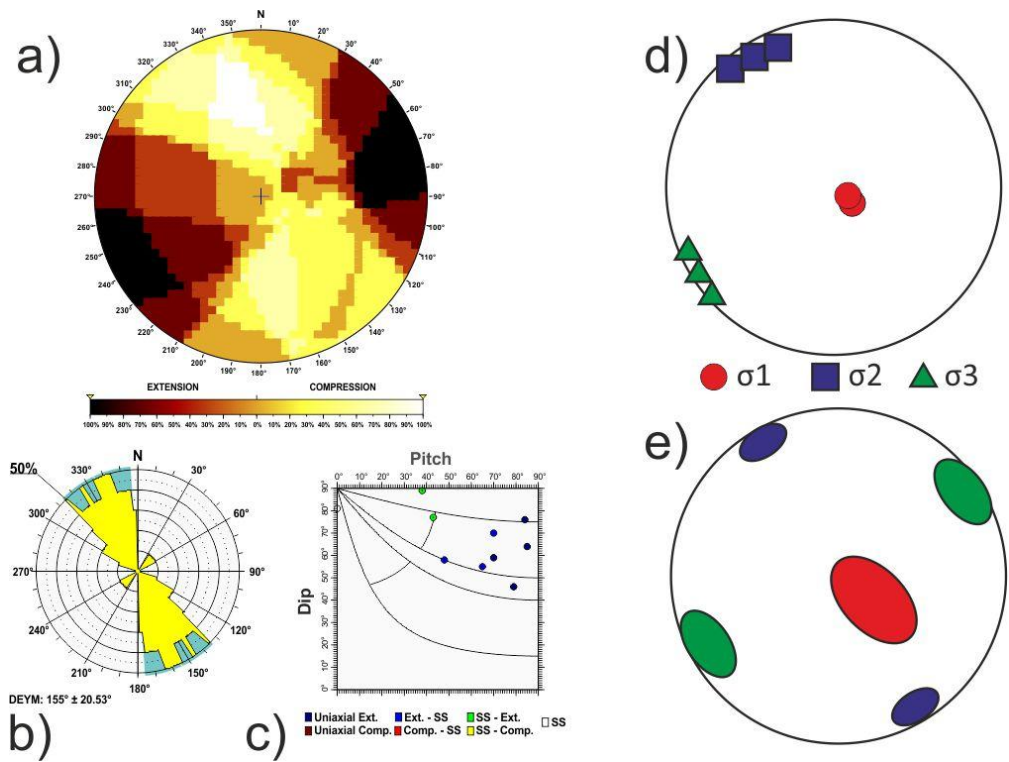
Fig. B17 Southern Valencia tectonic zone. Results of the stress and strain analyses for different zones: a) Right Dihedra solution. b) Rose diagram of the Dey (horizontal shortening direction) obtained from the Slip model. C) Pitch/Dip plot for the neo-formed nodal planes obtained from the Slip Model. d) Stress Inversion Results. e) Variability of the three principal stress axes of the stress inversion.

1545
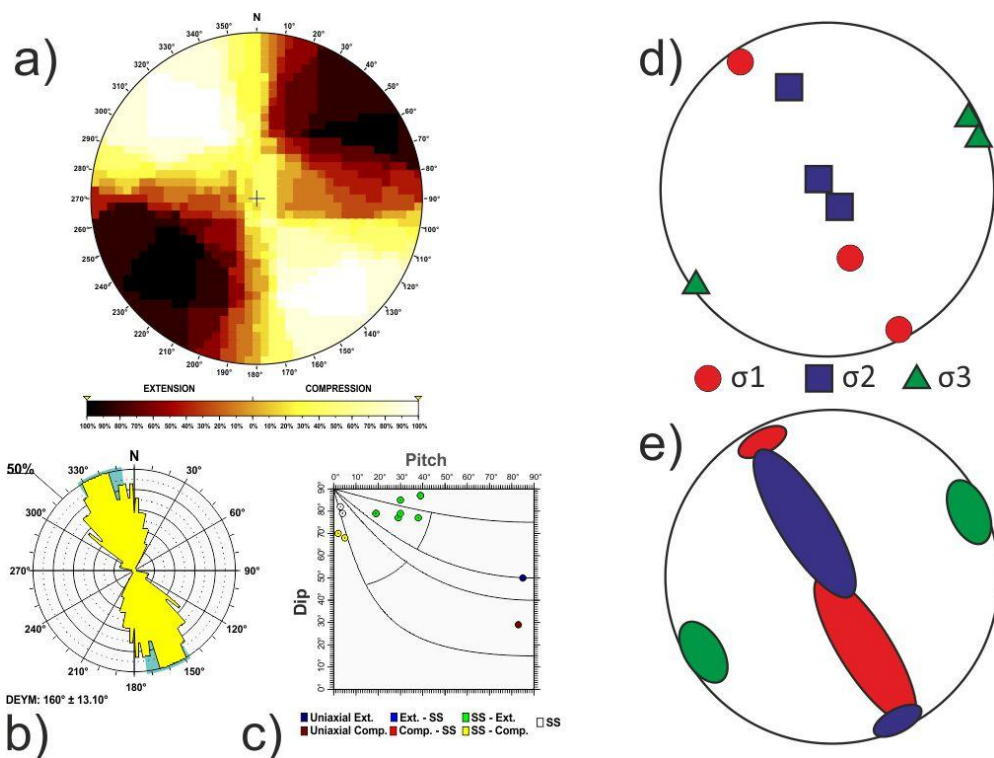
Fig. B18 Western Alcaraz Arch tectonic zone. Results of the stress and strain analyses for different zones: a) Right Dihedra solution. b) Rose diagram of the Dey (horizontal shortening direction) obtained from the Slip model. C) Pitch/Dip plot for the neo-formed nodal planes obtained from the Slip Model. d) Stress Inversion Results. e) Variability of the three principal stress axes of the stress inversion.
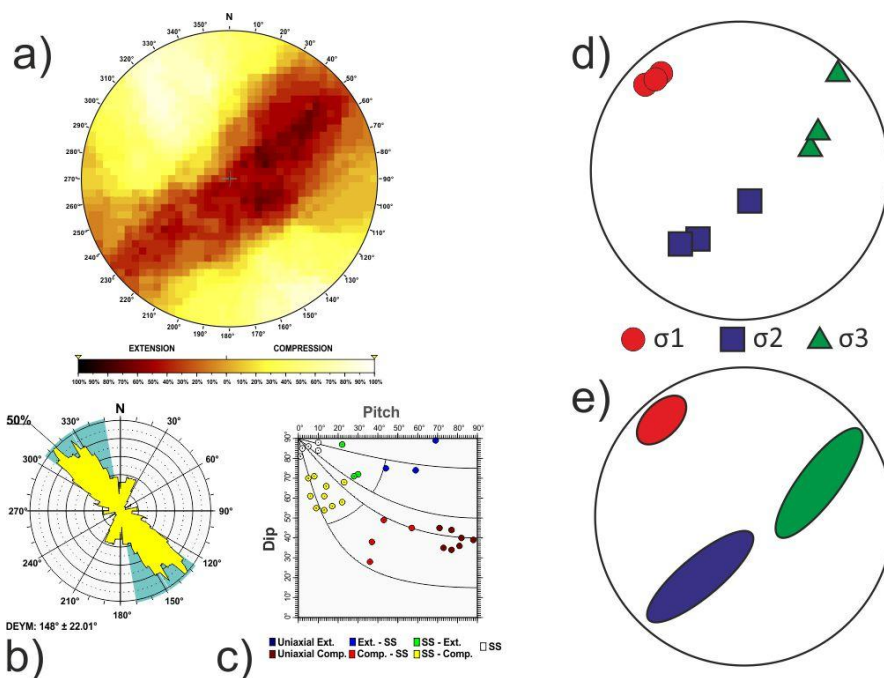
Fig. B19 Western Betics tectonic zone. Results of the stress and strain analyses for different zones: a) Right Dihedra solution. b) Rose diagram of the Dey (horizontal shortening direction) obtained from the Slip model. C) Pitch/Dip plot for the neo-formed nodal planes obtained from the Slip Model. d) Stress Inversion Results. e) Variability of the three principal stress axes of the stress inversion.
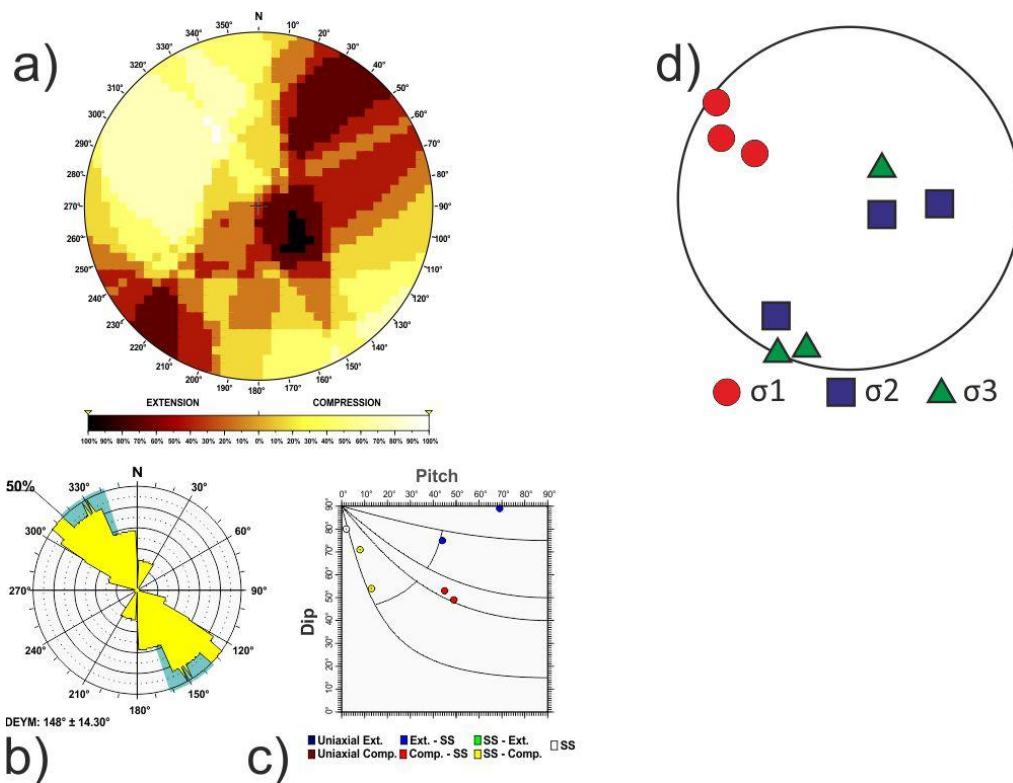
Fig. B20 Western Betics > 20 km tectonic zone. Results of the stress and strain analyses for different zones: a) Right Dihedra solution. b) Rose diagram of the Dey (horizontal shortening direction) obtained from the Slip model. C) Pitch/Dip plot for the neo-formed nodal planes obtained from the Slip Model. d) Stress Inversion Results. e) Variability of the three principal stress axes of the stress inversion.
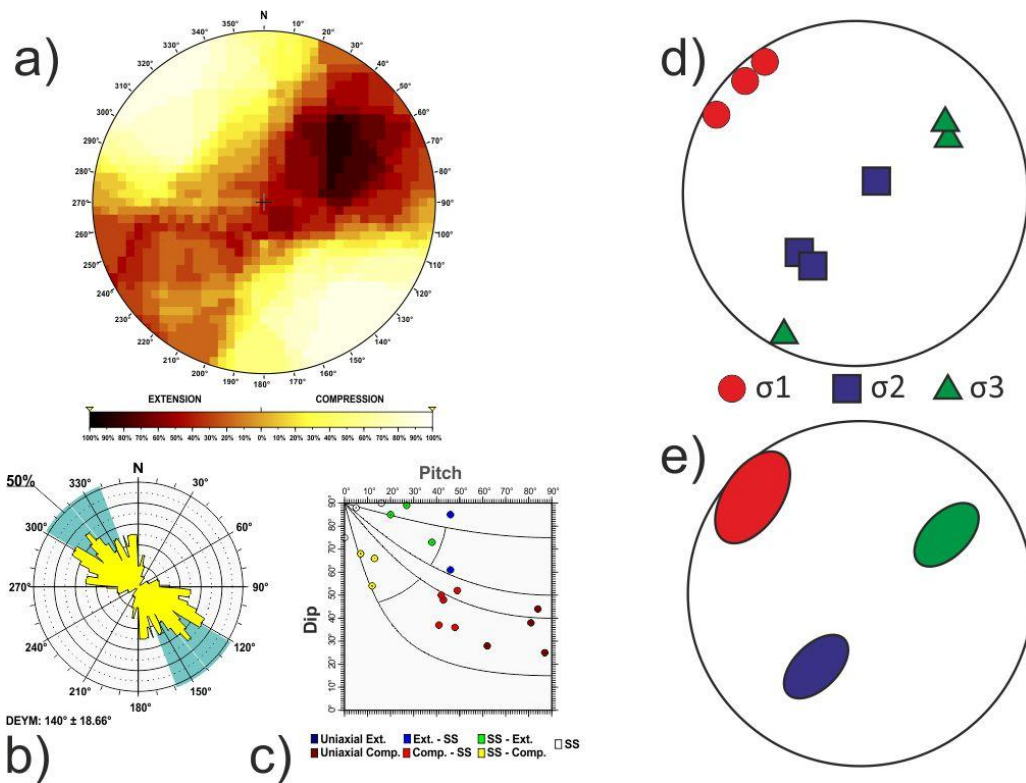
Fig. B21 Western Spanish Portuguese Central System tectonic zone. Results of the stress and strain analyses for different zones: a) Right Dihedra solution. b) Rose diagram of the Dey (horizontal shortening direction) obtained from the Slip model. C) Pitch/Dip plot for the neo-formed nodal planes obtained from the Slip Model. d) Stress Inversion Results. e) Variability of the three principal stress axes of the stress inversion.
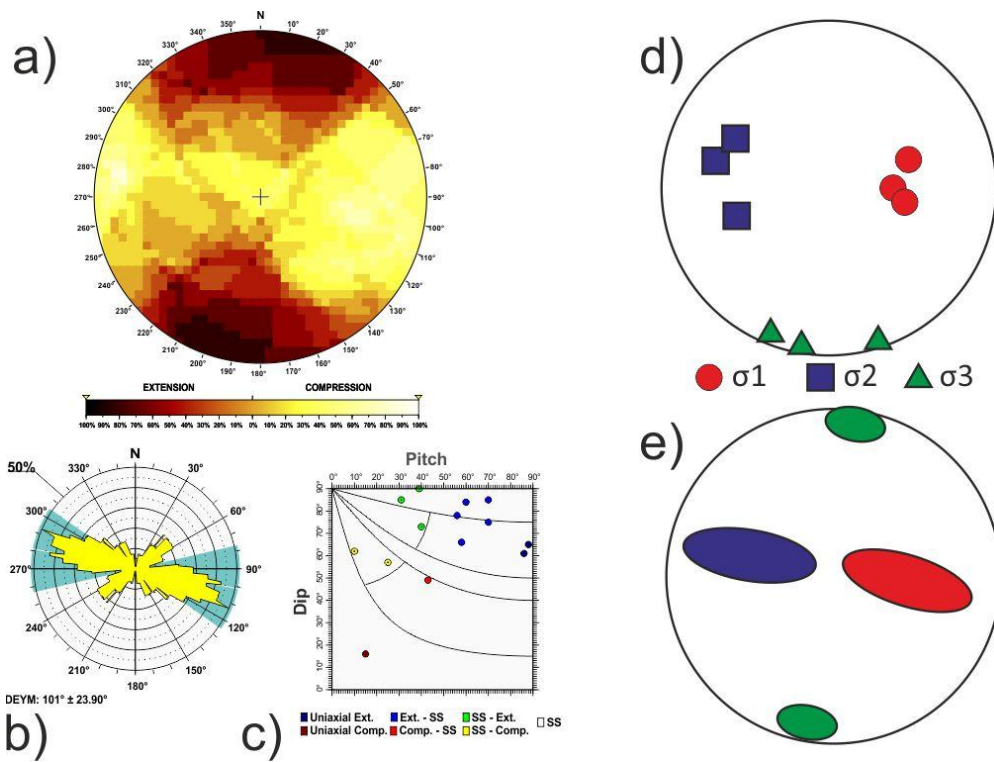
Fig. B22 Western Pyrenees tectonic zone. Results of the stress and strain analyses for different zones: a) Right Dihedra solution. b) Rose diagram of the Dey (horizontal shortening direction) obtained from the Slip model. C) Pitch/Dip plot for the neo-formed nodal planes obtained from the Slip Model. d) Stress Inversion Results. e) Variability of the three principal stress axes of the stress inversion.
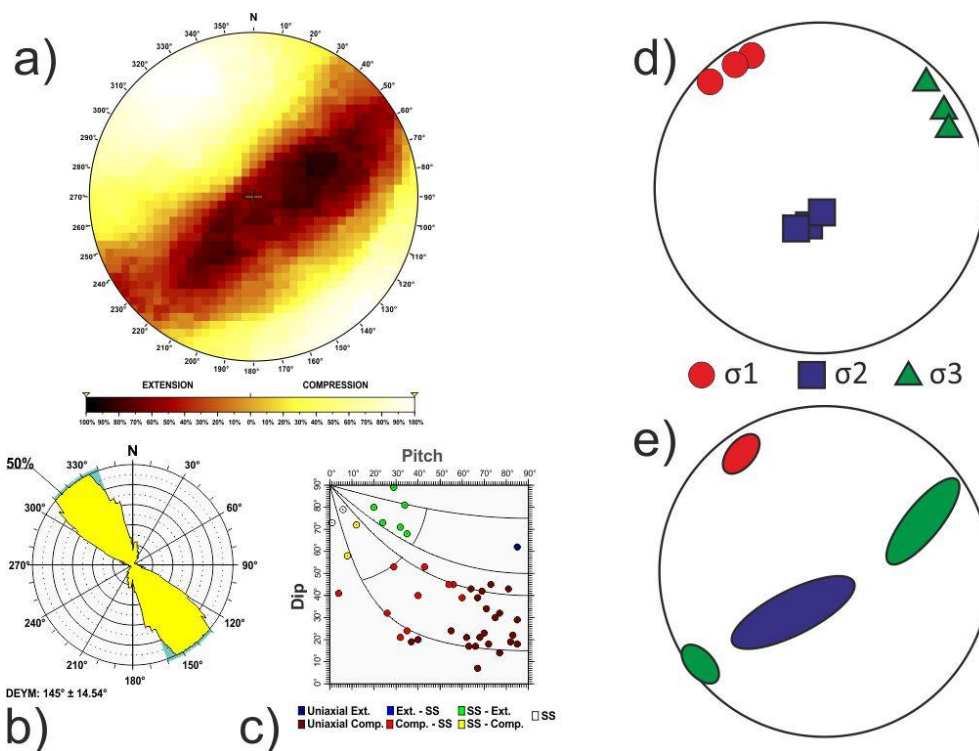
1600 Fig. B23 West Tell Atlas tectonic zone. Results of the stress and strain analyses for different zones: a) Right Dihedra solution. b) Rose diagram of the Dey (horizontal shortening direction) obtained from the Slip model. C) Pitch/Dip plot for the neo-formed nodal planes obtained from the Slip Model. d) Stress Inversion Results. e) Variability of the three principal stress axes of the stress inversion.

1605

1610

1615

Fig. B24 Western Valencia tectonic zone. Results of the stress and strain analyses for different zones: a) Right Dihedra solution. b) Rose diagram of the Dey (horizontal shortening direction) obtained from the Slip model. C) Pitch/Dip plot for the neo-formed nodal planes obtained from the Slip Model. d) Stress Inversion Results. e) Variability of the three principal stress axes of the stress inversion.

Data availability

Focal mechanisms used in this study are compiled from: Braunmiller et al., 2002; Carreño et al., 2008; Cesca et al., 2021; Chevrot et al., 2011; Custodio et al., 2016; Del Pie Perales, 2016; Dziewonski et al., 1981; Ekström et al., 2012; ETH-Swiss Seismological Service; GFZ-Postdam; Global Centroid Moment Tensor; IAG Instituto Andaluz de Geofísica; IGN Instituto Geográfico Nacional de España; IPMA Portuguese Institute for Sea and Atmosphere; INGV Istituto Nazionale di Geofisica e Vulcanologia; Martín et al., 2015; Matos et al., 2018; Olaiz et al.2024; Pondrelli et al., 2002, 2004; Rueda and Mezcua, 2005; Scognamiglio et al., 2006; Stich et al., 2003, 2005, 2006, 2010, 2020 and Villaseñor et al., 2020.

Supplementary material includes the focal mechanism compiled and the new focal mechanism calculated for this study. The database is available at a Zenodo repository (https://doi.org/10.5281/zenodo.14326528). A database encompassing both the results of this study and previous data from World Stress Map, standardized in accordance with World Stress Map guidelines is accessible at https://doi.org/10.5281/zenodo.14326528.

Author contribution

AO, JAAG, GDV, AMM conceived the idea. AO, JAAG, GDV, AMM, JVC, SC, DV and OH performed the formal analysis, investigation and methodology. JVC and DN calculated the new focal mechanisms. AO, JAAG, GDV, AMM, SC and OH completed the supervision and visualization of the manuscript. AO and OH worked on data curation. AO, JAAG, GDV, AMM, OH prepared the original manuscript; all the authors contributed to the review and editing. JAAG and AMM worked on funding acquisition.

Competing interest

The contact author has declared that none of the authors has any competing interests

Acknowledgements

The Generic Mapping Tools (GMT) were used for figure plotting (Wessel and Smith, 1995). The authors would like to express their sincere appreciation to Dr. Antonio Casas, Prof. Klaus Reicherter, an anonymous reviewer and the editor Dr. von Hagke for their insightful comments and constructive suggestions, which have greatly improved the quality of this manuscript.

Financial support

1655   The authors acknowledge support from the projects GEOMARHIS (PID2022-138360NB-I00) and model_SHaKER (PID2021-124155NB-C31) funded by the Ministry of Science, Innovation and Universities of Spain. Additional support comes from the Community of Madrid's programme of R&D activities in technologies (TEC-2024/ECO-69 - CARESOIL-CM)

References

Amadei, B., and Stephansson, O.: Rock Stress and its measurements, 1st ed., Chapman and Hall, New York, 9401062471,
1660   1997.

Ammar, A., Mauffret, A., Gorini, C. and Jabour, H.: The tectonic structure of the Alboran Margin of Morocco. Rev. Soc. Geo. España, 20 (3-4): 247-271, ISSN 0214-2708, 2007.

Angelier, J., and Mechler, P.: Sur une méthode graphique de recherche des contraintes principales egalement utilisable en tectonique et en seismologie: La methode des diedres droites, Bull. Soc. Geol. Fr., 7(19), 1309 – 1318,
1665   https://doi.org/10.2113/gssgfbull.S7-XIX.6.1309, 1977.

Alasset, P.J. and Meghraoui, M.: Active faulting in the western Pyrénées (France): Paleoseismic evidence for late Holocene ruptures. Tectonophysics 409 (2005) 39 – 54, https://doi.org/10.1016/j.tecto.2005.08.019, 2005

Alvarez-Gómez, J.A.: FMC—earthquake focal mechanisms data management, cluster and classification. SoftwareX 9, 299–307. https://doi.org/10.1016/j.softx.2019.03.008, 2019.

1670   Álvaro, M., Capote, R. and Vegas, R.: Un modelo de evolución geotectónica para la Cadena Celtibérica. Acta Geologica Hispanica. Homenage a LIuis Sole i Sabaris, 14, 172-177, 1979

Ancochea, E. and Huertas, M.J.: Radiometric ages and time–space distribution of volcanism in the Campo de Calatrava Volcanic Field (Iberian Peninsula). J. Iber. Geol. 47:209–223 https://doi.org/10.1007/s41513-021-00167-y, 2021.

Arcila, M. and Muñoz–Martín, A.: Integrated perspective of the present–day stress and strain regime in Colombia from analysis
1675   of earthquake focal mechanisms and geodetic data. In: Gómez, J. & Pinilla–Pachon, A.O. (editors), The Geology of Colombia, Volume 4 Quaternary. Servicio Geológico Colombiano, Publicaciones Geológicas Especiales 38, 21 pp. Bogotá. https://doi.org/10.32685/pub.esp.38.2019.17, 2020.

Arlegui, L.E., Simón, J.L., Lisle, R.J. and Orife, T.: Late Pliocene-Pleistocene stress field in the Teruel and Jiloca grabens (eastern Spain): contribution of a new method of stress inversion. J. Struc. Geol. 27, 693–705,
1680   https://doi.org/10.1016/j.jsg.2004.10.013, 2005.

Asensio, E., Khazaradze, G., Echeverria, A., King, R.W. and Vilajosana, I.: GPS studies of active deformation in the Pyrenees. Geophys. J. Int. 190, 913–921. doi: 10.1111/j.1365-246X.2012.05525.x, 2012.

Bailey, I. W., Alpert, L. A., Becker, T. W., and Miller, M. S.: Co-seismic deformation of deep slabs based on summed CMT data. J. Geophys. Res: Solid Earth, 117(B4), https://doi.org/10.1029/2011JB008943, 2012.

1685   Barcos, L., Balanyá, J.C., Díaz-Azpiroz, M., Expósito, I. and Jiménez-Bonilla, A.: Kinematics of the Torcal Shear Zone: Transpressional tectonics in a salient-recess transition at the northern Gibraltar Arc. Tectonophysics 663- 62-77. http://dx.doi.org/10.1016/j.tecto.2015.05.002, 2015.

Bell, J. S., Caillet, G. and Lemarrec, A.,: The Present-Day Stress Regime of the Southwestern Part of the Aquitaine Basin, France, as Indicated by Oil-Well Data, J. Struc. Geol., 14(8-9), 1019-1032, doi:10.1016/0191-8141(92)90033-S, 1992.

1690   Bolillot, G. and Malod, J.: The North and North-West Spanish continental margin: a review. Rev. Soc. Geol. España, 1, 295-316, 1988.

Borges, J. F., Bezzeghoud, M., Buforn, E., Pro, C., and Fitas, A.: The 1980, 1997 and 1998 Azores earthquakes and some seismo-tectonic implications. Tectonophysics, 435(1-4), 37-54, https://doi.org/10.1016/j.tecto.2007.01.008, 2007.

Braunmiller, J., Kradolfer U., Baer M. and Giardini D. Regional Moment- Tensor inversion in the European-Mediterranean
1695   area. Tectonophysics, 356, 5-22. [Dataset] https://doi.org/10.1016/S0040-1951(02)00374-8, 2002.

Briais, A., Armijo, R., Winter, T., Tapponnier, P. and Herbecq, A.: Morphological evidence for Quaternary normal faulting and seismic hazard in the Eastern Pyrenees. Annales Tectonicae 4(1), 19-42, 1990.

Buforn, E., Bezzeghoud, M., Udías, A., and Pro, C.: Seismic sources on the Iberia-African plate boundary and their tectonic implications. Pure and Applied Geophysics, 161, 623-646, https://doi.org/10.1007/s00024-003-2466-1, 2004.

1700   Busetti, S., Jiao, W. and Reches, Z. Geomechanics of hydraulic fracturing microseismicity: Part 1. Shear, hybrid and tensile events. AAPG Bulletin, v. 98, no. 11, pp. 2439-2457, 2014.Cabral, J.: An example of intraplate neotectonic activity, Vilarica Basin, northeast Portugal. Tectonics, 8, 285–303. https://doi.org/10.1029/TC008i002p00285, 1989.

Cabral, J.: Neotectonics of mainland Portugal: state of the art and future perspectives. Journal of Iberian Geology 38 (1), 71-84 http://dx.doi.org/10.5209/rev_JIGE.2012.v38.n1.39206, 2012.

1705   Cabral, J., Mendesa, V.B., Figueiredo, P., da Silveira, A.B., Pagarete, J., Ribeiro, A., Dias, R. and Ressurreição, R.: Active tectonics in Southern Portugal (SW Iberia) inferred from GPS data. Implications on the regional geodynamics. J. Geodyn., 112, 1-11. http://dx.doi.org/10.1016/j.jog.2017.10.002, 2017.

Cabral, J., Dias, R., Cunha, P.P. and Cabral, M.C.: Quaternary tectonic activity of the São Marcos–Quarteira fault (Algarve, southern Portugal): a case study for the characterization of the active geodynamic setting of SW Iberia. J. Iber. Geol.
1710   https://doi.org/10.1007/s41513-019-00102-2, 2019.

Cabrera, L., Roca, E. and Santanach, P.: Basin formation at the end of a strike-slip fault: the Cerdanya Basin (eastern Pyrenees). Jour. Geol. Soc. London 145, 261-268. doi:10.1144/gsjgs.145.2.0261, 1988.

Cannavò, F. and Palano, M.: Defining geodetic reference frame using Matlab®: PlatEMotion 2.0. Pure and Applied Geophysics, 173(3), 937–944. https://doi.org/10.1007/s00024-015-1112-z, 2016.

1715   Carreño, E., Benito, B., Martínez Solares, J.M., Cabañas, L., Giner, J., Murphy, P., López, C.,Del Fresno, C., Alcalde, J.M., Gaspar-Escribano, J.M., Antón, R., Martínez-Díaz, J., Cesca, S., Izquierdo, A., Sánchez Caballero, J.G., and Expósito, P.: The 7 June mbLg 4.2 Escopete Earthquake: An Event with Significant Ground Motion in a Stable Zone (Central Iberian Peninsula). Seismol. Res. Lett., Volume 79, number 6. 820-829. [Dataset] doi: 10.1785/gssrl.79.6.820, 2008.

Casas-Sainz, A.M. and de Vicente, G.: On the tectonic origin of the iberian topography. Tectonophysics, 465. 31 pp.
1720 https://doi.org/10.1016/j.tecto.2009.01.030, 2009.

Capote, R., de Vicente, G. and González-Casado, J.M.: An application of the slip model of brittle deformation to focal mechanism analysis in three different plate tectonics situations, Tectonophysics, 191, 399 – 409, https://doi.org/10.1016/0040-1951(91)90070-9, 1991.

Cebriá, J.M., López-Ruiz, J., Doblas, M., Martins, L.T. and Munha. J.: Geochemistry of the Early Jurassic Messejana-Plasencia
1725 dyke (Portugal-Spain); Implications on the origin of the Central Atlantic Magmatic Province. J. Petrol., 44 (3), 547-568, 2003.

Cesca, S., Stich, D., Grigoli, F., Vuan, A., López-Comino, J.A., Niemz, P., Blanch, E., Dahm, T. and Ellsworth, W.: Seismicity at the Castor gas reservoir driven by pore pressure diffusion and asperities loading. Nature communications, 12:4783, [Dataset] https://doi.org/10.1038/s41467-021-24949-1, 2021.

Chevrot, S., Sylvander, M. and Delouis, B.: A preliminary catalog of moment tensor for the Pyrenees. Tectonophysics, 510,
1730 239-251. [Dataset] doi:10.1016/j.tecto.2011.07.011, 2011.

Cloetingh, S., Burov, E., Beekman, F., Andeweg, B., Andriessen, P.A.M, García- Castellanos, D., de Vicente, G. and Vegas, R.: Lithospheric folding in Iberia. Tectonics, 2002, 21,5,1041. 26 pp. doi:10.1029/2001TC901031,2002

Comas, M. C., Platt, J. P., Soto, J. I., and Watts, A. B.: The origin and tectonic history of the Alboran Basin: insights from Leg 161 results. In Proceedings of the ocean drilling program scientific results (Vol. 161, pp. 555-580), 1999.

1735 Custodio, S., Lima, V., Vales, D., Cesca, S. and Carrilho, F.: Imaging active faulting in a region of distributed deformation from the joint clustering of focal mechanisms and hypocentres: Application to the Azores–western Mediterranean region. Tectonophysics, 676, 70-89. [Dataset].https://doi.org/10.1016/j.tecto.2016.03.013. 2016.

d'Acremont, E., Gutscher, M.A., Rabaute, A., Mercier de Lépinay, B., Lafosse, M., Poort, J., Ammar, A., Tahayt, A., Le Royc, P., Smit, J., Do Couto, D., Cancouët, R., Prunier, C., Ercilla, G. and Gorini, C.: High-resolution imagery of active faulting
1740 offshore Al Hoceima, Northern Morocco. Tectonophysics 632, 160-166, http://dx.doi.org/10.1016/j.tecto.2014.06.008, 2014.

de Vicente, G. (1988), Análisis poblacional de fallas. El sector de enlace Sistema Central- Cordillera Ibérica, Ph.D. thesis, 317 pp., Univ. Complutense de Madrid, Madrid.

de Vicente, G., Cloetingh, S., Muñoz-Martín, A., Olaiz, A., Stich, D., Vegas, R., Galindo-Zaldívar, J. & Fernández-Lozano, J.: Inversion of moment tensor focal mechanisms for active stresses around the microcontinent Iberia: Tectonic implications,
1745 Tectonics, 27(TC1009), doi:10.1029/2006TC002093, 2008.

de Vicente, G., Cunha, P. P., Muñoz-Martín, A., Cloetingh, S., Olaiz, A., and Vegas, R.: The Spanish-Portuguese Central System: An example of intense intraplate deformation and strain partitioning. Tectonics, 37. https://doi.org/10.1029/2018TC005204, 2018.

de Vicente, G., Cloetingh, S., J. Van Wees, J.D. and Cunha, P.P.: Tectonic classification of Cenozoic Iberian foreland basins.
1750 Tectonophysics, 502 (1-2), 38-61. doi:10.1016/j.tecto.2011.02.007, 2011de Vicente, G., Díez Fernández, R., Cunha, P.P. and Olaiz, A.: Active tectonics (Plio-Quaternary) in the western sector of the Madrid Cenozoic Basin. Iberfault 2022, ISBN:978-84-18321-58-0, 2022.de Vicente, G., Olaiz, A., Muñoz-Martín, A. and Cunha, P.P.: Longest and still longer: The Messejana-

Plasencia dyke and its links with later Alpine deformation belt in Iberia. Tectonophysics, Volume 815, 2021, 229009, ISSN 0040-1951, https://doi.org/10.1016/j.tecto.2021.229009, 2021.

1755   de Vicente, G., Terrinha, P., Carbonell, R., Muñoz-Martín, A. and Olaiz, A.: The Trans-Iberia Central Orogen and aborted subduction. X Simposio sobre el margen Ibérico Atlántico. Bilbao. Abstracts volume 14-16, 2022.

de Vicente, G. and Vegas, R.: Large-scale distributed deformation-controlled topography along the western Africa–Eurasia limit: Tectonic constraints. Tectonophysics, 474(1–2), 124–143. https://doi.org/10.1016/j.tecto.2008.11.026, 2009.de Vicente, G., Vegas, R., Muñoz-Martín, A., Silva, P.G., Andriessen, P., Cloetingh, S., González-Casado, J.M., Van Wees, J.D., Álvarez,

1760   J., Carbó, A., Olaiz, A., Cenozoic thick-skinned deformation and topography evolution of the Spanish Central System *Global and planetary change* 58, 335-381.2007 https://doi.org/10.1016/j.gloplacha.2006.11.042

De Ruig, M.J.: Extensional diapirism in the Eastern Prebetic Foldbelt, Southeastern Spain. In: Jackson, M.P.A., Roberts, D.G., Snelson, S. (Eds.), Salt tectonics: a global perspective. AAPG Memoir 65, 353-367, https://doi.org/10.1306/M65604C17, 1995.

1765   Del Pie Perales, L.: Inversión del momento sísmico para terremotos de la región cantábrica: implicaciones geodinámicas. Master thesis. University of Oviedo. 77 pp [Dataset].https://digibuo.uniovi.es/dspace/bitstream/10651/39062/6/TFM_%20Laura%20Pie%20Perales.pdf, 2016

Delvaux, D., Moeys, R., Stapel, G., Petit, C., Levi, K., Miroshnichenko, A., Ruzhich, V. and San´kov, V.: Paleostress reconstructions and geodynamics of the Baikal region, Central Asia, Part 2. Cenozoic rifting. Tectonophysics 282, 1-38.

1770   https://doi.org/10.1016/S0040-1951(97)00210-2, 1997.

Diaz, J., Gallar, J. and Carbonell, R.: Moho topography beneath the Iberian-Western Mediterranean region mapped from controlled-source and natural seismicity surveys. Tectonophysics 692A, 74-85. doi: 10.1016/j.tecto.2016.08.023, 2016.

Domingues, A., Custódio, S. and Cesca, S.: Waveform inversion of small-to-moderate earthquakes offshore southwest Iberia. Geophys. J. Int, Vol 192, Issue 1, January, 2013, Pages 248–259, https://doi.org/10.1093/gji/ggs010, 2013.

1775   Dziewonski, A.M., Chou, T.A. and Woodhouse, J.H.: Determination of earthquake source parameters from waveform data for studies of global and regional seismicity, J. Geophys. Res., 86, 2825-2852. [Dataset]. doi:10.1029/JB086iB04p02825, 1981.

Ercilla, G., Galindo-Zaldívar, J., Estrada, F., Valencia, J., Juan, C., Casas, D., Alonso, B., Mª. Comas, M.C., Tendero-Salmerón, V., Casalbore, D., Azpiroz-Zabala, M., Bárcenas, P., Ceramicola, S., Chiocci, F.L., Idárraga-García, J., López-González, N., Mata, P., Palomino, D., Rodríguez-García, J.A., Teixeira, M., Nespereira, J., Vázquez, J.T. and Yenes, M.

1780   Understanding the complex geomorphology of a deep sea area affected by continental tectonic indentation: The case of the Gulf of Vera (Western Mediterranean). Geomorphology 402 108126 https://doi.org/10.1016/j.geomorph.2022.108126, 2022.

Etheve, N., Mohn, G., Frizon de Lamotte, D., Roca, E., Tugend, J. and Gómez-Romeu, J.: Extreme Mesozoic crustal thinning in the eastern Iberia margin: The example of the Columbrets Basin (Valencia Trough). Tectonics, 37. https://doi.org/10.1002/2017TC004613, 2018.

1785   Etchecopar, A., Vasseur, G., and Daignieres, M.: An inverse problem in microtectonics for the determination of stress tensors from fault striation analysis. J. Struct. Geol., vol.3, no 1, pp 51-65. https://doi.org/10.1016/0191-8141(81)90056-0, 1981.

Ekström, G., Nettles, M. and Dziewonski, A.M.: The global CMT project 2004-2010: Centroid-moment tensors for 13,017 earthquakes, Phys. Earth Planet. Inter., 200-201, 1-9. [Dataset]. doi:10.1016/j.pepi.2012.04.002, 2012.

ETH- Swiss Seismological Service [Dataset] https://geophysics.ethz.ch/research/groups/sed.html

1790   Faccenna, C., Piromallo, C., Crespo-Blanc, A., Jolivet, L. and Rossetti, F.: Lateral slab deformation and the origin of the western Mediterranean arcs. Tectonics, 23, TC1012, doi:10.1029/2002TC001488, 2004.

Faccenna, C., Speranza, F., Caracciolo, F.D., Mattei, M. and Oggiano, G. Extensional tectonics on Sardinia (Italy): insights into the arc–back-arc transitional regime. Tectonophysics 356, 213 – 232. 2002

Fernández-Viejo, G., Álvarez Pulgar, J., Gallastegui, J and Quintana, L. The fossil accretionary wedge of the Bay of Biscay:

1795   Critical wedge analysis on depth-migrated seismic sections and geodynamical implications. Journal of Geology, vol. 120, n.º 3, pp. 315-31, https://doi.org/10.1086/664789., 2012

Ferranti, L., Passaro, S. and de Alteriis, G.: Morphotectonics of the Gorringe Bank summit, eastern Atlantic Ocean, based on high-resolution multibeam bathymetry. Quat. Int., 9-114. https://doi.org/10.1016/j.quaint.2013.11.011, 2014.

Flinn, D.: On tests of significance of preferred orientation in three-dimensional fabric diagrams. The Journal of Geology, 66(5):

1800   526-539. https://doi.org/10.1086/626533, 1958.

Fonseca, J.F.B.D. and Vilanova, S.P.: The 23 April 23 1909 Benavente (Portugal) M 6.3 Earthquake. Seismol. Res. Lett., 81, 3. doi: 10.1785/gssrl.81.3.534, 2010.

Frohlich, C. and Apperson, K.D.: Earthquake focal mechanisms, moment tensors, and the consistency of seismic activity near plate boundaries, Tectonics, 11, 279–296, https://doi.org/10.1029/91TC02888, 1992.

1805   Galindo-Zaldivar, J., Jabaloy, J., Serrano, I., Morales, J., González-Lodeiro, F. and Torcal, F.: Recent and present-day stresses in the Granada Basin (Betic Cordilleras): Example of a late Miocene-present-day extensional basin in a convergent plateboundary.Tectonics,18,(4),686-702, doi: 10.1029/1999tc900016, 1999.

Galindo-Zaldivar, J., Gil, A.J., Tendero-Salmerón, V., Borque, M.J., Ercilla, G., González-Castillo, L., Sánchez-Alzola, A., Lacy, M.C., Estrada, F., Avilés, M., Alfaro, P., Madarieta-Txurruka, A. and Chacón, F.: The Campo de Dalias GNSS Network

1810   Unveils the Interaction between Roll-Back and Indentation Tectonics in the Gibraltar Arc. Sensors, 22, 2128. https://doi.org/10.3390/s22062128, 2022.

Gallastegui, J. and Pulgar, J.A.: Initiation of an active margin at the North Iberian continent-ocean transition. Tectonics 21 (4). https://doi.org/10.1029/ 2001TC901046, 2002.

Gamboa, D., Omira, R., Piedade, A., Terrinha, P., Roque, C. and Zitellini, N.: Destructive episodes and morphological

1815   rejuvenation during the lifecycles of tectonically active seamounts: Insights from the Gorringe Bank in the NE Atlantic. Earth Planet Sci Lett, 116772. https://doi.org/10.1016/j.epsl.2021.116772. 2021.

García-Navarro, E., Fernández, C. and Camacho, M.A.: Mesozoic tectonic evolution of the southwest continental Iberian Margin. Geodinamica Acta 18/2, 131–144, 2005.

Gea P.J., Negredo, A.M. and Mancilla, F. dL.: The Gibraltar slab dynamics and its influence on past and present-day Alboran domain deformation: Insights from thermo-mechanical numerical modelling. Front. Earth Sci. 11:995041. doi: 10.3389/feart.2023.995041, 2023.

Gephart, J.W. and Forsyth, D.W.: An improved method for determining the regional stress tensor using earthqueakes focal mechanism data: application to the San Fernando earthquake sequence. J. Geophys. Res., vol. 89, no B11, pages 9305-9320. https://doi.org/10.1029/JB089iB11p09305, 1984.

GFZ-Postdam [Dataset] https://geofon.gfz-potsdam.de/old/eqinfo/list.php?mode=mt

Giner-Robles, J. L., Gumiel, P., Pérez-López, R., Rodríguez-Pascua, M. A. García-Mayordomo, J., Paredes, C. and González-Casado, J. M.: Importancia en la elección de la orientación del plano de falla en el análisis de mecanismos focales de terremotos. 5th Asamblea Hispano Portuguesa de Geodesia y Geofísica, Com. Española de Geod. Y Geofís., Sevilla, Spain. 2006.

Global Centroid Moment Tensor (former Harvard Centroid Moment Tensor) [Dataset] https://www.globalcmt.org/

Gómez de la Peña, L.: The origin and tectono-sidimentary structure of the Alboran Basin. PhD. Thesis. Universidad de Barcelona. 319 pp, 2017.

Gómez-Novell, O., Ortuño, M., García-Mayordomo, J., Insua-Arévalo, J. M., Rockwell, T. K., Baize, S., Martínez-Díaz, J.J., Pallàs, R. and Massana, E.: Improved geological slip rate estimations in the complex Alhama de Murcia Fault zone (SE Iberia) and its implications for fault behaviour. Tectonics, 41, e2022TC007465. https://doi.org/10.1029/2022TC007465, 2022.

Goula, X., Olivera, C., Fleta, J., Grellet, B., Lindo, R., Rivera, L., Cisternas, A. and Carbon, D.: Present and recent stress regime in the eastern part of the Pyrenees. Tectonophysics 308, 487-502. doi:10.1016/S0040-1951(99)00120-1, 1999.

Grácia, E., Pallàs, R., Soto, J.I., Comas, M., Moreno, X., Masana, E., Santanach, P., Diez, S., García, M. and Dañobeitia, J.: Active faulting offshore SE Spain (Alboran Sea): Implications for earthquake hazard assessment in the Southern Iberian Margin. Earth Planet. Sci. Lett. 241 (2006) 734–749. doi:10.1016/j.epsl.2005.11.009, 2006.

Gràcia, E., Grevemeyer, I., Bartolomé, R., Perea, H., Martínez-Loriente, S., Gómez de la Peña, L., Villaseñor, A., Klinger, Y., Lo Iacono, C., Diez, S., Calahorrano, A., Camafort, M., Costa, S., d'Acremont, E., Rabaute, A. and Ranero, C.R.: Earthquake crisis unveils the growth of an incipient continental fault system. Nature Communications, 10:3482. https://doi.org/10.1038/s41467-019-11064-5, 2019.

Granja Bruña, J.L., Vegas, R., Sentre, M.A., Muñoz-Martín, A. and Sainz-Maza, S.: Gravity modeling of the lithosphere in the Calatrava Volcanic Province (Spain): geodynamic implications. J. Iber. Geol. 41 (2) 2015: 233-252 http://dx.doi.org/10.5209/rev_JIGE.2015.v41.n2.47617, 2015.

Grevemeyer, I., Lange, D., Villinger, H., Custódio, S. and Matias, L.: Seismotectonics of the HorseshoeAbyssal Plain and Gorringe Bank,eastern Atlantic Ocean: Constraintsfrom ocean bottom seismometer data,J. Geophys. Res. Solid Earth,122,63–78, doi:10.1002/2016JB013586, 2017.

Gutiérrez, F., Sevil, J., Silva, P.G., Roca, E. and Escosa, F.: Geomorphic and stratigraphic evidence of Quaternary diapiric activity enhanced by fluvial incision. Navarrés salt wall and graben system, SE Spain. Geomorphology, 342, 1, 176-195. https://doi.org/10.1016/j.geomorph.2019.06.002, 2019.

Gutscher, M.A., Dominguez, S., Westbrook, G.K., Le Roy, P., Rosas, F., Duarte, J.C., Terrinha, P., Miranda, J.M., Graindorge, D., Gailler, A., Sallares, V. and Bartolome, R.: The Gibraltar subduction: A decade of new geophysical data. Tectonophysics 574-575, 72-91. http://dx.doi.org/10.1016/j.tecto.2012.08.038, 2012.

Heidbach, O., Barth, A., Müller, B., Reinecker, J., Stephansson, O., Tingay, M. and Zang, A.: WSM quality ranking scheme, database description and analysis guidelines for stress indicator. World Stress Map Technical Report 16-01, GFZ German Research Centre for Geosciences. DOI: http://doi.org/10.2312/wsm.2016.001 , 2016.

Heidbach, O., Barth, A., Connolly, P., Fuchs, F., Müller, B., Reinecker, J., Sperner, B., Tingay, M. and Wenzel, F.: Stress Maps in a Minute: The 2004 World Stress Map Release, EOS Trans., 85(49), 521-529, https://doi.org/10.1029/2004EO490001, 2004.

Heidbach, O., and Höhne, J.: CASMI - a tool for the visualization of the World Stress Map data base, Comp. & Geosciences, 34(7), 783-791, doi:10.1016/j.cageo.2007.06.004, 2008.

Heidbach, O., Rajabi, M., Cui, X., Fuchs, K., Müller, B., Reinecker, J., Reiter, K., Tingay, M., Wenzel, F.,, Xie, F., Ziegler, M.O., Zoback., M.L. and Zoback, M. .: The World Stress Map database release 2016: Crustal stress pattern across scales, Tectonophys., 744, 484-498, doi:10.1016/j.tecto.2018.07.007, 2018.

Heidbach, O., Rajabi, M., Reiter, K., Ziegler, M. O. and WSM Team: World Stress Map Database Release 2016, edited by G. D. Services, GFZ German Research Centre for Geosciences, doi:10.5880/WSM.2016.001, 2016.

Heidbach, O., Reinecker, J., Tingay, M., Müller, B., Sperner, B., Fuchs, K. and Wenzel, F.: Plate boundary forces are not enough: Second- and third-order stress patterns highlighted in the World Stress Map database, Tectonics, 26, TC6014, doi:10.1029/2007TC002133, 2007.

Heidbach, O., Tingay, M., Barth, A., Reinecker, J., Kurfeß, D. and Müller, B.: Global crustal stress pattern based on the World Stress Map database release 2008, Tectonophys., 482, 3-15, doi:10.1016/j.tecto.2009.07.023, 2010.

Instituto Andaluz de Geofísica [Dataset] https://iagpds.ugr.es/investigacion/informacion-general

Instituto Geográfico Nacional de España [Dataset]https://www.ign.es/web/ign/portal/tensor-momento-sismico/-/tensor-momento-sismico/getExplotacion

IPMA Portuguese Institute for Sea and Atmosphere [Dataset] https://www.ipma.pt/en/geofisica/tensor

Istituto Nazionale di Geofisica e Vulcanologia [Dataset] http://terremoti.ingv.it/en/tdmt

Jackson, M.P.A. and Hudec, M.R.: Salt tectonics, Principles and Practice. Part III - Salt-Tectonic Systems. Chapter 12 - Strike-Slip Salt-Tectonic Systems. Cambridge University Press. https://doi.org/10.1017/9781139003988.016, 2017.

Jost, M. L., Büßelberg, T., Jost, Ö., and Harjes, H. P.: Source parameters of injection-induced microearthquakes at 9 km depth at the KTB deep drilling site, Germany. Bull. Seismol. Soc. Am., 88(3), 815-832, 1998.

Kagan, Y.Y.: 3-D rotation of double-couple earthquake sources, Geophys. J. Int., 106, 709–716, https://doi.org/10.1111/j.1365-246X.1991.tb06343.x ,1991.

Khazaradze, G., Pena-Castellnou, S., Santamaría-Gómez, A., and Vernant, P.: 3D GPS velocity field of the Iberian Peninsula. Geophysical Research Abstracts, 21, EGU2019-9710, 2019.

Kiratzi, A. and Papazachos, C.: Active crustal deformation from the Azores triple junction to Middle East, Tectonophysics 243, 1-24, https://doi.org/10.1016/0040-1951(94)00188-F ,1995.

Lacan, P. and Ortuño, M.: Active Tectonics of the Pyrenees: A review. J. Iber. Geol. 38 (1) 2012: 9-30. http://dx.doi.org/10.5209/rev_JIGE.2012.v38.n1.39203, 2012.

Lacan, P.: Activité Sismotectonique Plio-Quaternaire del'Ouest des Pyrénées. PhD. Thesis. Université de Pau et des Pays de l'Adour: 284 pp., 2008.

Ljunggren, C., Chang, Y., Janson, T. and Christiansson, R.: An overview of rock stress measurement methods, International Journal of Rock Mechanics and Mining Sciences, 40(7-8), 975-989, doi:10.1016/j.ijrmms.2003.07.003. 2003.

López-Fernández, C., Fernández-Viejo, G., Olona, J. and Llana-Fúnez, S.: Intraplate Seismicity in Northwest Iberia along the Trace of the Ventaniella Fault: A Case for Fault Intersection at Depth. Bull. Seismol. Soc. Am., Vol. 108, No. 2, pp. 604–618, April 2018, doi: 10.1785/0120170215. 2018.

Lundstern, J-E. and Zoback, M.D.: Multiscale variations of the crustal stress field throughout North America. Nature Communications, 11:1951, https://doi.org/10.1038/s41467-020-15841-5, 2020.

Madarieta-Txurruka, A., González-Castillo, L., Peláez, J. A., Catalán, M., Henares, J., Gil, A. J., Lamas-Fernández, F. and Galindo-Zaldivar, J.: The role of faults as barriers in confined seismic sequences: 2021 seismicity in the Granada Basin (Betic Cordillera). Tectonics, 41, e2022TC007481. https://doi.org/10.1029/2022TC007481, 2022.

Maillard, A. and Mauffret, A.: Crustal structure and riftogenesis of the Valencia Trough (north-western Mediterranean Sea). Basin Research, 11, 357–379, 1999.

Maouche, S., Bouhadad, Y., Harbi, A., Rouchiche, Y., Ousadou, F. and Ayadi, A.: Active Tectonics and Seismic Hazard in the Tell Atlas (Northern Algeria): A Review. In: Bendaoud, A., Hamimi, Z., Hamoudi, M., Djemai, S., Zoheir, B. (eds) The Geology of the Arab World---An Overview. Springer Geology. Springer, Cham. https://doi.org/10.1007/978-3-319-96794-3_10, 2019.

Maouche, S., Meghraoui, M., Morhange, C., Belabbes, S., Bouhadad, Y. and Haddoum, H.: Active coastal thrusting and folding, and uplift rate of the Sahel Anticline and Zemmouri earthquake area (Tell Atlas, Algeria). Tectonophysics 509, 69–80. doi:10.1016/j.tecto.2011.06.003, 2011.

Martin-Gonzalez, F. and Heredia, N.: Geometry, structures and evolution of the western termination of the Alpine-Pyrenean Orogen reliefs (NW Iberian Peninsula). J. Iber. Geol., 37, DOI: 10.5209/rev_JIGE.2011.v37.n2.1103, 2011.

Martín, R., Stich, D., Morales, J and Mancilla F.: Moment tensor solutions for the Iberain-Maghreb region during the IberArray deployment (2009-2013). Tectonophysics, 663, 261-274, [Dataset] https://doi.org/10.1016/j.tecto.2015.08.012, 2015.

Martínez-Díaz, J. J.: Neotectonica y Tectonica Activa del Oeste de Murcia y sur de Almeria (Cordillera Betica). PhD Thesis, Universidad Complutense Madrid: 470 p, 1998.

Martínez-Díaz, J.J., Masana, E, and Ortuño, M.: Active tectonics of the Alhama de Murcia fault, Betic Cordillera, Spain. J. Iber. Geol. 38 (1), 253-270. http://dx.doi.org/10.5209/rev_JIGE.2012.v38.n1.39218, 2012.

Martínez-García, P.: Recent tectonic evolution of the Alboran Ridge and Yusuf regions. PhD. Thesis. Instituto andaluz de Ciencias de la Tierra (CSIC-UGR). 276 pp, 2012.

Martínez-Loriente, S., Gracia, E., Bartolome, R., Sallarès, V., Connors, C., Perea, H., Lo Iacono, C., Klaeschen, D., Terrinha, P., Dañobeitia, J.J. and Zitellini, N.: Active deformation in old oceanic lithosphere and significance for earthquake hazard: Seismic imaging of the Coral Patch Ridge area and neighboring abyssal plains (SW Iberian Margin). Geochem., Geophys., Geosyst., 14, 00. doi: 10.1002/ggge.20173, 2013.

Masana, E., Neotectonic features of the Catalan Coastal Ranges, Northeastern Spain. Acta Geológica Hispánica, 29, 2-4, 107-121, 1996.

Masana, E., Martínez-Díaz, J.J. Hernández-Enrile, J.L. and Santanach, P., The Alhama de Murcia fault (SE Spain), a seismogenic fault in a diffuse plate boundary: Seismotectonic implications for the Ibero-Magrebian region. J. Geophys. Res., Vol. 109, B01301, doi:10.1029/2002JB002359, 2004.

Masana, E., Moreno, X., Gràcia, E., Pallàs, R., Ortuño, M., López, R., Gómez-Novell, O., Ruano, P., Perea, H., Stepancikova, P. and Khazaradze, G.: First evidence of paleoearthquakes along the Carboneras Fault Zone (SE Iberian Peninsula): Los Trances site. Geologica Acta, 16, 4, 461-476 DOI: 10.1344/GeologicaActa2018.16.4.8, 2018.

Matias, H., Kress, P., Terrinha, P., Mohriak, W., Paulo, T., Menezes, L., Matias, L., Santos, F. and Sandnes, F.: Salt tectonics in the western Gulf of Cádiz, southwest Iberia. American Association of Petroleum Geologist Bulletin, 95(10), 1667-1698, 2011.

Matos, C., Custódio, S., Batlló, J., Zahradník, J., Arroucau, P., Silveira, G., and Heimann, S.: An active seismic zone in intraplate west Iberia inferred from high-resolution geophysical data. J. Geophy. Res: Solid Earth, 123, 2885–2907. [Dataset] https://doi.org/10.1002/2017JB015114, 2018.

McKenize, D.P.: The relation between fault plane solutions for earthquakes and the direction of the principal stresses. Bull. Seismol. Soc. Am. 59 (2): 591–601. https://doi.org/10.1785/BSSA0590020591, 1969.

Meghraoui, M., Cisternas, A. and Philip, H.: Seismotectonics of the Lower Cheliff Basin: Structural background of the El Asnam (Algeria) earthquake. Tectonics, 5, 6, 809-836, https://doi.org/10.1029/TC005i006p00809, 1986.

Meghraoui, M., and Pondrelli, S.:Active faulting and transpression tectonics along the plate boundary in North Africa, Ann. Geophys. 55, no. 5, doi: 10.4401/ag-4970, 2012.

Michael, A.: Use of Focal Mechanisms to Determine Stress: A Control Study. Journal of Geophysical Research: Solid Earth 92, no. B1: 357–68. https://doi.org/10.1029/JB092iB01p00357, 1987.

Montadert, L., B. Damotte, J. P. Fail, J. R. Delteil, and P. Valéry, Structure géologique de la plaine abyssale du Golfe de Gascogne, in Histoire Structurale du Golfe de Gascogne, edited by J. Debysier, X. Le Pichon, and M. Montadert, VI.14.1-VI.14.42, Technip, París, 1971.

Montenat, C. and d'Estevou, P. O.: The diversity of late Neogene sedimentary basins generated by wrench faulting in the Eastern Betic Cordillera, SE Spain. J. Pet. Geol., 22(1), 61-80, https://doi.org/10.1111/j.1747-5457.1999.tb00459.x, 1999.

Morales, J., Azañón, J.M., Stich, D., Roldán, F.J., Pérez-Peña, J.V., Martín, R., Cantavella, J.V., Martín, J.B., Mancilla, F. and González.Ramón, A.: The 2012-2013 earthquake swarm in the eastern Gualdalquivir Basin (South Spain): A case of heterogenous faulting due to oroclinal bending. Gondwana Research, Volume 28, Issue 4, Pages 1566-1578, https://doi.org/10.1016/j.gr.2014.10.017, 2015.

Morawietz, S., Heidbach, O., Reiter, K., Ziegler, M. O., Rajabi, M., Zimmerman, G., Müller, B. and Tingay, M.: An open access stress magnitude database for Germany and adjacent regions, Geothermal Energy, doi:10.1186/s40517 020 00178-5, 2020.

Neres, M., Carafa, M. M. C., Fernandes, R.M.S., Matias. L., Duarte, J.C., Barba, S. and Terrinha, P. Lithospheric deformation in the Africa-Iberia plate boundary: Improved neotectonic modeling testing a basal-driven Alboran plate. JGR Solid Earth, https://doi.org/10.1002/2016JB013012, 2019.

Neres, M., Neves, M. C., Custódio, S., Palano, M., Fernandes, R. and Matias, L.: Gravitational potential energy in Iberia: A driver of active deformation in high-topography regions. J. Geophys. Res.: Solid Earth, 123. https://doi.org/10.1029/2017JB015002, 2018a.

Neres, M., Terrinha, P., Custodio, S.M., Silva, J., and Miranda, J.M. Geophysical evidence for a magmatic intrusion in the ocean-continent transition of the SW Iberia margin. Tectonophysics, 744:118–133, Oct 2018, https://doi.org/10.1016/j.tecto.2018.06.014. 2018b

Neves, M.C., Terrinha, P., Afilhado, A., Moulin, M., Matias, L. and Rosas, F.: Response of a multi-domain continental margin to compression: Study from seismic reflection–refraction and numerical modelling in the Tagus Abyssal Plain. Tectonophysics 468, 113–130. http://dx.doi.org/10.1016/j.tecto.2008.05.008. 2009.

Nirrengarten, M., Manatschal, G., Tugend, J., Kusznir, N. and Sauter, D. Kinematic Evolution of the Southern North Atlantic: Implications for the Formation of Hyperextended Rift Systems. Tectonics, https://doi.org/10.1002/2017TC004495., 2018

Olaiz, A.J., Álvarez Gómez, J., A, de Vicente, G., Muñoz-Martín, A., Cantavella, J.V., Custódio, S., Vales, D. and Heidbach, O.: Seismo-tectonics of Greater Iberia: An updated review, Zenodo repository, doi:10.5281/zenodo.14326528

Olaiz, A.J., Muñoz-Martín, A., de Vicente, G., Vegas, R. and Cloetingh, S.: European continuous active tectonic strain–stress map. Tectonophysics, 474, 33–40, https://doi.org/10.1016/j.tecto.2008.06.023, 2009.

Olivera, C., Redondo, E., Lambert, J., Riera Melis, A. and Roca, A.: Els terratrèmols dels segles XIV i XV a Catalunya. Institut Cartogràfic de Catalunya, Monografies 30, 407pp, ISBN: 84-393-6961-1, 2006.

Pedrera, A., Ruiz-Constán, A., Marín-Lechado, C., Galindo-Zaldivar, J., González, A. and Peláez, J. A.: Seismic transpressive basement faults and monocline development in a foreland basin (eastern Guadalquivir, SE Spain). Tectonics, 32, 1571–1586. https://doi.org/ 10.1002/2013TC003397, 2013.

Perea, H., Masana, E. and Santanach, P.: An active zone characterized by slow normal faults, the northwestern margin of the València trough (NE Iberia): a review. J. Iber. Geol. 38(1):31–52, https://doi.org/10.5209/rev_jige.2012.v38.n1.39204, 2012.

Perea, H., Masana, E. and Simón, J.L.: Slow active faults along the extensional northeastern margin of the Iberian Peninsula. In The Geology of Iberia: A Geodynamic Approach Volume 5: Active Processes: Seismicity, Active Faulting and Relief, 10.1007/978-3-030-10931-8_4, 2020.

Pereira, R., Rosas, F., Mata, J., Represas, P., Escada, C. and Silva, B.: Interplay of tectonics and magmatism during post-rift inversion on the central West Iberian Margin (Estremadura Spur). Basin Research, 33:1497–1519. DOI: 10.1111/bre.12524, 2021.

Pierdominici, S., and Heidbach, O.: Stress field of Italy – Mean stress orientation at different depths and wave-length of the stress pattern, Tectonophys., 532-535, 301-311, doi:10.1016/j.tecto.2012.02.018, 2012.

Pla-Pueyo, S., Gierlowski-Kordesch, E.H., Viseras, C. and Soria, J.M.: Major controls on sedimentation during the evolution of a continental basin: Pliocene–Pleistocene of the Guadix Basin (Betic Cordillera, southern Spain). Sediment. Geol. 219 97–114. http://dx.doi.org/10.1016/j.sedgeo.2009.05.001, 2009.

Pondrelli S., Morelli, A. and Ekström, G.: European-Mediterranean Regional Centroid MomentTensor catalog: solutions for years 2001 and 2002, Phys. Earth Planet. Int., 145, 127-147. [Dataset] https://doi.org/10.1016/j.pepi.2004.03.008, 2004.

Pondrelli, S., Morelli, A., Ekström, G. Mazza, S., Boschi, E. and Dziewonski, M.: European- Mediterranean regional centroid-moment tensors: 1997-2000, Phys. Earth Planet. Int., 130, 71-101. [Dataset] https://doi.org/10.1016/S0031-9201(01)00312-0, 2002.

Posadas, A.M., Vidal, F., De Miguel, F., Alguacil, G., Peña, J., Ibañez, J.M. and Morales, J.: Spatial-Temporal Analysis of a Seismic Series Using the Principal Components Method: The Antequera Series, Spain, 1989. J. Geophys. Res., 98, B2, 1923-1932., 1993.

Rajabi, M., Tingay, M., Heidbach, O., Hillis, R. and Reynolds, S.: The present-day stress field of Australia, Earth Sci. Rev., 168, 165-189, doi:10.1016/j.earscirev.2017.04.003. 2017a

Rajabi, M., Tingay, M., King, R. and Heidbach, O.: Present-day stress orientation in the Clarence-Moreton Basin of New South Wales, Australia: A new high density dataset reveals local stress rotations, Basin Res., 29(S1), 622-640, doi:10.1111/bre.12175, 2017b.

Rajabi, M., Ziegler, M. O., Heidbach, O., Mukherjee, S. and Esterle, J.: Contribution of mine borehole data toward high-resolution stress mapping: An example from northern Bowen Basin, Australia, Int. J. Rock Mech. Min. Sci., 173, doi:10.1016/j.ijrmms.2023.105630, 2024.

Ramos, A., Fernández, O., Terrinha, P. and Muñoz, J.A.: Extension and inversion structures in the Tethys?Atlantic linkage zone, Algarve Basin, Portugal. Int. J. Earth Sci. (Geol Rundsch) 1–17. http://dx.doi.org/10.1007/s00531-015-1280-1., 2015.

2015   Ramsay, J.G.: Folding and fracturing rocks. McGraw-Hill, New York, N.Y. 560 pp., ISBN 978-0070511705, 1967.

Reches, Z.: Faulting of rocks in three-dimensional strain fields. II. Theoretical analysis, Tectonophysics, 47, 109 – 129. https://doi.org/10.1016/0040-1951(83)90264-0, 1983.

Reches, Z.: Determination of the tectonic stress tensor from slip along faults that obey the Coulomb yield condition. Tectonics, vol. 6, no. 6, 849-861 https://doi.org/10.1029/TC006i006p00849, 1987.

2020   Reches, Z., Baer, G. and Hatzor, Y.: Constraints on the strength of the Upper Crust from stress inversion of fault slip data, J. Geophys, Res, 97, 12,481 – 12,493. https://doi.org/10.1029/90JB02258, 1992.

Reicherter, K.R. and Peters, G. Neotectonic evolution of the Central Betic Cordilleras (Southern Spain). Tectonophysics 405,191-212. https://doi.org/10.1016/j.tecto.2005.05.022, 2005.

Reicherter, K.R. and Pletsch, T.K. Evidence for a synchronous Circum-Iberian subsidence event and its relation to the African-

2025   Iberian plate convergence in the Late Cretaceous. Terra Nova 12, 141-147, https://doi.org/10.1046/j.1365-3121.2000.123276.x 2002.

Reinecker, J., Tingay, M., Muller, B. and Heidbach, O.: Present-day stress orientation in the Molasse Basin, Tectonophysics, 482(1-4), 129-138, doi:10.1016/j.tecto.2009.07.021, 2010.

Reiter, K., Heidbach, O., Schmitt, D. R., Moeck, I., Ziegler, M. O. and Hauck, C.: Crustal stress field pattern of Canada,

2030   Tectonophys., 636, 111-124, doi:10.1016/j.tecto.2014.08.006, 2014.

Roca, E. and Guimerà, J.: The Neogene structure of the eastern Iberian margin: Structural constraints on the crustal evolution of the Valencia trough (western Mediterranean). Tectonophysics 203(1–4):203–218. https://doi.org/10.1016/0040-1951(92)90224-t, 1992.

Roca, E., and Muñoz, J. A. The Pyrenean orogen: pre-, syn- and post-collisional evolution. En: Ziegler, P.A., Horvath, F. (eds)

2035   Peri-Tethys Memoir 2: Structure and Prospects of Alpine Basins and Forelands. Mémoires du Muséum national d'Histoire naturelle, 170, 203–219. 1996.

Rueda, J. and Mezcua, J.: Near-real-time seismic moment-tensor determination in Spain. Seismol. Res. Lett. 76, 455-465. [Dataset] https://doi.org/10.1785/gssrl.76.4.455, 2005.

Ruiz, M., Diaz, J., Canari, A., Ortuño, M. and Vergés, J.: Seismic Activity at the Eastern Pyrenean Termination. Available at

2040   SSRN: https://ssrn.com/abstract=4341777 or http://dx.doi.org/10.2139/ssrn.4341777, 2023.

Ruiz, M., Gallart, J., Díaz, J., Olivera, C., Pedreira, D., López, C., González-Cortina, J.M. and Pulgar, J.A.: Seismic activity at the western Pyrenean Edge. Tectonophysics 412, 217–235, https://doi.org/10.1016/j.tecto.2005.10.034, 2006.

Ruiz Constán, A.: Lithospheric structure of the western Betic Cordillera and its foreland implications in the recent tectonic evolution. PhD Thesis. Universidad de Granada, 162 pp., 2009.

2045   Ruiz-Constán, A., Galindo-Zaldívar, J., Pedrera, A., Célérier, B. and Marín-Lechado, C.: Stress distribution at the transition from subduction to continental collision (northwestern and central Betic Cordillera), Geochem. Geophys. Geosyst., 12, Q12002, doi:10.1029/2011GC003824, 2011.

Rutter, E.H., Faulkner, D.R. and Burgess, R.: Structure and geological history of the Carboneras Fault Zone, SE Spain: Part of a stretching transform fault system. Journal of Structural Geology, 45, 68-86. http://dx.doi.org/10.1016/j.jsg.2012.08.009, 2012.

Sanz de Galdeano, C.: Geologic evolution of the Betic Cordilleras in the Western Mediterranean, Miocene to the present. Tectonophysics, 172 (1-2), 107-119, https://doi.org/10.1016/0040-1951(90)90062-D, 1990.

Sanz de Galdeano, C., García-Tortosa, F.J., Peláez, J.A., Alfaro, P., Azañón, J.M., Galindo- Zaldívar, J., López Casado, C., López Garrido, A.C., Rodríguez-Fernández, J. and Ruano, P.: Main active faults in the Granada and Guadix-Baza Basins (Betic Cordillera). J. Iber. Geol. 38 (1) 2012: 209-223. http://dx.doi.org/10.5209/rev_JIGE.2012.v38.n1.39215 , 2012.

Scognamiglio, L., Tinti, E. and Quintiliani, M.: Time Domain Moment Tensor (TDMT) (Data set). Istituto Nazionale di Geofisica e Vulcanologia (INGV). [Dataset] https://doi.org/10.13127/TDMT, 2006.

SGC, 1985–1997. Butlletí Sismològic. Generalitat de Catalunya. Servei Geològic de Catalunya.

Sibuet, J. C., Srivastava, S. P. and Spakman, W. Pyrenean orogeny and plate kinematics. J. Geophys. Res. 109:B08104, doi:10.1029/2003JV002514., 2004

Simón J.L.: Late Cenozoic stress field and fracturing in the Iberian Chain and Ebro Basin (Spain). J. Struct. Geol. 11:285–294, https://doi.org/10.1016/0191-8141(89)90068-0, 1989.

Simón, J.L.: Active faults in the Iberian Chain. In The Geology of Iberia: A Geodynamic Approach Volume 5: Active Processes: Seismicity, Active Faulting and Relief,   10.1007/978-3-030-10931-8_4, 2020.

Soumaya, A., Ben Ayed, N., Rajabi, M., Meghraoui, M., Delvaux, D., Kadri, A., et al.: Active faulting geometry and stress pattern near complex strike-slip systems along the Maghreb region: Constraints on active convergence in the western Mediterranean. Tectonics, 37, 3148–3173. https://doi.org/10.1029/ 2018TC004983, 2018.

Souriau, A. and Pauchet, H.: A new synthesis of Pyrenean seismicity and its tectonic implications. Tectonophysics 290, 221-244. doi: 10.1016/S0040-1951(98)00017-1, 1998.

Sperner, B., Müller, B., Heidbach, O., Delvaux, D., Reinecker, J. and Fuchs, K.: Tectonic stress in the Earth's crust: advances in the World Stress Map project, in New insights in structural interpretation and modelling, edited by D. A. Nieuwland, pp. 101-116, Geological Society, London, doi:10.1144/gsl.sp.2003.212.01.07, 2003.

Srivastava, S. P., Roest, W. R., Kovacs, L. C., Oakey, G., Levesque, S., Verhoef, J. and Macnab, R. Motion of Iberia since the Late Jurassic: Results from detailed aeromagnetic measurements in the Newfoundland Basin, Tectonophysics, 184, 229 – 260, https://doi.org/10.1016/0040-1951(90)90442-B 1990

Stich, D., Serpelloni, E., Mancilla, F.L. and Morales, J.: Kinematics of the Iberia– Maghreb plate contact from seismic moment tensors and GPS observations, Tectonophysics, 426, 3-4, 295-317 [Dataset] doi:10.1016/j.tecto.2006.08.004, 2006.

Stich, D., Martín, R., and Morales, J.: Moment tensor inversion for Iberia-Maghreb earthquakes 2005-2008. Tecthonophysics, 483, 390-398. [Dataset] https://doi.org/10.1016/j.tecto.2009.11.006, 2010.

Stich, D., Ammon, C.J. and Morales, J.: Moment tensor solutions for small and moderate earthquakes in the Ibero-Maghreb region, J. Geophys. Res. 108, 02JB002057. [Dataset] https://doi.org/10.1029/2002JB002057, 2003.

Stich, D., Batlló, J., Maciá, R., Teves-Costa, P and Morales, J.: Moment tensor inversion with single-component historical seimograms: The 1909 Benavente (Portugal) and Lambesc (France) earthquakes. Geophys. J. Int. 162, 850–858, [Dataset]doi: 10.1111/j.1365-246X.2005.02680.x, 2005.

2085 Stich, D., Martín, R., Morales, J., López-Comino, J.A. and Mancilla, FdL.: Slip partitioning in the 2016 Alboran Sea Earthquake Sequence (Western Mediterranean). Front, Earth Sci. 8:587356. [Dataset]. https://doi.org/10.3389/feart.2020.587356, 2020.

Tendero-Salmerón, V.: Recent and active deformation structures in the centra-eastern sector of the Betic Cordillera and the Alboran Sea: indentation processes and roll-back. Ph.D. Thesis. Universidad de Granada, 238 pp, 2022.

2090 Tendero-Salmerón, V., Galindo-Zaldivar, J., Peláez, J. A.,Martínez-Martos, M., Henares, J. and Marín-Lechado, C.: Seismicity in strike-slip foreland faults (central Betic cordillera front): Evidence of indentation tectonics. Tectonics, 39, e2020TC006143. https:// doi.org/10.1029/2020TC006143, 2020.

Tendero-Salmerón V, Lafosse M, d'Acremont E, Rabaute A, Azzouz O, Ercilla G, Makkaoui M and Galindo-Zaldivar J.: Application of Automated Throw Backstripping Method to Characterize Recent Faulting Activity Migration in the Al Hoceima
2095 Bay (Northeast Morocco): Geodynamic Implications. Front. Earth Sci. 9:645942. doi: 10.3389/feart.2021.645942, 2021.

Tendero-Salmerón, V., Galindo-Zaldivar, J., d'Acremont, E., Catalán, M., Martos, Y.M., Ammar, A. and Ercilla, G.: New insights on the Alboran Sea basin extension and continental collision from magnetic anomalies related to magmatism (western Mediterranean). Marine Geology, 443, 106696. https://doi.org/10.1016/j.margeo.2021.106696, 2022.

Terrinha, P.: Structural Geology and Tectonic Evolution of the Algarve Basin, South Portugal. PhD Thesis. Imperial College,
2100 London, pp. 430, 1998.

Terrinha, P., Matias, L., Vicente, J., Duarte, J., Pinheiro, J.L., Lourenço, N., Diez, S., Rosas, F., Magalhães, V., Valadares, V., Zitellini, N., Roque, C., Mendes Víctor, L. and MATESPRO Team: Morphotectonics and strain partitioning at the Iberia–Africa plate boundary from multibeam and seismic reflection data. Marine Geology, 267, 156–174. http://dx.doi.org/10.1016/j.margeo.2009.09.012, 2009.

2105 Tingay, M., Müller, B., Reinecker, J. and Heidbach, O.: State and Origin of the Present-day Stress Field in Sedimentary Basins: New Results from the World Stress Map Project, paper presented at 41st U.S. Symposium on Rock Mechanics (USRMS): 50 years of Rock Mechanics - Landmarks and Future Challenges, Golden, Colorado, June, 17-21, 2006.

Tingay, M., Müller, B., Reinecker, J., Heidbach, O., Wenzel, F. and Fleckenstein, P.: Understanding tectonic stress in the oil patch: The World Stress Map Project, The Leading Edge, 24, 1276-1282, doi:10.1190/1.2149653, 2005.

2110 Tozer, B., Sandwell, D. T., Smith, W. H. F., Olson, C., Beale, J. R. and Wessel, P.: Global Bathymetry and Topography at 15 Arc Sec: SRTM15+, Earth and Space Science, 6(10), 1847-1864, doi:10.1029/2019ea000658, 2019.

Vadillo Muñoz, O.: Análisis de la serie sísmica de Palenciana (Córdoba), Junio de 1989 y sus implicaciones sismotectónicas. PhD Thesis. Universidad Complutense de Madrid. 364 pp, 1999.

Van der Woerd, J., Dorbath, C., Ousadou, F., Dorbath, L., Delouis, B., Jacques, E., Tapponnier, P., Hahou, Y., Menzhi, M., Frogneux, M. and Haessler, H.: The Al Hoceima Mw 6.4 earthquake of 24 February 2004 and its aftershocks sequence. J. Geodyn., 77, 89–109. http://dx.doi.org/10.1016/j.jog.2013.12.004, 2014.

Van Hinsbergen, D., Vissers, J.J., Reinoud, L.M. and Spakman, W.: Origin and consequences of western Mediterranean subduction, rollback, and slab segmentation. Tectonics 33 (4), 393-419, https://doi.org/10.1002/2013TC003349, 2014.

Vázquez, J.T., Alonso, B., Fernández-Puga, M.C., Gómez-Ballesteros, M., Iglesias, J., Palomino, D., Roque, C., Ercilla, G. and Díaz-del-Río, V.: Seamounts along the Iberian Continental Margins. Boletín Geológico y Minero, 126 (2-3): 483-514 ISSN: 0366-0176, 2015.

Vegas, R., and Rincón-Calero, P.J. Campos de esfuerzos, deformación alpina y volcanismo Neógeno-cuaternario asociado en el antepaís bético de la provincia de Ciudad Real (España Central). Geogaceta 19, 31–34. 1996.

Vergés, J.: Evolución de los sistemas de rampas oblicuas de los Pirineos meridionales: fallas del Segre y Pamplona. Boletín Geológico y Minero, 114 (1): 87-101 ISSN: 0366-0176, 2003.

Villamor, M. P.: Cinemática terciaria y cuaternaria de la falla de Alentejo-Plasencia y su influencia en la peligrosidad sísmica del interior de la península ibérica. PhD Thesis. Universidad Complutense de Madrid, 343 pp.. 2002.

Villaseñor, A., Herrmann, R.B., Gaite, B. and Ugalde, A.: Fault reactivation by gas injection at an undergroung gas storage off the east coast of Spain. Solid Earth, 11, 63-74. [Dataset].https://doi.org/10.5194/se-11-63-2020, 2020.

Wessel, P. and Smith, W. H. F.: New version of the Generic Mapping Tools released. Eos, Transactions American Geophysical Union, 76(33), 329. https://doi.org/10.1029/95EO00198, 1995.

Wessel, P., Smith, W.H.F., Scharroo, R., Luis, J. and Wobbe, F.: Generic Mapping Tools: Improved Version Released. Eos, 94, 45, 5. 409–420, 2013.

Wetzler, N., Sagy, A., Marco, S. and Reches, Z. Asymmetry of faults and stress patterns within the Dead Sea basin as displayed by seismological analysis. Tectonophysics 819, 229069, https://doi.org/10.1016/j.tecto.2021.229069, 2021.

Ziegler, M. O. and Heidbach O.: Manual of the Matlab script Stress2Grid v1.1Rep., 33 pp, GFZ German Research Centre for Geosciences, Potsdam, 2019, https://doi.org/10.5880/wsm.2019.002

Zitellini, N., Gràcia, E., Matias, L., Terrinha, P., Abreu, M.A., DeAlteriis, G., Henriet, J.P. Dañobeitia, J.J., Masson, D.G. Mulder, T., Ramella, R., Somoza, L. and Diez, S.: The quest for the Africa–Eurasia plate boundary west of the Strait of Gibraltar. Earth and Planetary Science Letters 280, 13–50 https://doi.org/10.1016/j.epsl.2008.12.005, 2009.

Zoback, M.-L.: First- and Second- Order Patterns of Stress in the Lithosphere: The World Stress Map Project, J. Geophys. Res., 97., https://doi.org/10.1029/92JB00132, 1992.